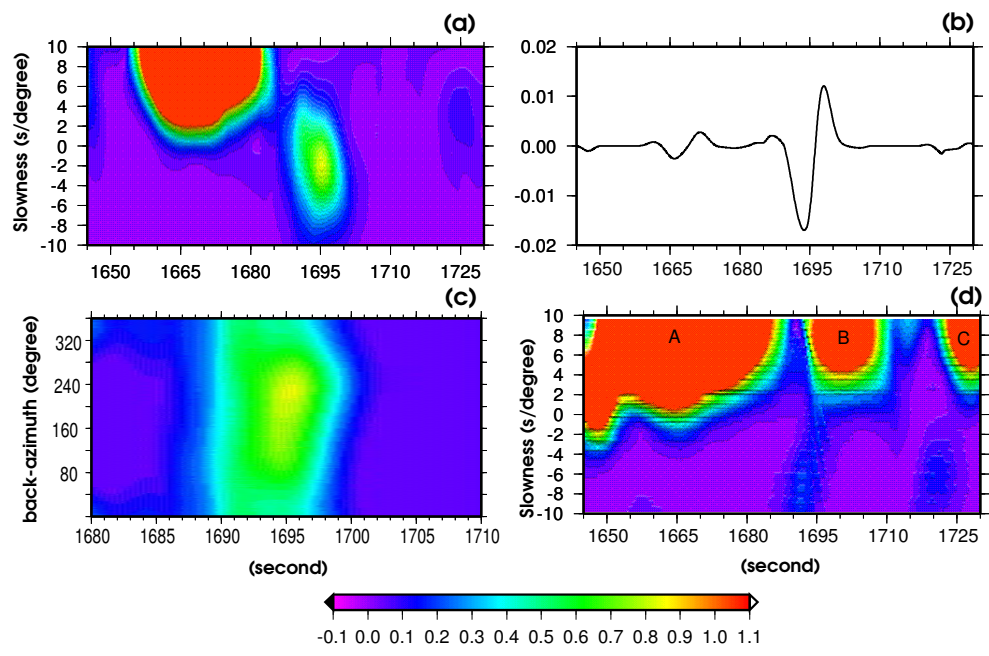


Chapter 13

Research Studies



1. Nonvolcanic Tremors on the Central San Andreas Fault

Robert M. Nadeau, David Dolenc and Aurelie Guilhem

1.1 Introduction

Nonvolcanic tremor activity (i.e., long-duration seismic signals with no clear P or S waves (Figure 13.1) may provide important clues to the rheology and processes responsible for the nucleation and seismic cycles of large earthquakes. Prior to our research, nonvolcanic tremors had only been observed in subduction zones (i.e., thrust fault plate boundaries) (e.g., *Obara, 2002; Rogers and Dragert, 2003*), where fluids from subduction processes were believed to play an important role in generating these tremors.

In Cascadia, a significant correlation between subduction zone tremor activity and subseismogenic zone (i.e. beneath the upper ~ 15 km of Earth's crust where earthquakes occur) slow slip events (referred to as episodic tremor and slip (ETS, *Rogers and Dragert, 2003*)) has also been observed, suggesting that stress changes from ETS events increase stress and possibly trigger earthquakes in the shallower seismogenic fault zone.

1.2 SAF Tremors

Because subduction has not occurred along the central SAF for several million years, fluids from active subduction are not present, and nonvolcanic tremor activity was not expected along the the central SAF zone.

Recently, however, our detailed inspection of triggered event data from Berkeley's borehole High Resolution Seismic Network (HRSN) at Parkfield, California revealed tremor-like signals originating in the vicinity of Cholame (Figure 13.1) (*Nadeau and Dolenc, 2005*).

Following the methods of *Obara (2002)*, seismic data recorded continuously with 20 Hz sampling frequency by two stations of the Southern California Seismic Network (SCSN) (Figure 13.1) and with 250 Hz sampling by the HRSN were then used to analyze these events.

Within an ~ 15 km search radius centered ~ 5 km southeast of Cholame (Figure 13.1) and during a 3-year period from 23 December 2000 to 22 December 2003 (i.e., when the M6.5 San Simeon earthquake occurred), 110 tremor events lasting between 4 to 20 minutes were identified. Locations of the tremors indicate that within the search radius, the tremors were confined to an ~ 25 km segment of the SAF and occur at depths of between 20 to 40 km.

The depths, frequency content (generally 1 to 10 Hz), S-wave propagation velocity, and waveform character of the SAF tremors were similar to those of the subduction zone tremors; however, the SAF tremors are less frequent (fewer than 5 events in any 24 hour period), have shorter

duration (less than 20 minutes), have smaller peak amplitudes (comparable to M0.5 earthquakes), and release less energy (energy equivalents $< M1.5$).

Our discovery of these nonvolcanic tremors is important for three principal reasons: 1) they occur along a transform plate boundary (i.e., the SAF) in contrast to previous nonvolcanic tremors that occur only in subduction zones, 2) no obvious source for fluid re-charge exists in the area to aid in the genesis of the tremors and 3) the highest level of tremor activity in the region occurs beneath the inferred epicentral region (1) of the moment magnitude (M) ~ 7.8 1857 Fort Tejon earthquake whose rupture zone is currently locked.

This segment of the SAF has an estimated earthquake recurrence time of 140 years (+93, -69) (*WGCEP, 1995*), and it is now over 140 years since the Fort Tejon event. Because stress changes from ETS events may trigger large earthquakes (4), future increases in SAF tremor activity may signal periods of increased probability for the next large earthquake on the segment.

An apparent correlation between tremor and local micro-earthquake rates at Cholame (*Nadeau and Dolenc, 2005*) also suggests that deep deformation associated with the Cholame tremors (i.e., ETS) may also be stressing the shallower seismogenic zone in this area.

Further evidence for stress-coupling between tremor related deep deformation and shallower SAF earthquake activity is also seen in the correlation between stress release from the nearby 28 September 2004, M6 Parkfield earthquake and the evolution of tremor activity rates in the area (Figure 13.2)

1.3 Acknowledgements

Supported by U.S. Geological Survey award no. 04HQGR0085 and U.S. Department of Energy Office of Basic Energy Sciences contract no. DE-AC03-765F00098.

1.4 References

- Nadeau, R.M. and D. Dolenc, Nonvolcanic Tremors Deep Beneath the San Andreas Fault, *Science*, 307, 389, 2005.
- Obara, K., Nonvolcanic Deep Tremor Associated with Subduction in Southwest Japan, *Science*, 296, 1679-1681, 2002.
- Rogers, G. and H. Dragert, Episodic Tremor and Slip on the Cascadia Subduction Zone: The Chatter of Silent Slip, *Science*, 300, 1942-1943, 2003.

Location

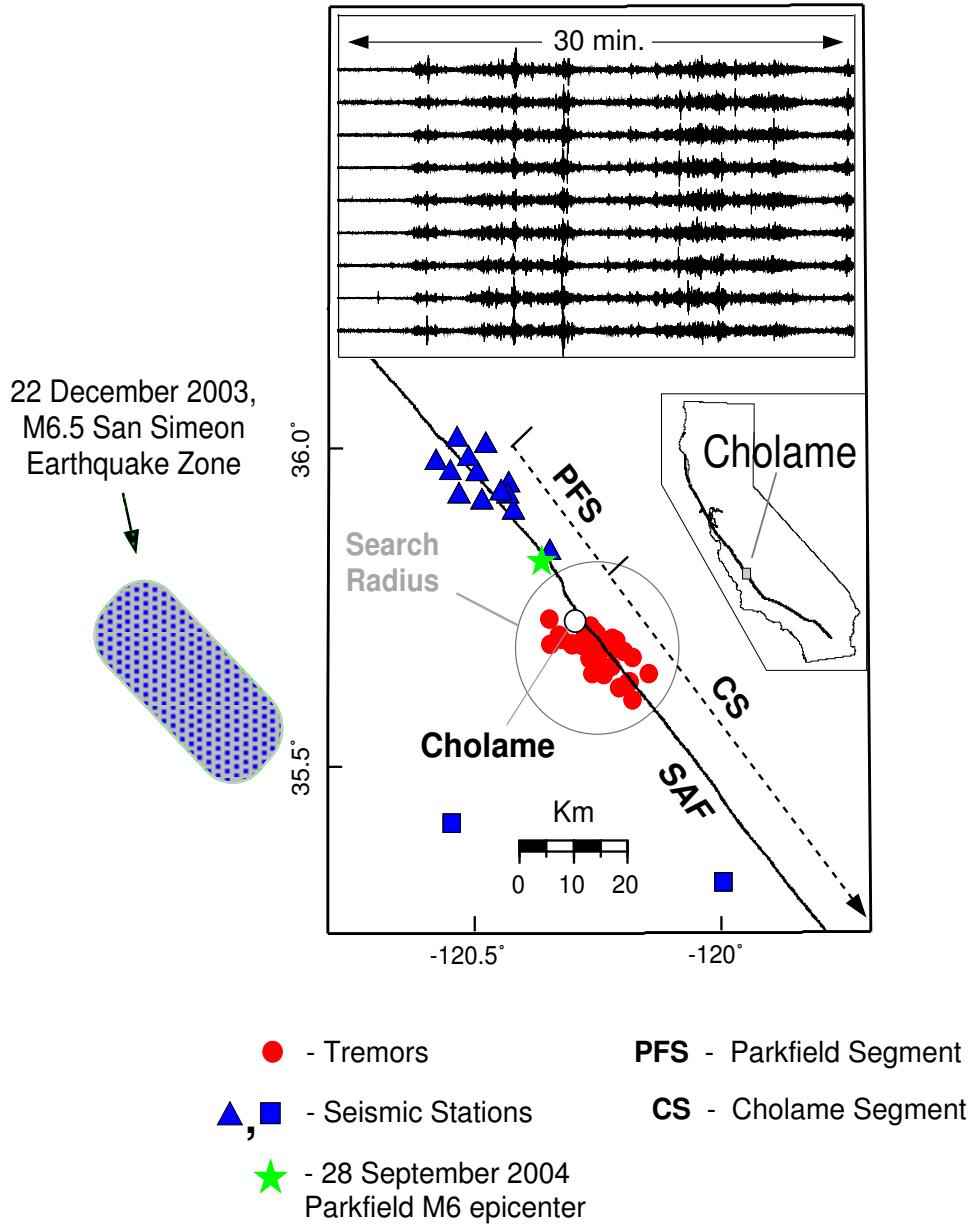


Figure 13.1: Thirty-four well-located tremors (small circles) along the northern Cholame Segment (CS) of the SAF. Triangles and squares are seismic stations of the HRSN and SCSN, respectively. Large circle is ~ 15-km-radius search zone. Star is the epicenter of the 28 September 2004, M6 Parkfield earthquake. (Inset, top) Horizontal component seismograms (3 to 8 Hz band-pass filtered) of two tremor events (ev1 and ev2) recorded by the stations with gray symbols. (Left) Approximate rupture zone of the 22 December 2003, M6.5 San Simeon Earthquake that occurred ~ 50 km to the west of the tremor zone. (Bottom inset) The location of Cholame, California.

Tremor Rate History

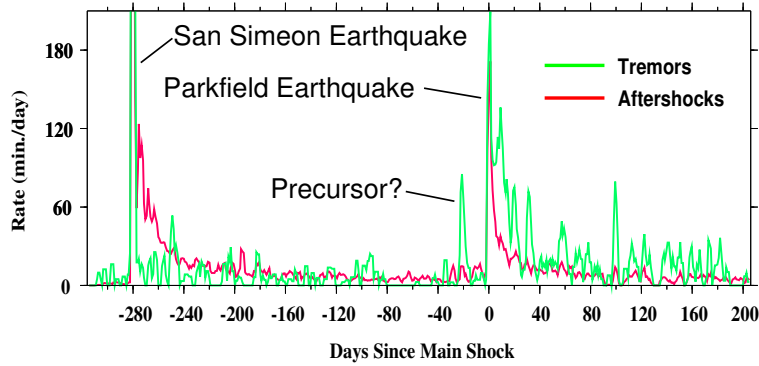


Figure 13.2: Activity rate history of nonvolcanic tremors (green) and microearthquakes (red) detected by the borehole High Resolution Seismic Network (HRSN) at Parkfield, CA. History spans 40 days prior to the San Simeon Earthquake through 200 days after the Parkfield mainshock. Tremor activity rates were not strongly influenced by the San Simeon event that occurred some 50 km to the west. However, the Parkfield earthquake whose epicenter occurred within about 10 km of the tremor zone had a strong impact. Parkfield aftershocks decayed much more rapidly than the tremor rate activity, suggesting some lag time between stress induced activity in the much deeper tremor zone relative to that in the seismogenic zone above. A precursory burst of tremor activity was also observed some 20 days prior to the Parkfield event. This is consistent with the observations of *Nadeau and Dolenc (2005)* which suggest a reciprocal stressing relationship in which stress changes associated with the tremor zone induce shallower earthquake activity with a lag time of a few weeks.

Working Group on California Earthquake Probabilities (WGCEP), Seismic hazards in southern California: probable earthquakes, 1994 to 2024, *Bull. Seism. Soc. Am.*, 85, 379-439, 1995.

2. Kinematic Modeling of the 2004 Parkfield Earthquake

Douglas Dreger, Mark Murray, Robert Nadeau, Peggy Hellweg, and Ahyi Kim

2.1 Introduction

The long-awaited Parkfield, California, earthquake occurred on September 28, 2004. This Mw 6.0 event was the latest in a series of moderate quakes (occurring approximately every 22 years) to strike the Parkfield segment of the San Andreas fault dating back to the nineteenth century. In anticipation of the repeat event a variety of geophysical instruments have been operating in Parkfield since the mid-1980s. Unfortunately, data from these instruments show no discernable precursory phenomena to the magnitude zero level (Langbein *et al.*, 2005). Nevertheless, the 2004 event was extremely well recorded by the seismic stations of the California Integrated Seismic Network, and continuous GPS sites, and therefore offers the best opportunity to date to learn about the physics of earthquake rupture. With the numerous near-fault stations from the USGS and CGS strong motion networks high resolution models of the kinematic rupture process are obtainable.

In this report we present our preliminary kinematic modeling results using local and regional seismic waveform data and the continuous GPS data.

2.2 Inversion Method

In our preliminary modeling we used 8 seismic stations located at distances from 3 to 328 km from the epicenter (Figure 13.3). The data was bandpass filtered between 0.02 to 0.3 Hz to emphasize the low frequency nature of the source process. The stations that were used provide excellent azimuthal coverage of the ruptured fault.

Seismic Green's functions were computed with an f - k integration code using the GIL7 velocity model, which has been found to be suitable for the California Coast Ranges (e.g. Pasyanos *et al.*, 1996).

In addition to the seismic data we used 11 coseismic displacement measurements from near-fault continuous GPS sites (Figure 13.4). The coseismic data was obtained from the 1-second solutions by averaging from 10 minutes before to 2-10 minutes after the event, effectively removing the post-seismic signal.

The GPS Green's functions were computed for an elastic half-space (Okada, 1992) representing the average of the elastic parameters in the upper 12 km of the GIL7 seismic velocity model.

We used the inversion method of *Hartzell and Heaton* (1983), and we performed inversions using each data set separately and combined. We performed inversions using a dipping fault (from the moment tensor solution) and a vertical fault from relocated aftershocks and modeling of

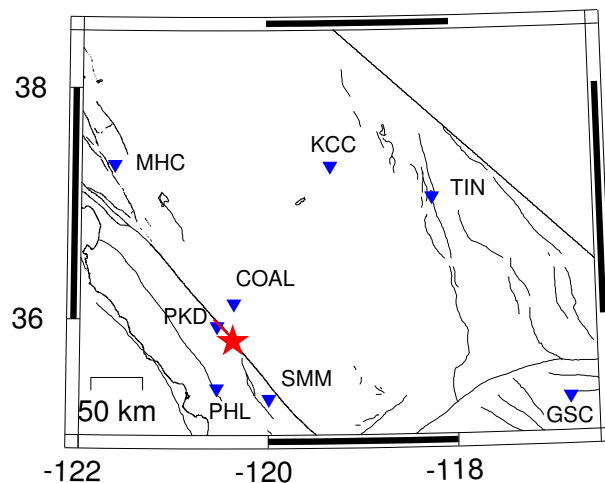


Figure 13.3: Location map. Seismic stations are shown as inverted triangles. The epicenter is shown as a star, and extent of fault model as a bold (red) line

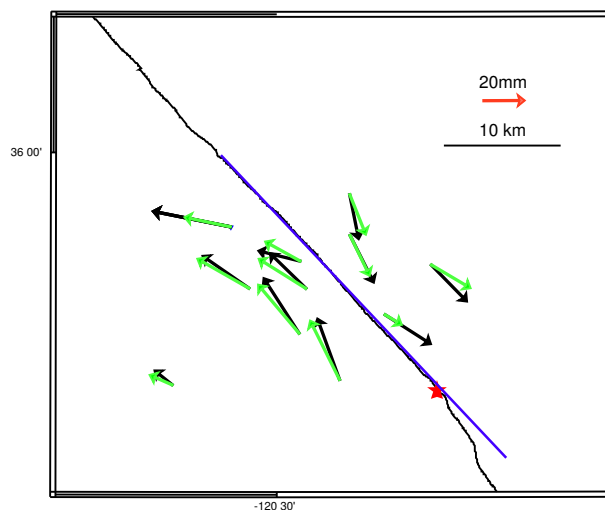


Figure 13.4: Observed GPS displacements (black) and predicted (green). The epicenter and assumed fault trace (blue line) are shown. The black line gives the distance scale, and the red arrow the GPS deformation scale.

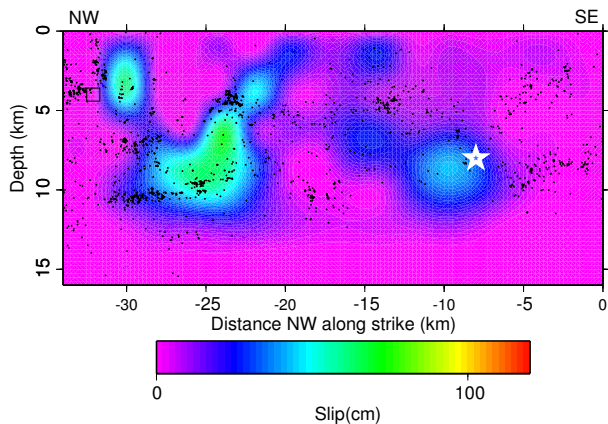


Figure 13.5: Smoothed slip distribution obtained from simultaneous inversion of seismic waveform and GPS data. The two deep asperities (5-12 km depth) are well constrained.

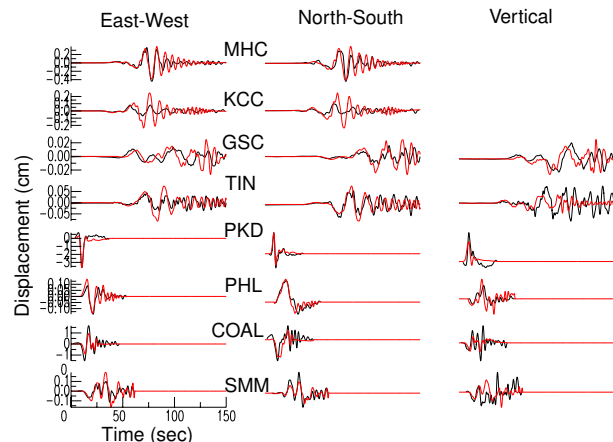


Figure 13.6: Observed (black) and predicted (red) displacement waveforms. The predicted waveforms are for the slip model shown in Figure 13.5

post-seismic deformation. These inversions showed that better fits were obtained with the vertical fault.

Inversions were performed with variable rake, however we found that it did not significantly improve fit so subsequent inversions assumed pure right-lateral slip.

Multiple time windows were used to model spatial variation in rupture velocity and rise time.

For the best fitting combined-data inversion result we obtained a scalar seismic moment of 1.17×10^{25} dyne cm, $M_w=6.0$, and rupture velocity of 3.0 km/s. The rise time is spatially variable, but is on average 1.2 seconds.

2.3 Slip Model

In Figure 13.5 the best-fitting combined-data inversion result is compared to double-difference relocated aftershocks (Hardebeck personal communication, 2004). The slip model shows an asperity located close to the hypocenter and another in the 12 to 5 km depth range about 20 km to the NW. The two deep patches of slip are well constrained by the seismic waveform and GPS data. The slip shallower than 5 km improves the fit to the GPS data, but is not well resolved.

Aftershocks tend to locate along the edges of the large slip patches in areas where the shear stress increased due to the fault rupture.

As shown in Figure 13.6 the kinematic slip model results in a very good level of fit to the seismic waveform data. The fit to the GPS data (Figure 13.4) is also good.

A surprising result is the NW rupture directivity. The directivity is well constrained by the regional seismic data. Inspection of the waveforms at the PKD and SMM stations (Figure 13.6) reveals significant differences in S-wave pulse width and amplitude that can only be explained by a NW propagating rupture. GPS data and

InSar inversion results (Ingrid Johanson, personal communication, 2005) similarly support the result that most of the mainshock slip was located NW of the epicenter. Interestingly strong motion stations to the SE have the largest peak values suggesting a component of SE-ward directivity (Shakel et al., 2005) that is not seen by the regional seismic waveform and the geodetic data sets. It is possible that the elevated strong ground motions SE of the epicenter are due to unaccounted for source process, and/or amplification effects due to the three-dimensional velocity structure of the San Andreas fault in this region (e.g. Michael and Eberhart-Phillips, 1991; Eberhart-Phillips and Michael, 1993). Our ongoing work is investigating both possibilities.

The slip in 2004 fills in the Parkfield segment that ruptured in 1934 and 1966, and therefore on this level the 2004 event is a typical repeat in the sequence of moderate Parkfield earthquakes. The 2004 rupture differs significantly however in that it nucleated at the SE end of the segment rupturing NW, while the two earlier events nucleated at the NW end rupturing SE (Bakun and McEvilly, 1979). This difference indicates that the actual triggering mechanism is very complex, and presently poorly understood. The 2004 event was possibly affected by a series of small events (M4-5) between 1992 to 1994, as well as the stress change caused by the nearby Mw6 Coalinga earthquake (Toda and Stein, 2002).

2.4 Ongoing Work

Our group is presently working on an updated kinematic rupture model for the 2004 earthquake by combining the GPS and regional waveform data set with the near-fault strong motion records and also the InSar-inferred deformation. This model will be used as a

boundary condition to calculate the stress change on the fault by solving the elasto-dynamic equations of motion using a finite-difference method (*e.g. Ide et al.*, 1997). The inferred stress change will be compared to observations of postseismic deformation and recurrence of characteristically repeating microearthquake sequences. Two of these sequences are the target sequences for the SAFOD deep borehole experiment.

Evidence of lateral velocity heterogeneity across the San Andreas fault (*Michael and Eberhart-Phillips*, 1991) might be an explanation for the elevated strong ground motions observed south of the epicenter. We will examine this possibility by performing finite-source simulations with 3D velocity structure to assess the impact of fault zone structure. In the longer term we will re-invert for kinematic slip parameters using 3D Green's functions.

The similarity and differences of the 2004 event to those that occurred in 1922, 1934, and 1966 is very important, and therefore we are also in the process of a reexamining the historical records for these earlier Parkfield events. With the constrained slip model for the 2004 event we will simulate motions for the various narrow band instrument types in operation at the time of the previous Parkfield earthquakes to ascertain the amount of information these waveforms carry with respect to the kinematic source process.

2.5 References

Bakun, W.H., and T.V. McEvelly, Earthquakes near Parkfield, California: Comparing the 1934 and 1966 sequences, *Science*, 205, 1375-1377, 1979.

Dreger, D. S., L. Gee, P. Lombard, M. H. Murray, and B. Romanowicz (2004). Rapid Finite-Source Analysis and Near-Fault Strong Ground Motions Application to the 2003 Mw6.5 San Simeon and 2004 Mw6.0 Parkfield Earthquakes, *Seism. Res. Lett.*, 2005.

Eberhart-Phillips, D., and A.J. Michael, Three-dimensional velocity structure and seismicity in the Parkfield region, central California, *J. Geophys. Res.*, 98, 15,737-15,758, 1993.

Hartzell, S. H., and T. H. Heaton, Inversion of strong ground motion and teleseismic waveform data for the fault rupture history of the 1979 Imperial Valley, California, earthquake, *Bull. Seism. Soc. Am.*, 73, 1553-1583, 1983.

Ide, S., and M. Takeo, Determination of constitutive relations of fault slip based on seismic wave analysis, *Journ. Geophys. Res.*, 102, 27,379-27,391, 1997.

Langbein, J., D. Dreger, J. Fletcher, J.L. Hardebeck, M. Hellweg, C. Ji, M. Johnston, J. R. Murray, R.M. Nadeau, M. Rymer, Preliminary Report on the 28 September 2004, M 6.0 Parkfield, California Earthquake, *Seism. Res. Lett.*, 76, 10-26, 2005.

Michael, A. J., and Eberhart-Phillips, D. M., Relationships between Fault Behavior, Subsurface Geology, and

Three-Dimensional Velocity Models, *Science*, 253, 651-654, 1991.

Okada, Y., Internal deformation due to shear and tensile faults in a half-space, *Bull. Seism. Soc. Am.*, 82, 1018-1040, 1992.

Pasyanos, M.E., D.S. Dreger, and B. Romanowicz, Toward Real-Time Estimation of Regional Moment Tensors, *Bull. Seism. Soc. Amer.*, 86, 1255-1269, 1996.

Shakel, A., V. Graizer, M. Huang, R. Borchert, H. Haddadi, K. Lin, C. Stephens, and P. Roffers, Preliminary analysis of strong-motion recordings from the 28 September 2004 Parkfield, California, earthquake, *Seism. Res. Lett.*, 76, 27-39, 2005.

Toda, S., and R.S. Stein, Response of the San Andreas Fault to the 1983 Coalinga-Nunez Earthquakes: An application of interaction-based probabilities for Parkfield, *J. Geophys. Res.*, 107, doi:10.1029/2001JB000172, 16pp., 2002.

3. The Parkfield Earthquakes: Then and Now

Margaret Hellweg and Bernard Dost (Koninklijk Nederlands Meteorologisch Instituut)

3.1 Introduction

When, in 1966, an earthquake of magnitude 6 occurred on the San Andreas Fault near the town of Parkfield, in central California, it caused excitement among seismologists for two reasons. First, a number of new seismic stations had just been installed near the epicenter and had recorded the quake; and second, many residents and seismologists could recall similar earthquakes which had happened there in 1922 and 1934, and had been recorded at regional seismograph stations. With the data from the new stations, seismologists were able to determine that the 1966 event had started to the NW of the town of Parkfield and had ruptured the fault to the SE. *Bakun and McEvilly* (1979, 1984) compared seismograms from the 1922, 1934 and 1966 Parkfield earthquakes. They found similarities in waveforms of the 1922 and 1934 events as recorded by the Bosch-Omori seismograph at the seismograph station at the University of California, Berkeley (BRK), 265 km NW of the epicenter. For the 1934 and 1966 events, they compared and found similarities in records from Wood-Anderson seismographs at Mount Hamilton (MHC), 185 km NW of the event, and at Santa Barbara (SBC), 185 km to its SE. In addition, they looked at recordings of the surface waves for all three events from the Galitzin seismograph in the Netherlands at DBN, almost 10,000 km away. This was one of the few stations world-wide which had good recordings from the same instrument for all three earthquakes. Thus, *Bakun and McEvilly* (1979, 1984) suggested that these events could be members of a sequence of characteristic earthquakes. In 1985, based in part on the waveform similarities for these events, *Bakun and Lindh* (1985) proposed that another, similar earthquake might again happen in the same place, perhaps around 1988. As part of a prediction experiment (*Bakun and Lindh*, 1985), many instruments were installed around the town of Parkfield to record such a quake and to determine whether any precursors might be observed.

3.2 Comparing seismograms

Since 1966, seismological instrumentation has changed. Early earthquakes were recorded on paper or perhaps on film. Now, we use digital recordings from broadband seismometers. These modern systems have many advantages: we know the transfer function of the instrument and can recover the true ground motion; the dynamic range is large, so we can analyse both small and large signals; and the frequency band of observations is wide, so we can observe both high and low frequency signals.

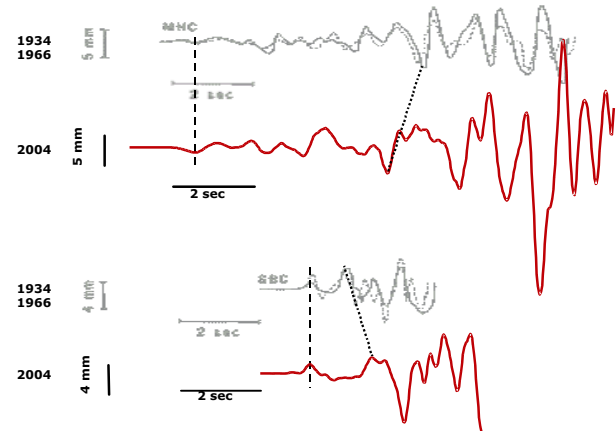


Figure 13.7: Comparison of the 2004 earthquake with events in 1966 (solid overplot) and 1934 (dashed overplot) for the stations MHC (top) and SBC (bottom). See text for details.

And finally, on September 28, 2004, another magnitude 6 earthquake occurred at Parkfield. Unlike the events in 1922, 1934 and 1966, this earthquake started well to the SE of the town of Parkfield, and ruptured NW. The rupture stopped about where the 1966 event had initiated (*Langbein et al*, 2005).

Fortunately, modern seismometers have been installed at the stations which *Bakun and McEvilly* (1979, 1984) used. We simulated the waveforms which would have been recorded for the 2004 Parkfield earthquake if old seismographs had still been running at the regional stations and at DBN.

At the regional stations, there are clear differences in the waveforms. These are probably related to the differences in the hypocenter and rupture direction of the 2004 event as compared to the earlier events. Figure 13.7 shows a comparison of P-wave records from the NS component of Wood-Anderson (WA) seismographs. The record for the 1934 is dashed and for 1966 solid (*Bakun and McEvilly*, 1979). These recordings are shown for the stations at MHC and SBA. Below each are WA traces for the 2004 event simulated from Berkeley Seismological Laboratory's station MHC and station SBA, which is a station of the Southern California Seismic Network operated by Caltech and the USGS. The records are on the

same scales and have been aligned on the P-wave. The WA records for the 2004 quake are clearly different from those of the earlier events. The Wood-Anderson amplitudes are proportionally larger at MHC than at SBC, and some phases arrive relatively earlier at MHC and later at SBC. These observations are consistent with NW rupture for the 2004 event, as compared to the SE rupture in 1966 and 1934.

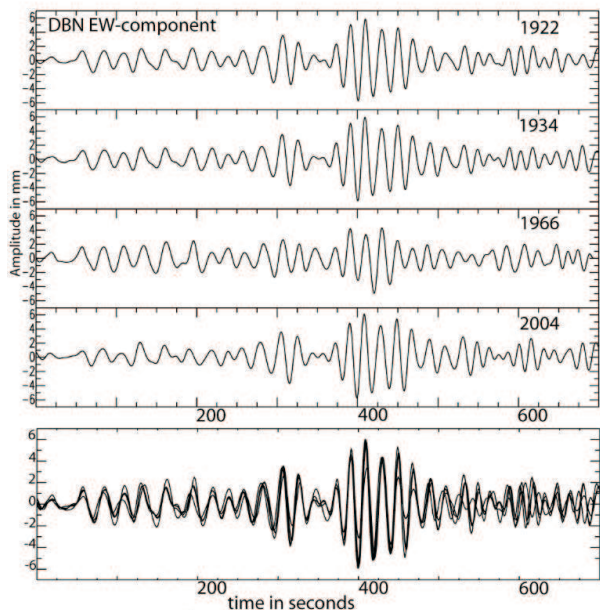


Figure 13.8: Comparison of the 2004 earthquake with the events in 1922, 1934 and 1966, as recorded at the teleseismic station DBN by a Galitzin seismograph. The amplitudes are given in mm recorded on the photographic paper. The records have been low pass filtered at 0.1 Hz. Below the seismograms for each event the recordings for the four events have been overplotted to emphasize their similarities.

Nearly 10,000 km from their epicenter, the events in 1922, 1934 and 1966 were recorded on light-sensitive paper by a set of horizontal Galitzin seismographs at De Bilt (DBN), the Netherlands. These seismographs were operated until 1994, when they were replaced by a 3-component, long period, digital seismometer, located at the same site. The modern instrument recorded the 2004 Parkfield earthquake.

In the records from DBN, there is some variation in the amplitudes of surface wave packets of the four events (Figure 13.8), although their phases seem to match quite well. For the comparison with the 2004 event, we have redigitized the photographic recordings of the horizontal components of the Galitzin seismographs for the 1922, 1934 and 1966 earthquakes. The waveform of the 2004 event closely resembles those of the 1922 and 1934 events.

The 1966 event deviates from the other three, especially for high frequencies. Amplitudes are comparable within the uncertainty in the gain, supporting the idea of a characteristic Parkfield earthquake (*Bakun and McEvilly, 1984*).

3.3 Perspectives

Before the 2004 event, the 1966 earthquake was the best-recorded of the Parkfield sequence. Stations of the Worldwide Standard Seismograph Network (WWSSN) were installed in the early 1960s, and recorded the 1966 earthquake at local, regional and teleseismic distances on paper records. The records were transferred to microchips (film), and recently some of them, including those from the Parkfield earthquake have been scanned as part of the Seismoarchives project at IRIS <http://www.iris.edu/data/SeismoArchives>. We plan to digitize these records from stations at all distances. Using rupture models for the 1966 and 2004 earthquakes, we will produce synthetic seismograms and compare them with the recordings for both events to investigate how well we can discriminate between these two very different rupture scenarios. Then, we will return to the even older data and apply what we have learned in order to better characterize this sequence of earthquakes.

3.4 References

- Bakun, W.H. and A.G. Lindh, The Parkfield, California, earthquake prediction experiment, *Science*, *229*, 619-624, 1985.
- Bakun, W.H., and T.V. McEvilly, Earthquakes near Parkfield, California: Comparing the 1934 and 1966 sequences, *Science*, *205*, 1375-1377, 1979.
- Bakun, W.H., and T.V. McEvilly, Recurrence models and Parkfield, California, earthquakes, *J. Geophys. Res.*, *89*, 3051-3058, 1984.
- Langbein, J., R. Borchardt, D. Dreger, J. Fletcher, J.L. Hardebeck, M. Hellweg, C. Ji, J. Johnston, J.R. Murray, R. Nadeau, M.J. Rymer, and J.A. Treiman, Preliminary report on the 28 September 2004, M 6.0 Parkfield, California earthquake, *Seismol. Res. Lett.*, *76*, 10-26, 2005.

4. A View of the 2004 Parkfield Earthquake from InSAR

Ingrid A. Johanson, Eric J. Fielding (JPL/Caltech), Roland Bürgmann

4.1 Introduction

The 2004 Parkfield earthquake was the long-awaited fulfillment of the USGS's Parkfield Prediction Experiment (Bakun and Lindh, 1985, Bakun and McEvilly, 1984). Since 1881 $M \sim 6$ earthquakes occurred near the town of Parkfield in Central California every ~ 20 years. After the event in 1966, the next earthquake was predicted to occur in 1988 ± 6 years. The years since the original prediction have seen the advent of space-based geodesy and now interferometric synthetic aperture radar (InSAR) data can now be added to the wealth of information on this earthquake. We present the results of a slip model encompassing the earthquake and two days of postseismic slip constrained by InSAR data from the ENVISAT satellite.

4.2 Interferogram processing

We use data from the European Space Agency's ENVISAT satellite, processed using ROIPAC software, developed at JPL. Phase unwrapping was performed by SNAPHU (Chen and Zebker, 2001) and was aided by a priori range change estimates from an inversion of GPS displacements during the interferogram time span. The contribution of topography to the interferogram phase was removed using a SRTM digital elevation model.

The ENVISAT satellite passed over the Parkfield area on September, 30 2004, two days after the Parkfield earthquake, on ascending track 435. We were able to make a pair with a previous ENVISAT acquisition from July 3, 2003. This interferometric pair is the most direct measure of the coseismic-only deformation field available using InSAR.

4.3 Data reduction

While the Parkfield earthquake has been highly anticipated, it is nonetheless a moderate sized event. As Figure 13.9 shows, the earthquake produced ground deformation resulting in 1 fringe (2π radians), corresponding to 28 mm of range change (change in distance between the ground and the satellite). This is comparable to the expected size of atmospheric errors in an interferogram (Zebker *et al.*, 1997). The interferogram also displays ground deformation due to groundwater movement. The signal from the Paso Robles Basin to the southwest (circled in Figure 13.9) is particularly noticeable. We have pared the interferogram down to just the immediate vicinity of the Parkfield earthquake (dashed line in Figure 13.9) and removed areas affected by groundwater

induced vertical motion in the Paso Robles and Salinas basins and topography-correlated atmospheric errors to the East and South.

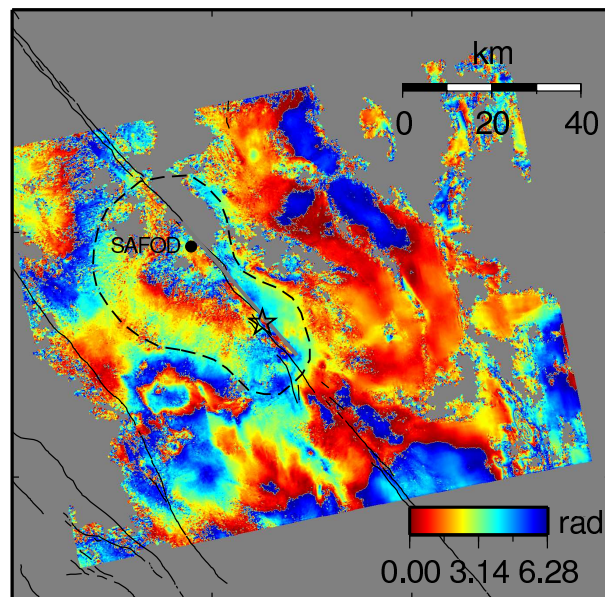


Figure 13.9: Interferogram from 7/3/2003 to 9/30/2004. Star is the epicenter of the 2004 Parkfield earthquake, dashed line borders area used in the inversion and dot is the location of the San Andreas Fault Observatory at Depth (SAFOD). Color scale is from 0 to 2π and repeats.

For the inversion, the geocoded and trimmed interferogram was sub-sampled on a grid with 1 km spacing. We correct our interferogram samples for coseismic and postseismic slip from the San Simeon earthquake and interseismic motion using an unpublished model based on GPS and InSAR and the model of Rolandone *et al.* (2004), respectively.

4.4 Model Results

The model plane is vertical with a strike of 319 degrees. We discretize the plane into 300 2 km x 1 km elements and perform a least squares inversion while seeking a smooth distribution of right-lateral slip. The results are shown in Figure 13.10. The slip model contains two high-slip asperities: one just above the hypocenter (red star in Figure 13.10) and a larger asperity to the northwest. Much of the slip in our model occurs within the area outlined by aftershocks as shown in Figure 13.10. Langbein *et al.* (2005) note that the relocated aftershocks occur

in the same clusters and streaks as the pre-earthquake background seismicity, including a streak which is visible in the aftershocks at about 5 km depth. One interpretation of microseismicity streaks is that they occur at the boundaries of creeping and locked asperities of the fault surface. Assuming that in an earthquake the strong asperity makes up its slip deficit by slipping more than the surrounding creeping sections, the microseismic streak would be expected to bound areas of high coseismic slip. The streak of aftershocks at 5 km depth occurs near the top of the northwest asperity, and could be interpreted as weakly bounding it.

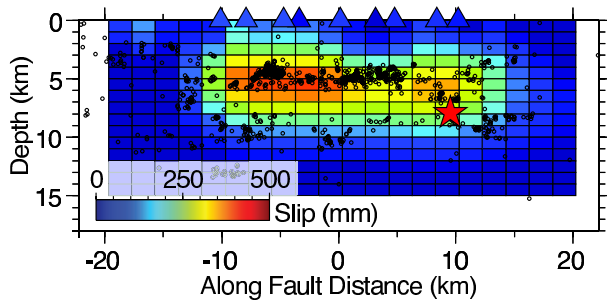


Figure 13.10: Results of inversion for slip during the 2004 Parkfield earthquake and two days of postseismic slip. Red star is earthquake hypocenter, black circles are double-difference relocated aftershocks (Langbein *et al.*, 2005), and colored triangles are surface offsets measured by creepmeters. X-axis datum is GPS station Carr Hill (CARH)

Creepmeter measured surface offsets are plotted as colored triangles in Figure 13.10 for comparison. Many of the creepmeters on the main SAF trace went off scale either during or soon after the earthquake. Between Sep. 30 and Oct. 2, these creepmeters were brought back on scale and an offset was manually measured. The triangles in Figure 13.10 represent the total creep measured when the creepmeters were brought back on scale. The top row of our model matches the overall magnitude and some of the features of the creepmeter surface slip distribution. Both show more surface slip 0-10 km north of Carr Hill than to the south.

The total moment of our model is 2.56×10^{18} Nm; equivalent to $M_w 6.2$. Seismic modelling of the coseismic rupture has estimated a moment magnitude $M_w 6.0$, which would require 1.32×10^{18} Nm ($M_w 6.0$) of the slip in our model to have occurred within the first two days of the postseismic period. An analysis of additional InSAR and GPS data spanning three months post-earthquake, suggests that 1.48×10^{18} Nm ($M_w 6.1$) of moment was subsequently released postseismically (Johanson *et al.*, submitted). Johanson *et al.* (submitted) find that aseismic slip could account for as much as 70% of the total

(coseismic and postseismic) moment release of the Parkfield earthquake.

4.5 Acknowledgements

This work was funded by SCEC and NSF grant EAR-0337308

4.6 References

- Bakun, W. H., and A. G. Lindh, The Parkfield, California, earthquake prediction experiment, *Science*, *229*, 619-624, 1985.
- Bakun, W. H., and T. V. McEvilly, Recurrence models and Parkfield, California, earthquakes. *Journal of Geophysical Research* *89*, 3051-3058, 1984.
- Chen, C. W., and H. A. Zebker, Two-dimensional phase unwrapping with use of statistical models for cost functions in nonlinear optimization, *J. Opt. Soc. Am. A Opt. Image Sci.*, *18*, 338-351, 2001.
- Johanson, I. A., E. J. Fielding, F. Rolandone, and R. Bürgmann, Coseismic and Postseismic Slip of the 2004 Parkfield Earthquake from Space-Geodetic Data, *Bull. Seismo. Soc. Am.*, submitted.
- Langbein, J., R. Borchardt, D. Dreger, J. Fletcher, J. L. Hardebeck, M. Hellweg, C. Ji, M. Johnston, J. R. Murray, and R. Nadeau, Preliminary Report on the 28 September 2004, M 6.0 Parkfield, California Earthquake, *Seismol. Res. Lett.*, *76*, 10-26, 2005.
- Rolandone, F., I. Johanson, R. Bürgmann, and D. Agnew, Variation in aseismic slip and fault normal strain along the creeping section of the San Andreas fault from GPS, InSAR and trilateration data, *Eos, Trans., AGU*, *85*, G32A-05, 2004.
- Zebker, H. A., P. A. Rosen, and S. Hensley, Atmospheric Effects in Interferometric Synthetic Aperture Radar Surface Deformation and Topographic Maps, *J. Geophys. Res.*, *102*, 7547-7563, 1997.

5. Frictional Afterslip Following the 2004 Parkfield, California Earthquake

Kaj M. Johnson, Roland Bürgmann, and Kristine Larson (University Colorado)

5.1 Introduction

The abundance of geodetic and seismic data recording postseismic deformation following the 2004 Parkfield earthquake provides an unprecedented opportunity to resolve frictional properties on the Parkfield section of the San Andreas fault. The Parkfield segment transitions between the locked section to the southeast that last ruptured in the 1857 Fort Tejon earthquake and the creeping section to the northwest. We develop 3D rate- and state-dependent friction models of afterslip following the 2004 earthquake to investigate the frictional behavior of the fault. It is assumed that the coseismic rupture occurred on an area of the fault surrounded by aseismic creep that accelerated after the earthquake. We estimate the distribution of coseismic slip, afterslip, and rate-state frictional parameters by inverting a two-step slip model. In the model we: 1) estimate the coseismic slip distribution from 1 Hz GPS data, and 2) use the corresponding coseismic shear stress change on the fault as input into a numerical afterslip model governed by rate-state friction. We find the rate-state frictional parameter A-B, which is an indicator of frictional stability, is in the range $10^{-4} - 10^{-3}$ at 50 MPa normal stress, about an order of magnitude lower than experimental values for granite at conditions well above or below the transition from potentially unstable (negative A-B) to nominally stable (positive A-B) friction. The estimate of A-B values fall within a wide range of experimental values reported for Serpentine which crops out along the San Andreas fault zone. The critical slip distance, d_c , which characterizes the distance over which strength breaks down during a slip event, is in the range 0.01-0.1 m, consistent with seismic estimates and a fault gouge thickness of 1-10 m. The afterslip model reproduces most features observed in the GPS time-series data including high surface velocities in the first few months after the earthquake and lower rates at later times, as well as the cumulative postseismic displacement. The model tends to under-predict the displacement data at later times, suggesting that perhaps the modeled afterslip period ends too quickly or an un-modeled deformation process dominates the signal at later times.

5.2 The model

To model afterslip at Parkfield we discretize a 65-km-long segment of the San Andreas fault into rectangular patches of uniform slip dislocations in a homogeneous elastic half-space. We assume the slip rate distribution

on the fault prior to the earthquake is that estimated by *Murray et al.* (2001) who inverted GPS velocities averaged over 1991-1998 for the interseismic slip rate. Also following *Murray et al.* (2001), we assume the fault is locked down to 15 km depth to the southeast of Parkfield, creeping at 25 mm/yr down to 15 km depth northwest of Parkfield, and creeping at 32 mm/yr everywhere below 15 km depth. These large creeping sections of the fault are assumed to extend infinitely along the strike of the San Andreas fault.

We envision that the area of the fault bounded by micro-seismicity (*Nadeau et al.*, 2005) is locked between earthquakes and is surrounded by aseismic fault creep. The locked part of the fault ruptures during the earthquake and creep in the surrounding areas accelerates to relax the coseismic stress load. We assume the coseismic stresses relax during afterslip according to the following Dieterich-Ruina formulation of rate-state friction, equations (1) and (2), together with the equation relating stress on the fault to slip

$$\tau = \sigma \{ \mu + A \ln(V/V^*) + B \ln(V^* \theta / d_c) \} \quad (13.1)$$

$$\frac{d\theta}{dt} = 1 - \frac{V\theta}{d_c} \quad (13.2)$$

where τ is shear stress on the fault, σ is the normal stress, V is sliding velocity, V^* is a reference velocity, μ is the nominal coefficient of friction at the steady reference velocity, θ is a state variable that evolves with time, A and B are laboratory-derived constants, and d_c is the so-called critical slip distance. d_c is interpreted as an indication of the size of asperity contacts and is thought of as the slip necessary to renew surface contacts. In this formulation, the state, θ , can be interpreted as the average asperity contact time because it increases linearly with time at zero slip velocity.

The conditions on stress and state before the earthquake are obtained from the interseismic slip rate distribution (*Murray et al.*, 2001) assuming steady state conditions ($d\theta/dt = 0$). The initial condition on stress immediately after the earthquake (the beginning of the afterslip period) is the pre-earthquake stress plus the stress change caused by the earthquake.

The objective is to invert GPS data with a forward model of the coseismic and postseismic processes to obtain estimates of the frictional parameters, A , B , and d_c . The two-step forward model produces a coseismic slip distribution and the resulting afterslip distribution that is driven by the coseismic stress change. In the first step,

we perform a linear slip inversion of the coseismic GPS data for the coseismic slip distribution. In the second step, we specify the rate-state friction parameters and initial conditions and solve for the evolution of afterslip as. σA , σB , and D_c vary linearly with depth.

5.3 Results

Figure 13.11 shows the best-fitting coseismic slip and afterslip distributions. The cumulative afterslip after 9 months is shown. The afterslip is largely localized within two patches. One patch is in the upper 5 km, just above the larger coseismic slip patch. The other patch of afterslip occurs above the hypocenter.

The fit to the GPS time-series is shown in Figure 13.12. The model reproduces the rapid postseismic velocities during the first 0.1-0.2 years and the less rapid velocities during the later time periods. There is a tendency for the model to under-fit the displacements at later times indicating that the model relaxes and returns to the pre-earthquake rate too quickly. This may indicate that another (un-modeled) deformation mechanism, such as deep distributed flow, may dominate the signal at later times.

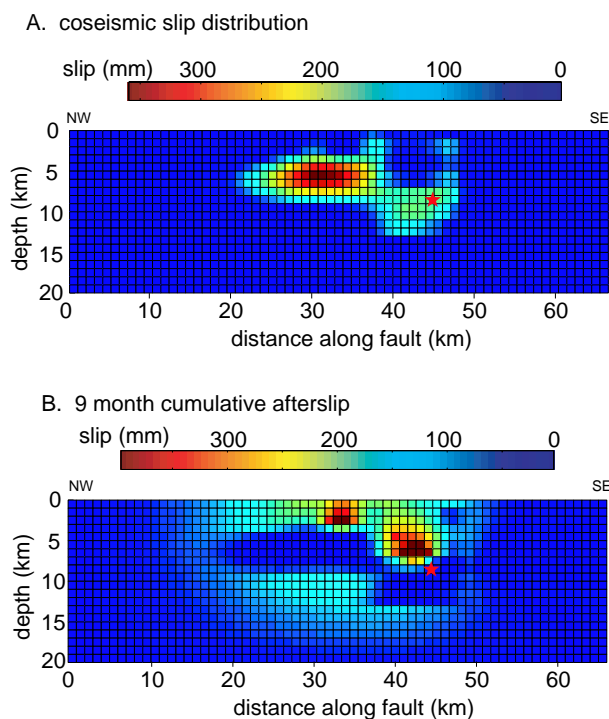


Figure 13.11: A. Best-fitting coseismic slip distribution and, B. corresponding 9-month cumulative rate-state afterslip.

Table 1 shows the approximate 95% confidence intervals on the frictional parameters. The values for A and B assume a uniform effective normal stress on the fault of

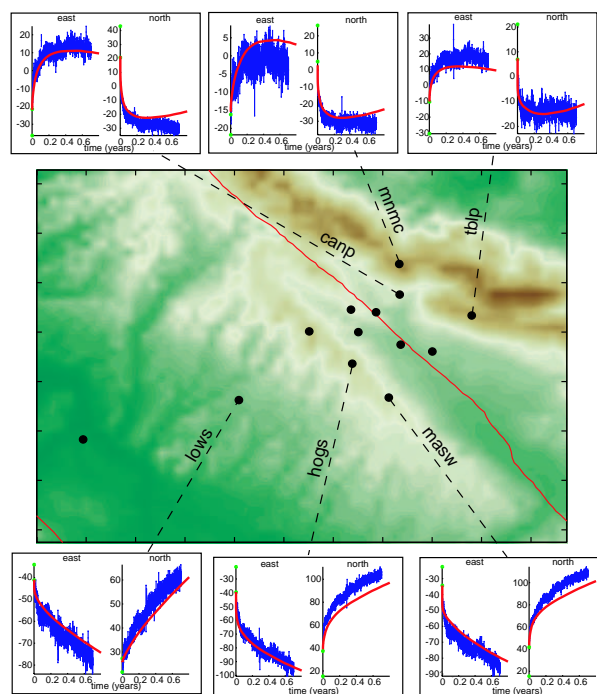


Figure 13.12: Fit to the postseismic GPS time series. Only a subset of data is shown because of space limitations. Data shown with 95% confidence error bars. Solid line is model. Vertical axis is displacement in mm.

50 MPa. The parameters vary linearly with depth, so we report the values at the center of the top and bottom rows of patches. A-B is on the order of 10^{-4} to 10^{-3} , which is about an order of magnitude lower than experimental values for granite at conditions well above or below the transition from potentially unstable (negative A-B) to nominally stable (positive A-B) friction. It is also an order of magnitude lower than an estimate from an afterslip inversion of the Tokachi-oki, Japan, earthquake (*Miyazaki et al.*, 2004). However, the estimated A-B values fall within a wide range of experimental values reported for Serpentine, which crops out along the San Andreas fault zone and is frequently mentioned as an important factor allowing for velocity-strengthening behavior of some faults (*Reinen et al.*, 1994). The low values of A-B might be indicative of a transition zone from velocity-weakening (negative A-B) to velocity-strengthening (positive A-B). Estimates of d_c are of the order 0.01-0.1 m, in reasonably good agreement with the seismic estimate near Parkfield (*Fletcher and Spudich*, 1998). The scaling relationship of *Marone and Kilgore* (1993) infers a fault gouge thickness of 1-10 meters.

5.4 Acknowledgements

This work is funded partially by NSF grant EAR-0309946.

Table 13.1: Table 1. 95% Confidence intervals on frictional parameters

parameter	top of fault	bottom of fault
A	0.0004-0.0052	0-0.024
B	0-0.0045	0-0.0468
A-B	0.0006-0.0018	0.0001-0.0021
d_c (meters)	0.020-0.250	0-0.650

5.5 References

Fletcher, J.B., and P. Spudich, Rupture characteristics of three $M \sim 4.7$ (1992-1994) Parkfield earthquakes, *Journal of Geophysical Research*, *103*, 835 - 854, 1998.

Marone, C., and B. Kilgore, Scaling of the critical slip distance for seismic faulting with shear strain in fault zones, *Nature*, *362*, 618-621, 1993.

Miyazaki, S., Segall, P., Fukuda, J., and T. Kato, Space time distribution of afterslip following the 2003 Tokachi-oki earthquake: Implications for variations in fault zone frictional properties, *Geophys. Res. Lett.*, *31*, doi: 10.1029/2003GL019410, 2004.

Murray, J.R., Segall, P., Cervelli, P., Prescott, W., and J. Svare, Inversion of GPS data for spatially variable slip-rate on the San Andreas fault near Parkfield, *Geophysical Research Letters*, *28*, 359 - 362, 2001.

Nadeau, R.M., Foxall, W., and T.V. McEvilly, Clustering and periodic recurrence of microearthquakes on the San Andreas fault at Parkfield, California, *Science*, *267*, 503 - 507, 1995.

Reinen, L.A., Weeks, J.D., and T.E. Tullis, The frictional behavior of Lizurdite and Antigorite Serpentinites: Experiments, constitutive models, and implications for natural faults, *Bulletin Seismological Society of America*, *143*, 317-358, 1994.

6. The Orinda Earthquake Sequence: Scaling of Small Earthquakes

Margaret Hellweg

6.1 Introduction

Does the faulting in large and small earthquakes involve different physical processes? This question remains open because of the pervasive difficulty in geophysics of performing controlled experiments. To find the answer, it is necessary, for example, to separate source from path and site effects in seismograms. A sequence of small earthquakes which occurred near Orinda, California, offers an opportunity to explore this question. This sequence occurred under Berkeley Seismological Laboratory's station BRIB (37.92 N, 122.15 W). At the surface are a broadband seismometer and an accelerometer. In addition to the surface installation, there is a borehole at the station equipped with a 3-component geophone and a 3-component accelerometer at a depth of 119 m. The sequence began on October 19, 2003, at 14:35:27 UTC, with an earthquake with M_d 2.5. The mainshock (MS) with M_L 3.5 followed about an hour later. In the next week and over the course of the next 3 months there were more than 4000 aftershocks ranging in magnitude from -2.5 to 3.4.

6.2 The largest events

The two largest earthquakes of the sequence were the mainshock on October 19, at 15:32 UTC with M_L 3.5, and an aftershock at 17:50 on October 20, with M_L 3.4 (Figure 13.13). For these two events one of the horizontal components of both the surface and the borehole seismometers was clipped. The black traces in Figure 13.13 show the seismometer records. Fortunately, the clipped component of the borehole seismometer coincides with the single functioning component of the borehole accelerometer. When the instrument response is removed from the accelerometer recording and the trace is integrated, it matches the corresponding component of the velocity sensor (gray traces in Figure 13.13). The offset traces at the beginning of the records in Figure 13.13A show a small event which occurred 1.5 s before the mainshock. These traces, scaled to be 100,000 times those for the mainshock, show some of the range of sizes of the events in this sequence. The large aftershock appears to be a double event (Figure 13.13B) with two clear P and two clear S phases.

6.3 Event magnitudes

How small are the smallest earthquakes in this sequence that we can see in the record? For most of the events, standard magnitudes cannot be determined:

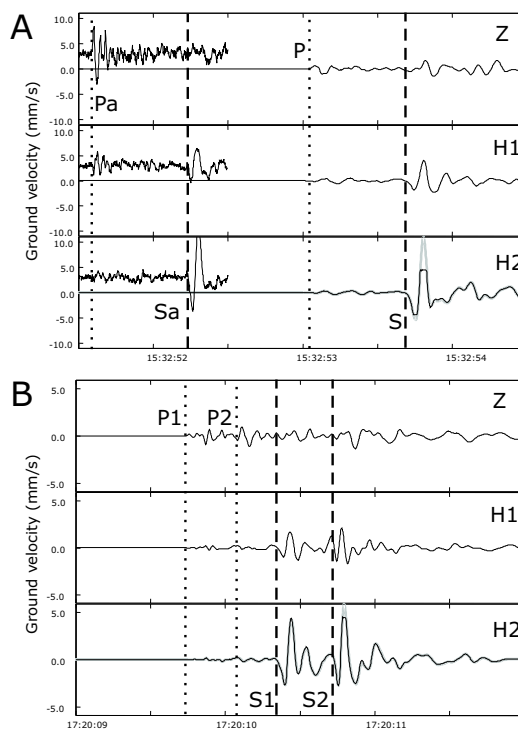


Figure 13.13: Seismograms of the mainshock (A) and largest aftershock (B). Z, H1 and H2 are the vertical and orthogonal horizontal components, respectively. The H2 geophone (black) was clipped for these two events, so the gray trace shows the instrument-corrected accelerometer record. Dotted and dashed lines show P- and S-arrivals, respectively. (A) About 1.5 s before the mainshock, a small event occurred. Its traces have been multiplied by 100,000. (B) The large aftershock appears to be a double-event. The P- and S-phases of the first and second event are indicated.

the events are too small to be recorded at other stations and, strictly speaking, the local magnitude scale is not defined for events so close to the recording station. To determine the magnitude threshold for the events, I calibrated a manual magnitude scale using events from the catalog. Following the definition of local magnitude (Richter, 1935), I measured the peak-to-peak amplitudes in the instrument-corrected velocity seismograms of the two horizontal components of the borehole velocity sensor and multiplied by the period and by the magnification of a Wood-Anderson instrument at that period. As the distances of these events from the station BRIB are all nearly the same, no distance correction is necessary.

Figure 13.14 shows a comparison between the catalog and manual magnitudes (gray dots). The line shows the least-squares regression between the catalog and manual magnitudes and allows the manual magnitudes to be projected to corresponding catalog magnitudes (black dots). The smallest events analysed correspond to M_L -1.5; however, there are still smaller events in the seismograms from the borehole geophone. No manual magnitudes have been determined for these tiny earthquakes yet, but the smallest events recorded at station BRIB are more than five units of magnitude smaller than the mainshock.

6.4 Perspectives

Many different interesting questions can be explored using this dataset. One of the most fundamental in terms of earthquake physics is the question of scaling: does the same thing happen in tiny events as in the large events which capture public attention. However, this sequence also offers a view into the relationship of mainshocks and aftershocks for small earthquakes. Normally, only a few aftershocks with magnitudes between 0.5 and 3.5 would make it into the catalog. For the Orinda MS, more than 4000 aftershocks have been recorded and are available for analysis. It should be possible to map their locations with respect to the MS, and perhaps determine its rupture surface independently. Other perspectives include investigations of the effects of path attenuation on the frequency content of small events.

6.5 References

Richter, C.F. An instrumental earthquake magnitude scale. *Bull. Seismo. Soc. Am.*, 25, 1-32, 1935.

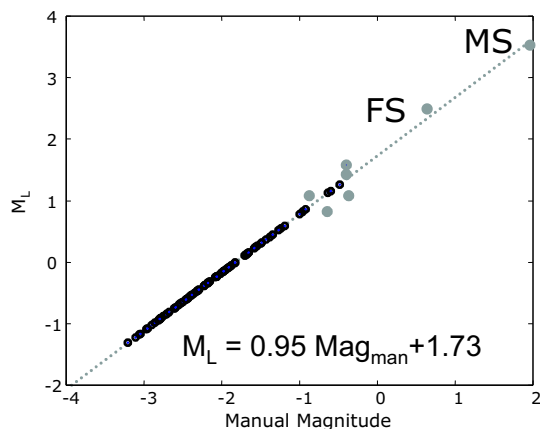


Figure 13.14: Magnitude calibration. Gray dots show the events from the Orinda sequence which are in the NCSN catalog. A least-squares regression (line) allows M_L to be determined for the many small events.

7. Inversion for the Velocity Structure of the Santa Clara Valley, California

David Dolenc, Doug Dreger, and Shawn Larsen (LLNL)

7.1 Introduction

In our previous work we investigated teleseismic, local, and microseism data recorded by the 41-station seismic array in the Santa Clara Valley (SCV) (Figure 13.15). We have found strong correlations between basin depth reported in the USGS 3D seismic velocity model (ver. 2) (*Jachens et al.*, 1997) and different relative measures of ground motion parameters such as teleseismic arrival delays, P-wave amplitudes, wave energy, local earthquake S-wave amplitudes, and periods of microseism horizontal to vertical spectral ratio peaks (*Dolenc et al.*, 2005; *Dolenc and Dreger*, 2005). The teleseismic, local earthquake, and microseism observations were also found to be strongly correlated with one another. The results suggested that all three datasets are sensitive to the basin structure (Figure 13.16) and could therefore be used together to improve the 3D velocity model.

7.2 Method

We started to develop a simultaneous inversion of the teleseismic, local, and microseism observations to refine the seismic velocity model within the SCV basins. To reduce the extremely large model space, we only invert for the velocity structure within the basins while the basin geometry, as defined in the USGS velocity model, is held fixed. The inversion is based on the approach described in *Aoi* (2002). We parameterize the velocity model in the basins and invert it by using teleseismic P-wave waveforms as well as additional relative parameters, such as teleseismic wave energy, local earthquake S-wave amplitude, and periods of microseism horizontal to vertical spectral ratio peaks. The model parameters are determined by the inversion with the constraint that the observation equation, which is nonlinear in the model parameters, is best satisfied in the sense of least squares. The observation equation is linearized by omitting higher order terms and solved iteratively by singular value decomposition. To solve the observation equation, synthetic waveforms as well as sensitivity functions (differential seismograms) are required. The 3D elastic finite-difference code (*Larsen and Schultz*, 1995) is used to calculate waveforms, and the sensitivity functions are obtained numerically by taking the difference of waveforms from perturbed and unperturbed models. The inversion is performed in the 0.1 to 1 Hz passband in which the SCV seismic experiment observations had a good signal to noise ratio.

We prepared four variations of the USGS model in the

basins: (1) laterally uniform velocity with a single vertical velocity gradient, (2) three regions of vertical velocity gradient distributed vertically, (3) six 1-km thick horizontal layers with constant velocities, and (4) multi-layered constant velocity slices draped over the basin geometry.

Because of the computational limitations, the slowest velocities in the models were increased to a minimum S-wave velocity of 1 km/s. The slowest P-wave velocity was 1.75 km/s. To model the plane wave from the teleseismic events, we used a disc of point sources in the deepest homogeneous layer of the velocity model, representing the upper mantle. To simulate the microseisms, we used a localized source of isotropic Rayleigh waves located offshore. The preliminary results of the f-k analysis of the observed and simulated microseisms display strong directionality in their propagation and localization of the source, which supports the use of the point source for microseisms.

Preliminary results show that the model parameters are iteratively modified and that the residuals between the data and synthetic seismograms are converging.

7.3 Conclusions

Previous results showed strong correlations between the SCV basin depth reported in the USGS 3D seismic velocity model and different relative measures of ground motion parameters observed for the teleseismic and local events, as well as microseisms. We are developing a simultaneous inversion of observations from the three datasets to refine the seismic velocity model in the SCV basins.

7.4 Acknowledgements

Part of this work was supported by the USGS grants 99HQGR0057 and 00HQGR0048. The Hellman Faculty Fund is acknowledged for partial support.

7.5 References

- Aoi, S., Boundary shape waveform inversion for estimating the depth of three-dimensional basin structures, *Bull. Seism. Soc. Am.* 92, 2410-2418, 2002.
- Dolenc D., D. Dreger, and S. Larsen, Basin structure influences on the propagation of teleseismic waves in the Santa Clara Valley, California, *Bull. Seismol. Soc. Am.*, 95, 1120-1136, 2005.
- Dolenc D. and D. Dreger, Microseisms observations in the Santa Clara Valley, California, *Bull. Seismol. Soc.*

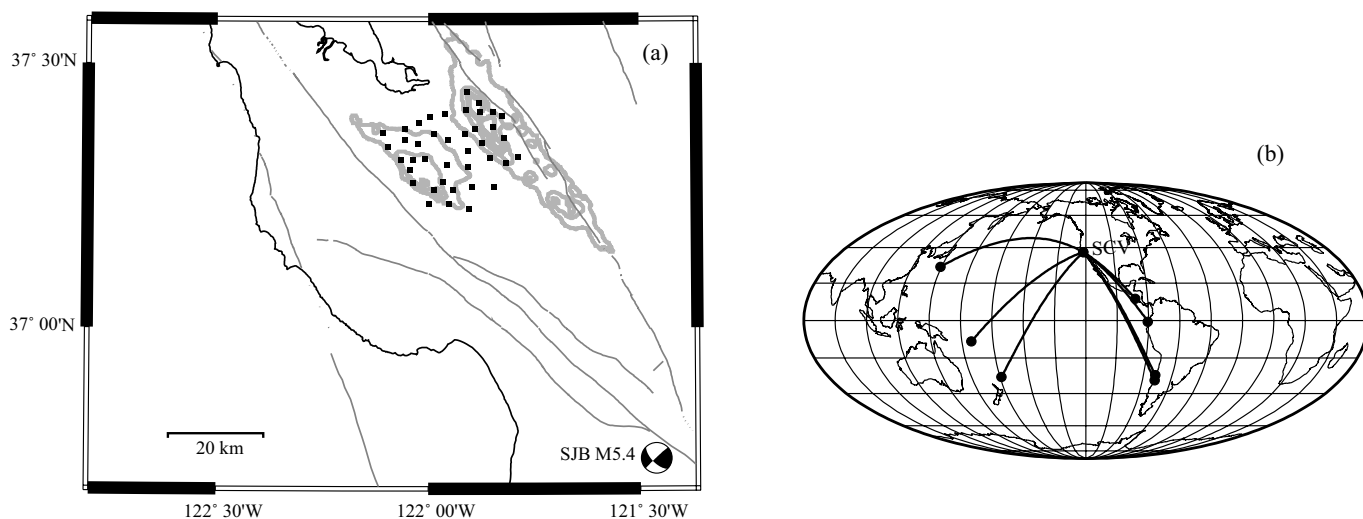


Figure 13.15: (a) Location of the SCV seismic array. Contours of the basins from the USGS model at 1km, 3 km, 5 km, and 6 km depth are shown in gray. Focal mechanism for the San Juan Bautista M_L 5.4 event is shown. (b) Locations of the teleseismic events used in the study.

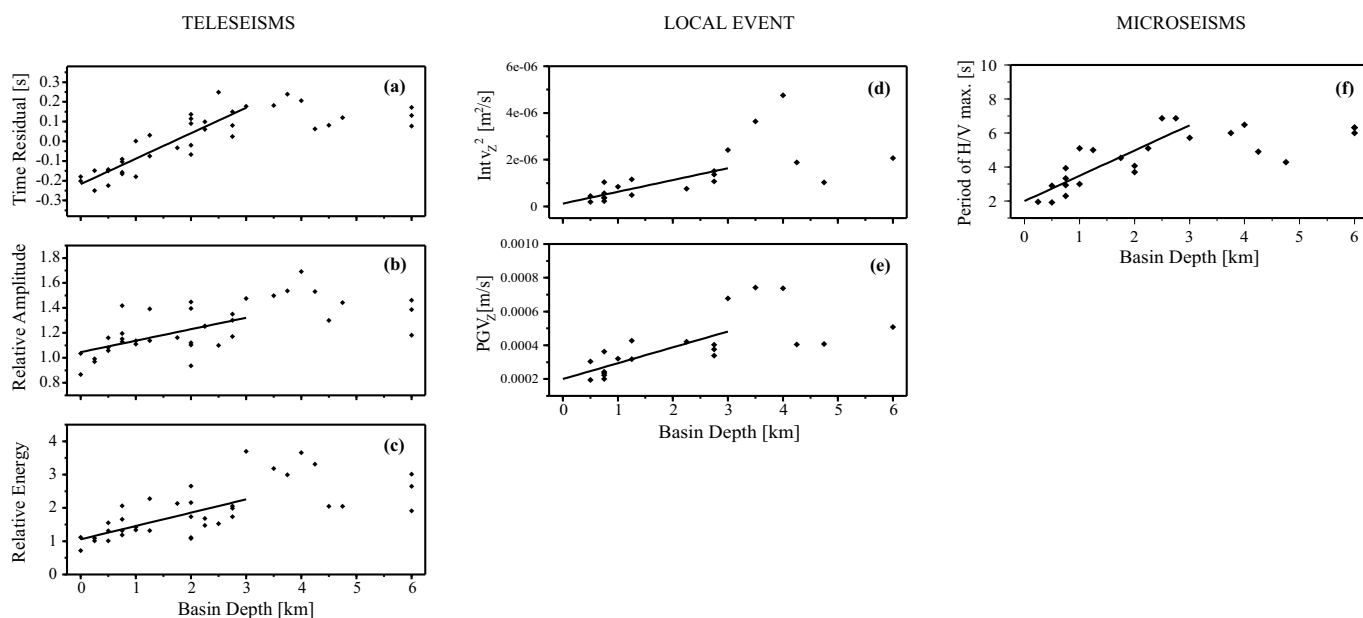


Figure 13.16: Correlations between different relative measures of ground motion parameters and USGS model basin depth. (a) Travel-time residuals, (b) relative amplitudes, and (c) average P-wave energy averaged over the teleseismic events shown in Figure 13.15b as a function of the USGS model basin depth. (d) Integrated squared vertical velocity and (e) vertical PGV measured for the San Juan Bautista event as a function of the USGS model basin depth. (f) Period of the microseisms H/V peak as a function of the USGS model basin depth.

Am., 95, 1137-1149, 2005.

Jachens, R. C., R. F. Sikora, E. E. Brabb, C. M. Wentworth, T. M. Brocher, M. S. Marlow, and C. W. Roberts, The basement interface: San Francisco Bay area, California, 3-D seismic velocity model, *EOS Trans. AGU* 78,

F436, 1997.

Larsen, S. and C. A. Schultz, ELAS3D: 2D/3D elastic finite-difference wave propagation code, *Technical Report No. UCRL-MA-121792*, 19 pp, 1995.

8. Analysis of Bridge Structures Crossing Fault Rupture Zones: Seismic Ground Motion Simulation

Douglas Dreger, Gabriel Hurtado (CEE) and Anil Chopra (CEE)

8.1 Introduction

Bridges that cross faults can be subjected to large dynamic and static ground motions. As there are very few actual ground motions recorded very close to ruptured faults ($< 100\text{m}$), ground motion simulation is the only viable way to obtain time histories for structural analysis. Professors Dreger (BSL) and Chopra (CEE) are collaborating on a Caltrans funded project investigating the response of bridges that cross faults with the objective of developing simplified methods that can be applied to bridge design. In this report the ground motion simulation part of the effort is described.

The bridges being considered have a minimum span of 30m, and therefore the simulation method must be capable of calculating seismic response time histories at this small distance from the fault. In addition, the method must accurately account for the near-fault source radiation pattern, far- and near-field seismic radiation, and have the ability to characterize motions for a broad range of fault types (e.g. vertical strike-slip and reverse faulting), as well as variable slip and full kinematic description of the rupture process. We must be able to accurately simulate the directivity effect as well as the sudden elastic rebound sometimes referred to as fling.

8.2 Simulation Method

The simulation method that we use is a 4th order accurate staggered-grid finite-difference code, e3d, developed at Lawrence Livermore National Laboratory (LLNL) (Larsen and Schultz, 1995). An advantage of this code is that it has been tested, and calibrated in a PEER/SCEC funded effort to validate numerical methods for ground motion simulation.

In addition, e3d simulates complete seismic waveforms in terms of near- intermediate- and far-field terms of the solution to the elasto-dynamic equation of motion. At such a close distance the fault all of these terms are important in strong ground motion generation.

We use a very fine model discretization of 20m. Motions at the closest stations to the fault (15m) are obtained by interpolation, and have been verified analytically for the strike-slip case. This high spatial resolution has the advantage that the kinematic source model also has high resolution producing a smooth evolution of the rupture front and the slip time function. The drawback of course is that it is computationally very expensive.

We simulate motions for a Mw6.5 earthquake using *Wells and Coppersmith* (1994) to estimate the fault

length and width. From the scalar seismic moment and the fault area the average slip is specified. We use *Somerville et al.*, (1999) to specify the slip rise time from the moment. Simulations have been performed for models ranging from a pure vertical strike-slip event to a 20-degree dipping thrust fault. We have tested rupture velocities of 70% and 140% (super-shear) of the shear wave velocity, although most of the simulations are for 80% of the shear wave velocity as is commonly reported in the literature for moderate earthquakes. We are in the process of setting up a distributed slip and variable rise time simulation to assess the effect of such source complexity on very near-fault strong ground motion.

The initial models are simplified greatly and using the finite-difference approach is "over-kill", but in the future we may consider more complex source functions and 3D fault structures such as velocity discontinuities across the fault or low-velocity fault gouge. It is desirable that the ground motion computation and the source resolution are at the same resolution, and in the future when comparisons are made with more complex models all of the ground motions will have been computed with the same theory and numerical algorithm.

The total model dimension is $50 \times 20 \times 15 \text{ km}^3$ and with the grid spacing of 20m this translates to 2.3 billion grid points, requiring 121.8 Gbytes of memory. The simulations were performed on a LLNL super computer.

8.3 Vertical Strike-Slip Results

Arrays of stations are located along the length of the fault. Subarrays 1 and 8 are located off the end of the fault. Subarrays 2 and 7 are at the two ends of the fault, subarrays 3-6 are along the fault trace. On each side of the fault the two closest stations are 15m from the fault. The hypocenter is located beneath subarray 3.

The displacement seismograms at the closest station to the fault for each subarray are shown in Figure 13.17. Static offsets are observed on the FP component at sites adjacent to the fault. The static offsets are due to the sudden elastic rebound of the fault and are sometimes referred to as fling. The static offset on one side of the fault shows one-half of the total differential motion across the fault. The sign of the static offset is opposite at the stations on the other side of the fault. The FP component static offsets are reduced in amplitude at the two sites at the end of the fault (subarrays 2 and 7). This is due to the elastic response of the medium around the fault in which "push" and "pull" quadrants result in deformation that

is not parallel to the fault strike. At these two sites, for the same reason, the FN component also shows a static offset. There are negligible static offsets at sites located off of the ends of the fault.

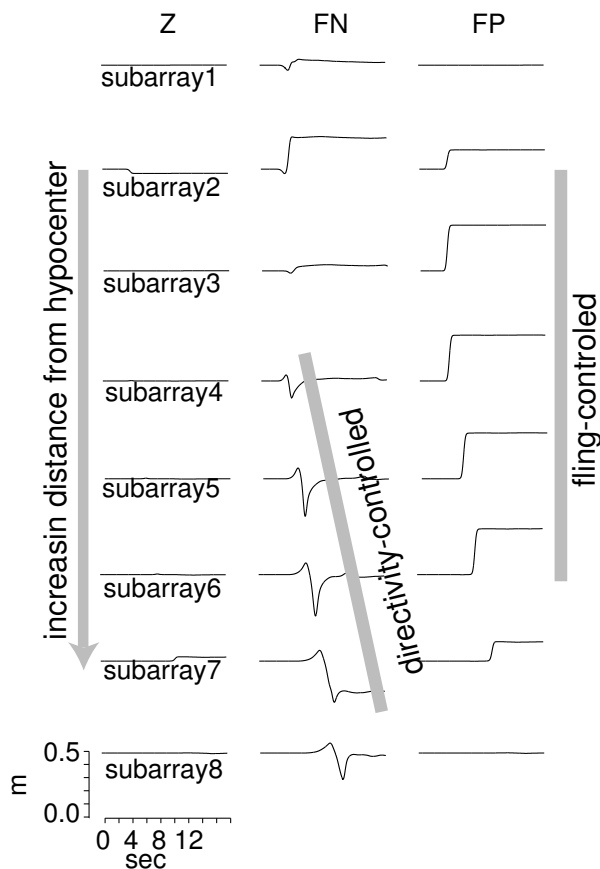


Figure 13.17: Comparison of three-component displacement records at subarrays 1-8 for the vertical strike-slip fault case. Rupture directivity is evident on the FN components. Constant amplitude static offsets are observed on the FP component for stations located along the fault.

The time from zero displacement to the final static value is controlled by the local slip rise time during rupture. In these simulations a constant average slip rise time from *Somerville et al.*, (1999) was assumed. At such close distance to the fault the corresponding velocity pulses are representative of the local slip velocity during rupture.

The FN component on the other hand only has dynamic pulse-like motions with no static offset (except for the two fault end cases already discussed). The FN component has the same amplitude on each side of the fault like the FP component, but in contrast it also has the same sign. The pulse amplitude is seen to steadily grow from subarray 3 to 6 due to directivity. At subarray 7 the FN amplitude is slightly reduced, and it remains large at

subarray 8 off of the end of the fault.

Because the fault is vertically dipping and the slip direction is horizontal the vertical motions are very weak in comparison to the two horizontal components. In the other simulations for different source and slip-direction geometries dynamic pulses and static offsets are observed on the vertical component.

In velocity the FN component becomes very pronounced, growing steadily in amplitude in the direction of rupture with maximum values on the order of 1 m/s. The velocity pulses have the same sign on each side of the fault. In contrast the FP (fling) velocity pulses along the fault have constant amplitude, but opposite sign on the two sides of the fault. The FP velocity pulses also have amplitude on the order of 1 m/s. The FP peak velocity close to the fault is controlled by the slip velocity on the fault. Slip velocity is proportional to stress drop and therefore for events with stress drop on the order 10 MPa the slip velocity is on the order of 1 m/s.

The magnitude of the directivity effect depends on how co-linear the strike and slip directions are. In the case of a vertical strike-slip fault the strike and rake are co-linear producing a maximum directivity effect. In the case of a reverse fault the rake is perpendicular to the strike and this produces a minimum directivity effect (except in the updip direction). The simulations for the other fault orientations clearly illustrate this point. Figure 13.17 also shows that the amount of directivity depends on distance from the epicenter to the station.

In general the simulations show that both static offsets and dynamic directivity-controlled pulses need to be considered on any of the three components to account for possible faulting variability. In fact, as the faulting style trends to dip-slip cases there is increased vertical motions and a transition of fling-controlled motions (static offsets) to the FN component, and directivity-controlled motions to the FP component. In oblique faulting cases it will be necessary to consider both dynamic pulses and static offsets in displacement on all three components.

8.4 References

- Larsen, S. and C.A. Schultz (1995). ELAS3D: 2D/3D elastic finite-difference wave propagation code, *Technical Report No. UCRL-MA-121792*, 19 pp.
- Somerville, P. G., K. Irikura, R. Graves, S. Sawada, D. Wald, N. Abrahamson, Y. Iwasaki, T. Kagawa, N. Smith, and A. Kowada (1999). Characterizing crustal earthquake slip models for the prediction of strong ground motion, *Seism. Res. Lett.*, 70, 59-80.

9. Investigation of Deep Earthquake Mechanics

Ahyi Kim and Douglas Dreger

9.1 Introduction

The mechanism of deep earthquakes in subducted oceanic lithosphere in the transition zone remains enigmatic, although there have been several studies about the mechanism for these events (e.g. *Seilver et al.*, 1995; *Raleigh and Patterson*, 1965; *Ogawa*, 1987; *Hobbs and Ord*, 1988). It is known that first motions from deep earthquakes show four-lobed radiation patterns typical of shallow shear dislocation (*Honda*, 1932). At such depth, because of tremendous pressure, frictional sliding similar to that for shallow events is not possible, yet they must have a separate mechanism that produces earthquake motions much like their shallow counterparts. Interpretation of constitutive relations for the deep-focus events is the one of the approaches to finding the mechanism for these events. For the great Bolivia earthquake, which occurred on June 9, 1994 with a moment magnitude of 8.2, *Kanamori et al.* (1998) argued that the source process was dissipative based on calculation of seismic efficiency from the observed low rupture velocity. In their paper they show that once rupture initiated, melting could occur, further reducing friction and promoting fault slip. In this study, using several large deep-focus earthquakes, we compute the dynamic and static stress change inferred from kinematic source models of deep-focus earthquakes to see if they have a more dissipative process on average than those of the shallow events, and to also see the range of variability of these parameters among the set of deep earthquakes that have reasonable set of models.

9.2 Data and Method

As a first step, we examined 2 deep-focus earthquakes, namely by the Bolivia (June 9, 1994 Mw8.2 623km) and Fiji earthquakes (March 9 1994 Mw7.6 563km). Kinematic models and other source parameters were determined by *Antolik* (1996). To examine the slip weakening constitutive relationship for deep-focus earthquakes, at first, we calculated, or collected from the literature information, about the seismic moment, the radiated seismic energy, faulting area, average slip, and static stress drop. Second, following the method of *Kanamori et al.* (1998), the possible temperature rises for all of the events were estimated using the parameters collected. To compute the temperature rise, it was necessary to assume the width of the shear zone, which was inferred from the rise time (e.g. *Kanamori et al.*, 1998), or the scaling of anti-crack width to shear-slip from laboratory measurements (e.g. *Bouchon and Ihmle*, 1999). The radiated energy, scalar seismic moment and stress drop were used to determine

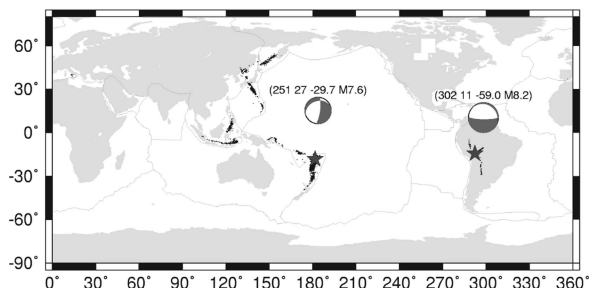


Figure 13.18: the location and moment tensor solution for the earthquakes. Bolivia earthquake occurred in the subducting Nazca plate. In this region, the deep earthquakes doesn't occur often, but they have very big magnitude when they occur. From the study of *Kanamori et al* (1998), Bolivia earthquake had the very high stress drop and Long risetime, and low seismic efficiency. On the other hand, For Fiji earthquake, which was occurred in the subducting Pacific plate. Most of the deep earthquakes occur in this region.

the seismic efficiency, which we correlated to independent observations of the rupture velocity in these events. From this analysis the events can be categorized in terms of the degree of their dissipative character. Third, to determine the temporal displacement and stress fields, we used the finite-difference method with a kinematic representation of the source process as a boundary condition (e.g. *Ide and Takeo*, 1997). We used kinematic models which have been well determined (*Antolik*, 1996). The finite-difference method is used to solve the equation of motion with an isotropic, linear-elastic stress constitutive relationship to determine the velocity/stress wavefield due to the prescribed finite-source slip. We used the absorbing boundary condition on all surfaces because all of the events are at great depth. The stress drop models obtained from this study were used to estimate the frictional energy and the possible temperature rise during faulting to assess whether frictional melting could have played a role in the other large deep earthquakes. For this analysis, we followed the method introduced in *Bouchon and Ihmle* (1999). The determined velocity/stress fields at the third step were used to examine the stress-slip constitutive relationship, the static stress drop, and the normal stress perturbation for each of the events. The magnitude of the dynamic shear and normal stress over the fault in advance of the rupture provides information on the level of deviatoric stress that triggers mecha-

nisms by which ruptures continue to grow; in the case of the Bolivia earthquake possibly outside the region of the metastable slab core.

9.3 Results

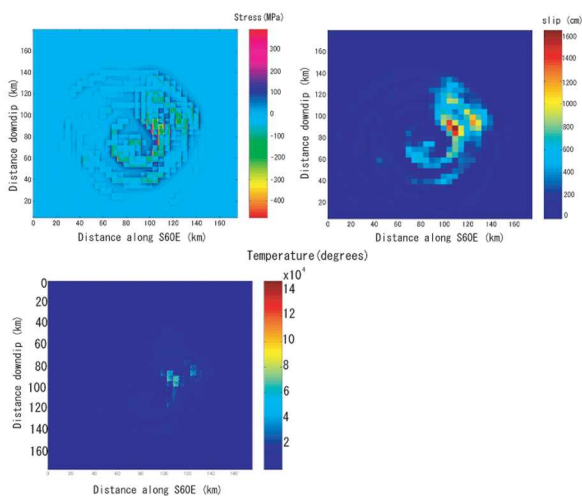


Figure 13.19: result for the Bolivia earthquake(Top right)slip distribution, (Top left)static stress distribution (bottom)possible temperature rise during the rupture.

Figure 2 shows the slip distribution, static stress change and possible temperature rise during the Bolivia earthquake. For the Bolivia earthquake, the source time function shows a large moment release 15 sec after initiation and as a result, the largest offset is not in the hypocenter region. The maximum stress change was 400Mpa, and the average stress was 21Mpa at the main rupture area, which is consistent with the result of static stress drop estimates (*Bouchon and Ihmle*, 1999). Using the stress distribution, we compute the possible temperature rise at each subfault. Taking into account the rock melting temperature of around 600 degrees, we found during the Bolivia earthquake, that melting likely occurred. The Fiji earthquake showed a factor of ten lower in temperature, but still was high enough to melt the surrounding rocks.

9.4 Conclusion

We examined the stress field and calculated the temperature increase for the Bolivia and Fiji earthquakes. For the thickness of the fault zone, assumed in both cases the temperature rise was high enough to melt the surrounding rocks. In our ongoing work, we are studying kinematic modeling, and the stress change of other large deep earthquakes.

9.5 References

Antolik, M.,D. Dreger, and B. Romanowicz, Rupture processes of large deep-focus earthquakes from inversion of moment rate functions, *Journ. Geophys. Res.*, *104*, 863-894, 1999.

Antolik, M., New results from studies of three outstanding problems in local, regional global seismology, Ph.D. Thesis, 311 pp., Univ. of Calif., Berkeley,1996.

Antolik, M., D. Dreger, and B. Romanowicz, Finite fault source study of the great 1994 deep Bolivia earthquake, *Geophys. Res. Lett.*, *23*, 1,589-1,592,1996.

Bouchon, M., and P. Ihmle, Stress drop and frictional heating during the 1994 deep Bolivia earthquake, *Geophys. Res. Lett.*, *26*, 3,521-3,524, 1999.

Green, H. W., and P. C. Burnley, A new self-organizing mechanism for deep-focus earthquakes, *Nature*, *341*, 733-737, 1989.

Hobbs, B. E., and A. Ord, Plastic instabilities: Implications for the origin of intermediate and deep focus earthquakes, *Journ. Geophys. Res.*, *93*, 10,521-10,540, 1988.

Honda, H., On the types of the seismograms and the mechanism of deep earthquake, 1932.

Ide, S., and M. Takeo, Determination of constitutive relations of fault slip based on seismic wave analysis, *Journ. Geophys. Res.*, *102*, 27,379-27,391, 1997.

Kanamori, H., D. L. Anderson, and T.H.Heaton, Frictional melting during the rupture of the 1994 Bolivian earthquake, *Science*, *279*, 839-842,1998.

McGuire, J. J., D. Wiens, P. Shore, and M. Bevis, The March 9, 1994 (Mw7.6) deep Tonga earthquake: Rupture outside the seismically active slab, *Journ. Geophys. Res.*, *102*, 15,163-15,182, 1997.

Ogawa, M., Shear instability in a viscoelastic material as the cause of deep-focus earthquakes, *Journ. Geophys. Res.*, *92*, 13,801-13,810, 1987.

Raleigh, C. B., and M. S. Patterson, Experimental deformation of serpentinite and tectonic implications, *Journ. Geophys. Res.*, *70*, 3,965-3,985,1965.

Silver, P. G., S. Beck, T. Wallace, and C. Meade, Rupture characteristics of the deep Bolivian earthquake of 9 June 1994 and the mechanism of deep-focus earthquake, *Science*, *268*, 69-73,1995.

10. ElarmS: A Methodology for Earthquake Early Warning

Richard M Allen

10.1 Introduction

The ElarmS methodology is designed to predict the distribution of peak ground shaking across the region affected by an earthquake before the beginning of significant ground motion at the epicenter. The method uses the first few seconds of the P-wave at the stations closest to the epicenter to estimate the magnitude of the earthquake. Attenuation relations provide the predicted distribution of ground shaking as a function of distance from the epicenter (Allen, 2004). The complete ElarmS system generates an "AlertMap" of predicted peak ground shaking. The first AlertMap is available 1 sec after the first P-wave trigger and is updated every second as additional data is gathered from stations further from the epicenter. More information about ElarmS is available at <http://www.ElarmS.org>.

10.2 Location and warning time

ElarmS uses the arrival times of P-waves to locate earthquakes. When the first station triggers, an event is located at that station with a depth typical of events in the region. The earthquake is then located between the first two, and then the first three stations to trigger. Once four stations have triggered a grid search method is used to locate the event, minimizing the misfit between predicted and observed arrival times. The warning time is defined as the remaining time until the onset of peak ground shaking and can be estimated given the origin time and location of the earthquake using S-wave arrival time curves. Offline testing of ElarmS using a dataset of 32 earthquakes in southern California shows that the first predictions of ground shaking are available before the S-arrival at the epicenter for 56% of earthquakes (Figure 13.20).

Warning time probability density functions have been calculated for northern California. These are based on the current distribution of broadband velocity and accelerometer stations across the region and the 35 earthquake rupture scenarios identified by the *Working Group on California Earthquake Probabilities* (2003). Figure 13.21 shows the probability that there will be an earthquake in the next 30 years for which there would be a given warning time for the city of San Francisco. These calculations show that it would be possible to provide warning for the vast majority of these damaging earthquakes. It also shows that for the most damaging events that cause ground shaking with $\text{MMI} > X$ in the city, it is more likely than not that there will be more than 20 sec warning.

10.3 Rapid magnitude estimation

The magnitude of an earthquake is rapidly estimated from the frequency content of the first four seconds of the P-wave arrival. The predominant period, τ_p , of the vertical component waveform is calculated using the method first described by Nakamura [1988]. The maximum τ_p observed within 4 sec, τ_p^{max} , has been measured for earthquakes $3.0 < M < 8.3$ from around the world and is found to scale with earthquake magnitude (Figure 13.22). The data shows no evidence to suggest that the scaling relation breaks down for the largest magnitude events with rupture durations greater than 4 sec.

The accuracy and timeliness of magnitude estimates are central to the usefulness of an early warning system. The accuracy of magnitude estimates are a function of the number of stations providing P-wave data. Datasets from both southern California and Japan show that using just the closest station to the epicenter the average magnitude error is ~ 0.75 magnitude units, once data from the closest 2 stations is available the error drops to ~ 0.6 , and to ~ 0.5 magnitude units once 4 stations provide data. The offline tests of 32 earthquakes from southern California show that magnitude estimates are available for 56% of earthquakes at the time of the S-arrival at the epicenter with an average magnitude error of 0.44 magnitude units (Figure 13.20a).

10.4 Distribution of ground shaking

Given the location and magnitude of an earthquake, the spatial distribution of peak ground shaking can be estimated using attenuation relations (e.g. Campbell, 1981; Joyner and Boore, 1981; Fukushima and Irikura, 1982; Abrahamson and Silva, 1997; Boore, et al., 1997; Campbell, 1997; Sadigh, et al., 1997; Field, 2000). Attenuation relations for small and large magnitude events have already been developed for southern California (Allen, 2004), and are under development for northern California.

ElarmS uses the attenuation relations in a two-stage process. One second after the first P-wave trigger the first estimate of magnitude is available and the attenuation relations provide PGA as a function of distance from the epicenter. The error in the PGA estimates as a function of time for the 32 earthquakes in the test dataset from southern California is shown in Figure 13.20b. As time progresses, the stations closest to the epicenter experience their PGA and this information is used to adjust the initial attenuation relation. The improvement in the PGA estimate is only marginal as shown in Figure

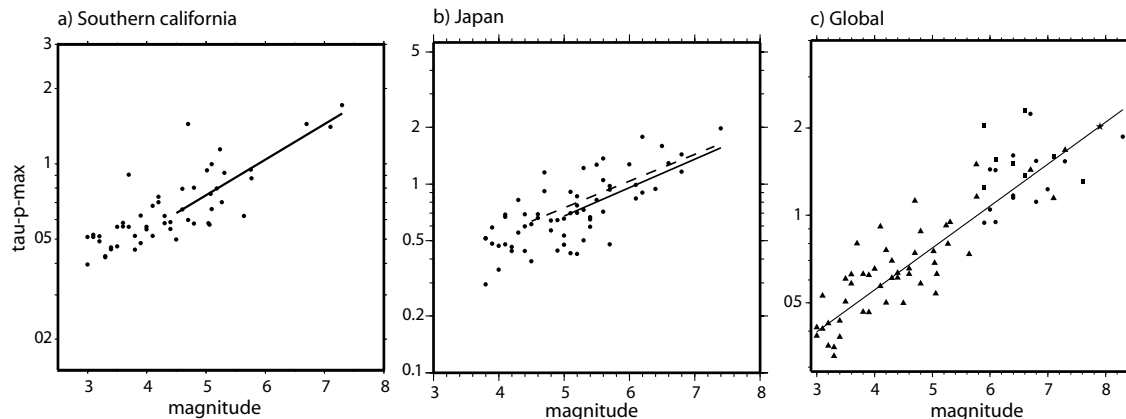


Figure 13.22: Scaling relation between event-averaged τ_p^{max} and magnitude. All data has been processed using the same recursive algorithms. A) Southern California earthquakes and best fit relation (solid line). From *Allen and Kanamori* (2003). B) Earthquakes in Japan and best fit relation (solid line). The dashed line is the best fit relation for California shown in A which is nearly identical. From *Lockman and Allen* (in review). C) Global compilation of earthquakes including southern California, Japan, Taiwan and the Denali earthquake. Waveforms are a mixture of accelerometers and broadband velocity instruments.

13.20c, but inclusion of PGA observations once available does remove outliers i.e. cases when the magnitude based estimate is very high or low.

10.5 Acknowledgements

This work was funded by the US Geological Survey NEHRP program, awards 03HQGR0043 and 05HQGR0074.

10.6 References

Abrahamson, N. A., and W. J. Silva, Empirical response spectral attenuation relations for shallow crustal earthquakes, *Seismo. Res. Lett.*, *68*, 94-127, 1997.

Allen, R. M., Rapid magnitude determination for earthquake early warning, in *The many facets of seismic risk*, edited by M. Pecce, et al., pp. 15-24, Universita degli Studi di Napoli "Federico II", Napoli, 2004.

Allen, R. M., and H. Kanamori, The potential for earthquake early warning in southern California, *Science*, *300*, 786-789, 2003.

Boore, D. M., W. B. Joyner, and T. E. Fumal, Equations for estimating horizontal response spectra and peak acceleration from western north american earthquakes; a summary of recent work, *Seismo. Res. Lett.*, *68*, 128-153, 1997.

Campbell, K. W., Near-source attenuation of peak horizontal acceleration, *Bull. Seism. Soc. Am.*, *71*, 2039-2070, 1981.

Campbell, K. W., Empirical near-source attenuation relationships for horizontal and vertical components of peak ground acceleration, peak ground velocity, and

pseudo-absolute acceleration response spectra, *Seismo. Res. Lett.*, *68*, 154-179, 1997.

Field, E. H., A modified ground-motion attenuation relationship for southern California that accounts for detailed site classification and a basin-depth effect, *Bull. Seismol. Soc. Am.*, *90*, S209-S221, 2000.

Fukushima, Y., and K. Irikura, Attenuation characteristics of peak ground motions in the 1995 hyogo-ken, *J. Phys. Earth*, *45*, 135-146, 1982.

Joyner, W. B., and D. M. Boore, Peak horizontal acceleration and velocity from strong-motion records including records from the 1979 imperial valley, California, earthquake, *Bull. Seismol. Soc. Am.*, *71*, 2011-2038, 1981.

Lockman, A., and R. M. Allen, Magnitude-period scaling relations for Japan and the Pacific Northwest: Implications for earthquake early warning, *Bull. Seismol. Soc. Am.* in review.

Nakamura, Y., On the urgent earthquake detection and alarm system (UrEDAS), *Proc. 9th World Conf. Earthquake Eng.*, *VII*, 673-678, 1988.

Sadigh, K., C. Y. Chang, J. A. Egan, F. Makdisi, and R. R. Youngs, Attenuation relationships for shallow crustal earthquakes based on California strong motion data, *Seismo. Res. Lett.*, *68*, 180-189, 1997.

Working Group on California Earthquake Probabilities, *Earthquake probabilities in the San Francisco Bay region: 2003 to 2031*, U.S. Geological Survey, 2003.

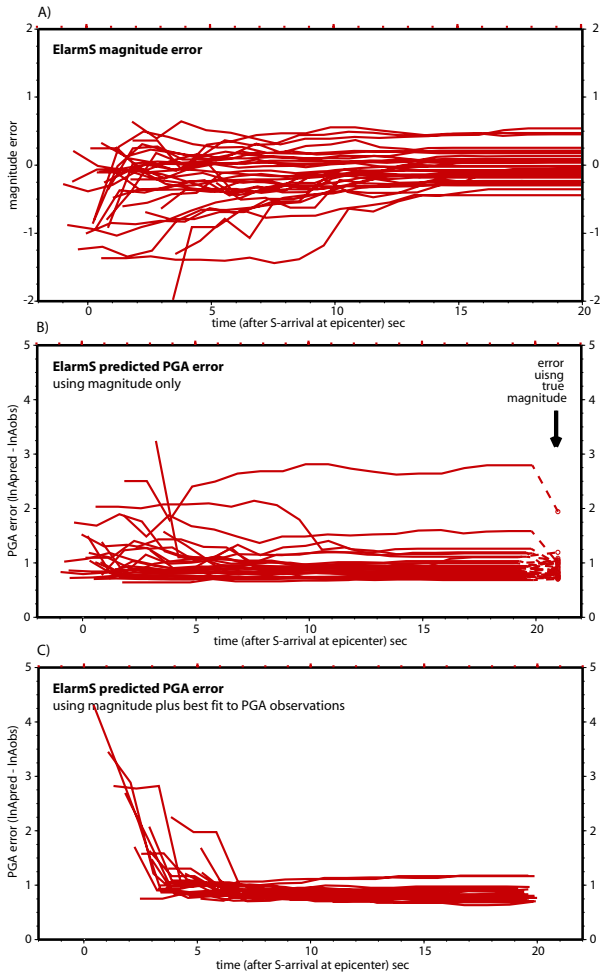


Figure 13.20: The results of testing ElarmS offline using a set of 32 earthquakes in southern California and the current distribution of stations. All panels show errors as a function of time with respect to the S-wave arrival at the epicenter which represents the earliest time of peak ground shaking during an earthquake. A) The error in the magnitude estimate. A magnitude estimate is available for 56% of earthquakes at the time of the S-arrival at the epicenter with an average magnitude error of 0.44 magnitude units. Within 5 sec magnitude estimates are available for 97% of events with an average error of 0.33. B) Average absolute error in PGA estimates at all stations. At the time of the S-arrival the average absolute error is 1.08. It drops to 1.00 within 5 sec, 0.98 within 10 sec, and reaches 0.95 at 15 sec. When the correct magnitude is used in the attenuation relations (i.e. removing the error in the ElarmS magnitude estimate), the error is 0.89, only slightly lower. C) Average error in PGA once available PGA observations are incorporated. The most important use of PGA observations is to remove outliers. The error in the PGA estimates is calculated in the usual way: the error is the natural logarithm of the predicted PGA minus the natural logarithm of the observed PGA for the event.

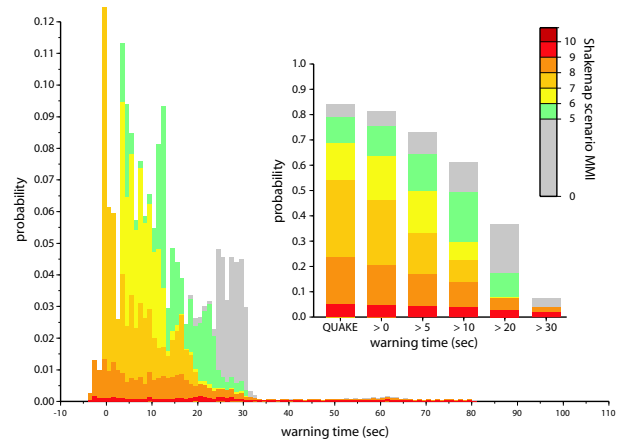


Figure 13.21: Earthquake early warning time probability density function for the city of San Francisco. Warning times were calculated for the 35 rupture scenarios identified by the *Working Group on California Earthquake Probabilities* (2003) and the probability of each rupture assigned to the warning time. Epicenters were distributed at 1 km intervals along the complete length of each rupture and the cumulative probability of all events set equal to the probability of the rupture scenario. The warning time is defined at the time at which 4 sec of the P-wave is available at 2 stations and a 2 sec delay for telemetry has been added. This distribution of warning times is based on the current distribution of stations with a moderate improvement to telemetry. The warning times are color coded by the predicted intensity of ground shaking in the city using the scenario ShakeMaps. The inset shows the probability of > 0, 5, 10, 20 and 30 sec warning along with the total probability of all 35 rupture scenarios (labeled QUAKE).

11. Northern California Seismicity Project

Robert A. Uhrhammer

11.1 Introduction

The Northern California Seismicity Project (NCSP) is a counterpart to the San Francisco Bay Region (SFBR) - Historical Earthquake Re-analysis Project (HERP) which has been reported upon in previous annual reports. The initial objective of this project which commenced in August, 2000, is to transcribe the pre-1984 data for $M_L \geq 2.8$ earthquakes which have occurred in Northern and Central California (NCC) (outside of the SFBR covered by HERP), from the original reading/analysis sheets, kept on store in the Berkeley Seismological Archives, to a computer readable format.

Characterization of the spatial and temporal evolution of NCSP seismicity during the initial part of the earthquake cycle as the region emerges from the stress shadow of the great 1906 San Francisco earthquake is the long term goal. The problem is that the existing BSL seismicity catalog for the SFBR, which spans most of the past century (1910-present), is inherently inhomogeneous because the location and magnitude determination methodologies have changed, as seismic instrumentation and computational capabilities have improved over time. As a result, NCC seismicity since 1906 is poorly understood.

Creation of a NCC seismicity catalog that is homogeneous, that spans as many years as possible, and that includes formal estimates of the parameters and their uncertainty is a fundamental prerequisite for probabilistic studies of the NCC seismicity. The existence of the invaluable BSL seismological archive, containing the original seismograms as well as the original reading/analysis sheets, coupled with the recently acquired BSL capability to scan and digitize historical seismograms at high resolution allows the application of modern analytical algorithms towards the problem of determining the source parameters of the historical SFBR earthquakes.

11.2 Background and Motivation

Although the 1910 to present BSL catalog of earthquakes for NCC appears to be a simple list of events, one must remember that it really is a very complex data set. It is easy to misinterpret observed variations in seismicity if we do not understand the limitations of this catalog. The existing 1910 to present BSL catalog of earthquakes for NCC is inhomogeneous in that it suffers from the three types of man-made seismicity changes identified by *Habermann, 1987*, namely detection changes, reporting changes, and magnitude shifts. The largest change in the detection capability of the BSL seismic station net-

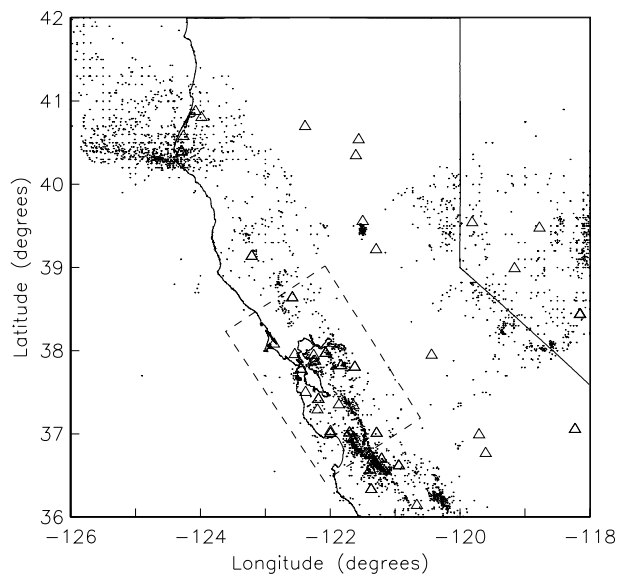


Figure 13.23: Map of the NCC Region showing the 1951-1983 $M_L \geq 2.9$ seismicity (small dots). The triangles are the seismic stations, operated by Berkeley and adjacent networks between 1951 and 1983, for which data are available. Events occurring in the dashed inset box were transcribed and analyzed as a part of the HERP project.

work occurred starting circa 1927 with the installation of the Wood-Anderson and Benioff seismometers at several sites in NCC (see Figure 13.23) and the resulting increase in sensitivity lowered the threshold for detection of NCC earthquakes by about 2 M_L units. The most significant reporting change occurred circa 1942 when the BSL began determining M_L for some earthquakes and by 1948 M_L was routinely determined and reported for all SFBR earthquakes listed in the BSL Bulletin (*Romney and Meeker, 1949*).

The lack of a homogeneous catalog of earthquake for the SFBR which spans most of the past century, the availability of the invaluable BSL seismological archive, the interest in the Working Group on California Earthquake Probabilities (WGCEP, 1999), the funding of an initial effort with support from the USGS-PG&E CRADA, and the purchase and loan of a high-resolution wide-format digitizer by the USGS, combine to provide both an incentive and an unique opportunity to systematically re-process, using modern algorithms, the BSL seismographic records and data for SFBR earthquakes and to produce a homogeneous catalog of earthquakes for the

region.

11.3 Current Effort

To expedite the transcription process, we converted all relevant available data from the online NCEDC event catalogs and the in-house phase data to a flat transcription file format for the years 1978 through 1983. We also acquired a copy of the International Data Center (ISC) CDROM which contains events and associated station data published in the ISC Bulletins from January 1964 through December 1977 (Version 1.2). This ISC data set includes event and station data contributed by Berkeley and the CDROM also contains a algorithm to search the database and extract and translate the ISC coded phase Berkeley data to a readable print format for years 1963 through 1977. This enabled us to start with transcription files that contained approximately half of the data that is on the original reading/analysis sheets for the years 1964 through 1983. The primary data from the original reading/analysis sheets, that was not included in this process, was the Wood-Anderson maximum trace amplitude data that is crucial for the determination of local magnitude.

During the past year six students worked on the process of transcribing the data from the original BSL reading/analysis sheets to computer readable form. They started by checking the transcription of the original reading/analysis sheets and locating the earthquakes from 1983 and they have been working back in time. Since none of the data on the pre-1964 reading/analysis sheets exists in a computer readable form, all data has to be transcribed and consequently it takes more time to transcribe each event. Currently they are currently transcribing reading/analysis sheet data from 1951 and they have processed reading/analysis sheets for over 4400 earthquakes which have occurred in NCC. Also, the pre-1951 reading/analysis sheets data do not contain Wood-Anderson maximum trace amplitude data which is used in the calculation of local magnitude so that the original Wood-Anderson seismograms with have to be retrieved from the archive and the amplitudes read. This quite labor intensive component of the project is planned for the coming year.

11.4 Acknowledgements

UC Berkeley students Vicky Chi Sum Chan, Jonathan Hsu, Rose Li, Sean Tsai, Noli Valera and visiting U Pennsylvania student Carmen Rodriguez participated in this project during the past year and we thank them for their efforts.

This project was partially supported by the USGS funding of the Northern California Earthquake Data Center.

11.5 References

Habermann, R. E., Man-made changes of seismicity rates, *Bull. Seism. Soc. Am.*, 77, 141-159, 1987.

Romney, C. F. and J. E. Meeker, Bulletin of the Seismographic Stations, *University of California Press*, 18, pp. 89, 1949.

12. Seismogram Scanning Project

Robert A. Uhrhammer

12.1 Introduction

This aim of Seismogram Scanning Project (SSP) is to scan selected analog seismograms kept on store in the Berkeley Seismological Laboratory (BSL) Seismogram Archive and generate digital image files for studying microseismic source areas and distribution in relation to wave climate. The Berkeley Seismogram Archive, where approximately 1.2 million analog seismograms dating back to 1910 are stored, contains seismograms recorded at the Berkeley seismic station, dating back to 1930, which are crucial for this project. This scanning project is being undertaken in collaboration with Dr. Peter Bromirski of the University of California, San Diego/Scripps Institution of Oceanography on his project funded by the California Department of Boating and Waterways. The corresponding digitization of the scanned seismograms is being done at the Scripps Institution of Oceanography.

12.2 Background and Motivation

The photographic and smoked paper seismograms kept on store in the BSL seismogram archive are gradually deteriorating over time and scanning of the seismograms into a computer readable format is essential if they are to be preserved for the future. BSL has a wide format scanner and whenever the opportunity and funding allows we make an effort to scan seismograms.

12.3 Current Effort

During the past year we have systematically scanned the November-March Berkeley vertical component Sprengnether seismograms for the winters of 1962 through 1991 and also the November-March Berkeley vertical component Wilip-Galitzin seismograms for the winters of 1930 through 1964 for a total of $\sim 10,000$ seismograms.

12.4 Digitization Procedure

Digitization of the photographic seismograms has two components. The seismograms are first scanned at a resolution of 400 dots per inch on an Contex Scanning Technology Ideal FSS 18000 DSP Full Scale Scanner using their interactive WIDEimage scanning software package (URL: <http://www.contex.com/software/wideimagenet/default.htm>). The scanned images are stored as Tag Image Format (TIF) bitmap image files. To substantially reduce the storage requirements a histogram analysis is employed to interactively set an appropriate thresh-

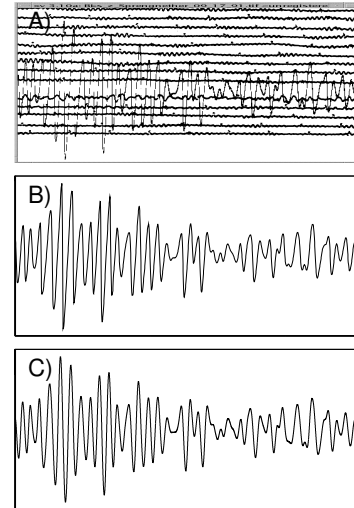


Figure 13.24: A comparison of: A) the scanned BKS Sprengnether Z-component seismogram; B) the corresponding digitized waveform, and; C) the corresponding waveform synthesized from the co-sited Streckeisen STS-1 broad band seismograph. The seismic signal is from a M 5.7 teleseism which occurred 4000 km SE of Berkeley (1991/09/18,09:48:13; 14.65N, 90.99W) in Guatemala. All three plots are at the same scale with the horizontal axis spanning 511.25 seconds and the vertical axis spanning 175 mm. That all three waveforms are highly similar is verification of the accuracy of the digitization procedure and the accuracy of the Sprengnether transfer function.

old and the scanned seismograms are stored as 1-bit resolution line-art images. The traces on the scanned seismogram image are then digitized at nominally 4 samples per second using the SeisDig software package (Bromirski and Chuang, 2003) available for download at URL: <http://www.ucsg.edu/~bromirski>. The resulting digitized seismogram has an amplitude resolution of 0.0635 mm (i.e. the pixel resolution and equivalent to a data logger sensitivity of 15748 DU/M) and a time resolution of 0.254 seconds for the SPR seismograms recorded at 15 mm/min and 0.127 seconds for the W-G seismograms recorded at 30 mm/min (also the pixel resolution). The effective dynamic range is approximately 64 dB ($20 \log_{10}(100\text{mm}/0.0635\text{mm})$). An example of a digitized SPR seismogram is shown in Figure 13.24.

12.5 Calibration of Wilip-Galitzin, Sprengnether and Streckeisen Seismographs

As seismic instrumentation has evolved, three different three-component set of long-period/broadband seismographs have been installed and operated, with overlapping intervals, at Berkeley since the 1930's. Wilip-Galitzin (W-G) seismographs were operated on the northern most seismic piers in the basement of Haviland Hall on the Berkeley Campus (BRK) from August 28, 1930 until February 1, 1965. World Wide Standardized Station (WWSS) Sprengnether (SPR) long-period seismographs were operated in the Byerly Seismic Vault (BKS), located in Strawberry Canyon behind the Botanical Garden, from June 8, 1962 until September 30, 1991. Streckeisen (STS-1) broadband seismographs began recording in the Byerly Seismic Vault (BKS) on May 11, 1987 with a 16-bit PC-based recording system (*Bolt et al.*, 1988) and a 20 second pendulum configuration and by August 8, 1991 they had evolved into the current 24-bit Quanterra Q680 data logger and 360 second very-broadband (VBB) pendulum configuration. The W-G and SPR seismographs operated concurrently, but not co-sited, from June 8, 1962 until February 1, 1965. The SPR and STS-1 seismographs operated concurrently at BKS from August 8 until September 30, 1991. Comparison of selected seismograms from these intervals allow us to verify the calibration and response of these seismographs and to demonstrate that, within appropriate passbands, the earlier instrument seismograms can be reliably synthesized from later instrument seismograms and that absolute ground motions can be reliably estimated. An example of a SPR seismogram, synthesized from the corresponding STS-1 seismogram, is shown in Figure 13.24. A Streckeisen STS-2 seismograph has operated at BRK since January 1, 1993 and a comparison of selected seismograms from the BKS STS-1 and the BRK STS-2 is used to quantify differences in their site responses. A comparison of the responses of these seismographs is shown in Figure 13.25.

12.6 Acknowledgements

UC Berkeley students Amanda Austin and Kevin Lee participated in this project during the past year and we thank them for their efforts.

This project was funded by sub-award of the California Department of Boating and Waterways Contract 03-106-105.

12.7 References

Bolt, B. A., J. E. Friday and R. A. Uhrhammer, A PC-based Broadband Digital Seismograph Network, *Geophysical Journal*, 93, 565-573, 1998.

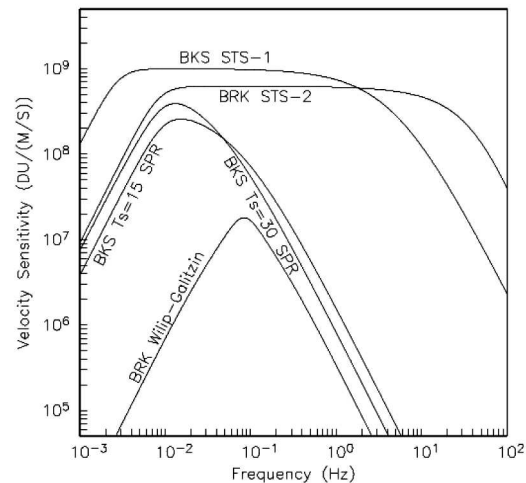


Figure 13.25: A comparison of the velocity responses of the BRK W-G and STS-2 and the BKS SPR and STS-1 seismographs operated at Berkeley. The W-G and SPR instruments recorded galvanometrically on photographic paper and the paper seismograms are scanned at a resolution of 400 dots per inch. The STS-1 and STS-2 instruments record digitally via a high-resolution data logger. The velocity sensitivity is given in digital units per meter per second (DU/(M/S)). Two responses are given for the SPR because its natural period (T_s) was changed from 30 seconds to 15 seconds on May 12, 1965.

Bromirski, P. D. and S. Chuang, SeisDig Software to Digitize Scanned Analog Seismogram Images: User's Manual, *Scripps Institution of Oceanography Technical Report, Scripps Institution of Oceanography, Integrative Oceanography Division*, UC San Diego, 28 pp., July 2, 2003.

13. Insight into the Origin of Earth's hum and Microseisms

Junkee Rhie and Barbara Romanowicz

13.1 Introduction

It is well understood that the background level of seismic noise is affected by fluid covers surrounding the solid Earth, such as the atmosphere and ocean. Microseism due to ocean waves is the most significant seismic noise at periods between 2 to 25 sec. For very long periods (> 1000 s), variations in atmospheric pressure affect more significantly the level of seismic noise with increasing period. Between the two period ranges, from 150 to 500 s, weak but dominant background noise is the continuous free oscillations of the Earth. [e.g. *Nawa, et al.*, 1998; *Suda et al.*, 1998]. The amplitude level of this excitation is very low and it can be only detected by stations with a quiet seismic environment or by stacking of several seismic records. Rhie and Romanowicz [2004] showed that the geographic locations of the sources generating ubiquitously propagating Rayleigh waves are mostly in the oceans and that infragravity waves may play an important role in the transfer of energy from the atmosphere to the solid Earth. The theoretical work explaining the oceanic origin of the continuous free oscillations followed, and demonstrated that infragravity waves have enough energy to generate continuous free oscillations. [*Tanimoto*, 2005]. Significant wave height measurements at buoys on the Pacific show significant correlations with the variations of seismic amplitude in the microseism band (2-25 s). An interesting observation is that the ocean measurements show a good correlation with the variation in the seismic amplitude in the hum band (150-500 s) as well. This observation may indicate that seismic excitations in both frequency bands, 2-25 s and 150-500 s, have the same source or similar generating mechanism, i.e. ocean waves propagating to the shore. However, long period energy propagates long distance more efficiently and is able to excite observable continuous free oscillations of the Earth.

13.2 Correlation between two arrays

Rhie and Romanowicz (2004) showed that there is a very good correlation between the variations in maximum stack amplitudes for two regional arrays at Japan (F-net) and California (BDSN) with common maximum amplitude on day 31 in 2000 at periods around 240 s. This correlation was explained by common sources generating long period surface wave energy over the ocean. Both seismic arrays detect maximum seismic energy arriving on day 31 and significant wave height measurements near the California and Japan coasts also show that wave heights were largest around day 31 in 2000.

We took time windows from 30 to 35 days in 2000 to compare the variations in seismic amplitudes for the two arrays. Stack amplitude functions as a function of time and back-azimuth are computed for both arrays and moving averages with the duration of 6 hours and shift of 1 hour are taken. Stack amplitude functions are computed by correcting for dispersion based on PREM. Gaussian filters with center period of 150 s and 240 s had been taken before the dispersion correction and stacking. The overall trends for both arrays and both frequency bands are consistent, but if we look more carefully, some differences emerge. For example, it is clear that onsets of first maxima on day 31 for F-net and BDSN have a time difference of about 0.5 days, which is too large to be explained by seismic wave propagation from one common source under the assumption of minor arc propagation. This indicates that both arrays detect elastic energy arrivals coupled at different geographic regions.

13.3 Correlation between ocean and seismic data

We collected significant wave height recordings measured at buoys deployed by National Ocean and Atmospheric Administration (NOAA) and Japan Meteorological Agency (JMA) on the Pacific for days of 30 through 35 in 2000. The significant wave heights are compared to the variations in the level of seismic amplitude at F-net and BDSN (Figure 13.26).

We computed maximum mean stack amplitude for center period of 240 s and compared the variations in amplitude with significant wave height measured at buoys placed close to the two arrays in Japan (F-net) and California (BDSN). Two significant wave height measurements in different parts of the Pacific show similar trends with two maxima on day 31 and 33. Rough comparison of the onsets of associated maxima in buoy and seismic data for the eastern Pacific shows that the maximum in the seismic data arrives later than that in buoy data on days 31 and 33. It indicates that seismic energy measured at the two arrays had been generated closer to the shore than the location of the buoys and the mechanism of generating continuous long period Rayleigh waves may be similar to the one for the microseisms at short periods. The significant wave heights measured at the buoys placed very close to the Californian coast (46027 in Figure 13.26) show much better agreement with the seismic data at BDSN. It is very difficult to determine similar trends of significant wave heights at eastern and western part of the Pacific are just local phenomena from

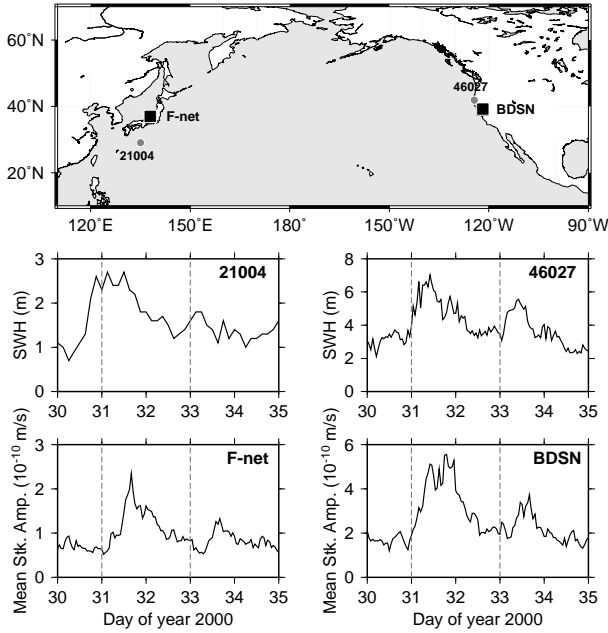


Figure 13.26: Significant wave heights at buoys (solid gray circles) near California and Japan coasts and mean stack amplitudes for two regional arrays (black squares)

separate ocean waves or basically initiated by one common origin. Considering long term correlation of seismic amplitudes for both arrays, we prefer one common atmospheric perturbation - that may be very spatially extended - which generates eastward and westward propagating ocean waves.

13.4 Cross continental propagation of surface wave energy

In the previous section, we showed there is very good correlation between ocean wave heights and seismic excitations. We believe that the energy in ocean waves is converted to elastic energy close to the coast and propagates over the array and this elastic energy can excite the continuous oscillations of the Earth. To confirm this hypothesis, we need to show the elastic energy generated from the ocean wave can propagate long distance to finally be able to excite normal modes of the Earth. We selected several high dynamic range, very broad band seismometers deployed in the United States and computed their power spectral densities at long periods between 50 to 350 s to check if there is similar trend we found in oceanic and seismic data near the coast of California (Figure 13.27). We can clearly see two large amplitude peaks in PSD on day 31 and 33 at all three stations (CMB, TUC, and HRV).

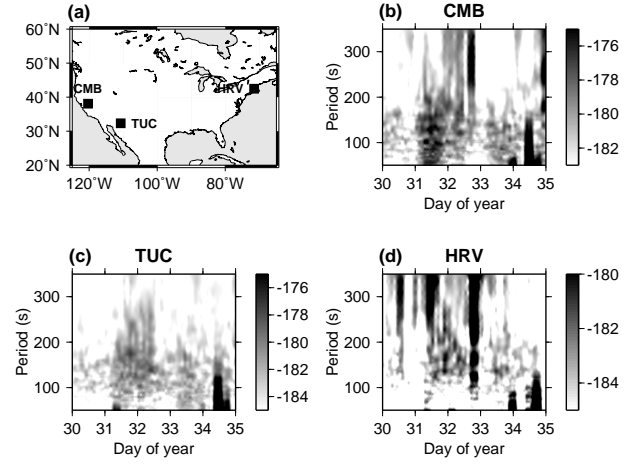


Figure 13.27: Power spectral densities at three stations. The unit for (b), (c) and (d) is $10 \times \log(m^2 s^{-4}) / Hz$.

13.5 Discussion

We showed that there is a good correlation between significant wave heights measured at buoys and the variation in seismic amplitudes at long periods. Also, this long period energy can propagate across the continent. This observation may indicate that interaction between ocean wave and sea floor near the coast generates not only short period seismic wave (microseisms) but also long period ones (the hum of the Earth).

13.6 Acknowledgements

We are thankful to Dr. Nozomu Takeuchi for making Japanese buoy data available.

13.7 References

- Nawa, K, N. Suda, Y. Fukao, T. Sato, Y. Aoyama, and K. Shibuya, Incessant excitation of the Earth's free oscillations, *Earth Planets Space*, 50, 3-8, 1998.
- Rhie, J. and B. Romanowicz, Excitation of Earth's continuous free oscillations by atmosphere-ocean-seafloor coupling, *Nature*, 431, 552-556, 2004.
- Suda, N. K. Nawa, and Y. Fukao, Earth's background free oscillations, *Science*, 279, 2089-2091, 1998.
- Tanimoto, T., The oceanic excitation hypothesis for the continuous oscillations of the Earth, *Geophys. J. Int.*, 160, 276-288, 2005.

14. Observations of Infragravity Waves at the Monterey Ocean Bottom Broadband Station (MOBB)

David Dolenc, Barbara Romanowicz, Debra Stakes (MBARI), Paul McGill (MBARI), and Doug Neuhauser

14.1 Introduction

The Monterey ocean bottom broadband station (MOBB) is a collaborative effort between the Monterey Bay Aquarium Research Institute (MBARI) and the Berkeley Seismological Laboratory (BSL). The MOBB is located 40 km offshore in the Monterey Bay, buried in the ocean floor at a water depth of 1000 m (*Romanowicz et al.*, 2003).

Infragravity waves are ocean surface waves with periods longer than the wind-driven waves and the swell. Their wave amplitudes in the deep water are small (< 1 cm) and they can be observed in the frequency band from 0.002 to 0.05 Hz. Infragravity waves have been identified as an important source of long-period noise at the ocean bottom (*Webb et al.*, 1991). Recently, they have also been proposed as a source of the Earth's continuous free oscillations (*Rhie and Romanowicz*, 2004; *Tanimoto*, 2005).

14.2 Observations

We computed power spectral density (PSD) for 1-hour long MOBB data segments and compared the results to the spectral wave density (SWD) measured at the nearby NOAA buoys. The SWD is computed at the buoys and measures energy of the ocean waves in m^2/Hz in the 0.01 Hz wide frequency bins that cover the 0.03 to 0.4 Hz range. The location of the buoys as well as comparison spectrograms for a 7-day period are shown in Figure 13.28. The infragravity peak can be observed in the PSD plot for the vertical MOBB channel (Figure 13.28, top panel). A rather sudden change of the infragravity peak width is indicated with a black line. The storm observed on day 344 was approaching from the WNW direction. Increased energy of the 10-20 s ocean waves on day 344 can therefore first be seen on buoy 46014, and last on buoy 46011. The arrival of these waves at buoy 46042 coincides with the increase of the infragravity signal on MOBB. This tells us that the infragravity waves observed at MOBB are primarily locally generated. The same can generally be observed throughout the deployment and for storms arriving from different azimuths.

14.3 Modulation of infragravity signal

The PSD for the vertical MOBB component for a 10-day period is shown in Figure 13.29b. As before, the strongest infragravity signal (days 18-20) coincides with the increased energy of 10-20 s ocean waves as recorded

at the local buoy 46042 (Figure 13.29f). In addition, two types of modulation of the infragravity peak can be observed (*Dolenc et al.*, 2005).

The modulation with a period equal to the diurnal tide and to a lesser extent the semidiurnal tide is best seen at the short-period end of the infragravity peak (30-40 s periods) as well as throughout the entire infragravity band. This modulation correlates with the amplitude of the ocean tides at MOBB, shown in Figure 13.29a.

Previous studies of the nonlinear interaction between short-period waves and currents (*Longuet-Higgins and Stewart*, 1960, 1964) found that the energy variations of the short-period waves correspond to work done by the currents against the radiation stress of the short-period waves. The magnitude of the energy exchange between the short-period waves and tidal current depends on the pattern of the tidal currents, but in simple situations, the energy of the short-period waves is in phase with the tidal elevations (*Longuet-Higgins and Stewart*, 1964). This agrees with our observations.

Another effect that the tides have on the generation of the infragravity waves is through different topography that is brought into play at the same water depth during different tide heights. The topography around MOBB is very complex and it is possible that already a small water depth change can significantly perturb the conditions for generation and reflection of infragravity waves.

We also observe a low-frequency modulation which is best seen as the variation of the period on the long-period side of the infragravity peak at which the infragravity peak rises above the noise from other sources (Figure 13.29b,c). First we compare this to the significant wave height measured at the local buoy 46042 (Figure 13.29d). The two agree well in the first half of the 10-day period, but then significant wave height has a peak in the second half of the day 25, when most of the wave energy was in the waves with periods shorter than 10 s (Figure 13.29f). Correlation between the period of the infragravity peak envelope and the significant wave height is shown in Figure 13.29g. Next, we looked at the correlation between the period of the infragravity peak envelope and the wave energy in individual frequency bins as observed at the local buoy. The best correlation was observed with the ocean waves with 14.3 s period for which the SWD is shown in Figure 13.29e,h. The correlation coefficient between the period of the infragravity peak envelope and the SWD observed in the individual bins at buoy 46042, as a function of the SWD bin period, is presented in

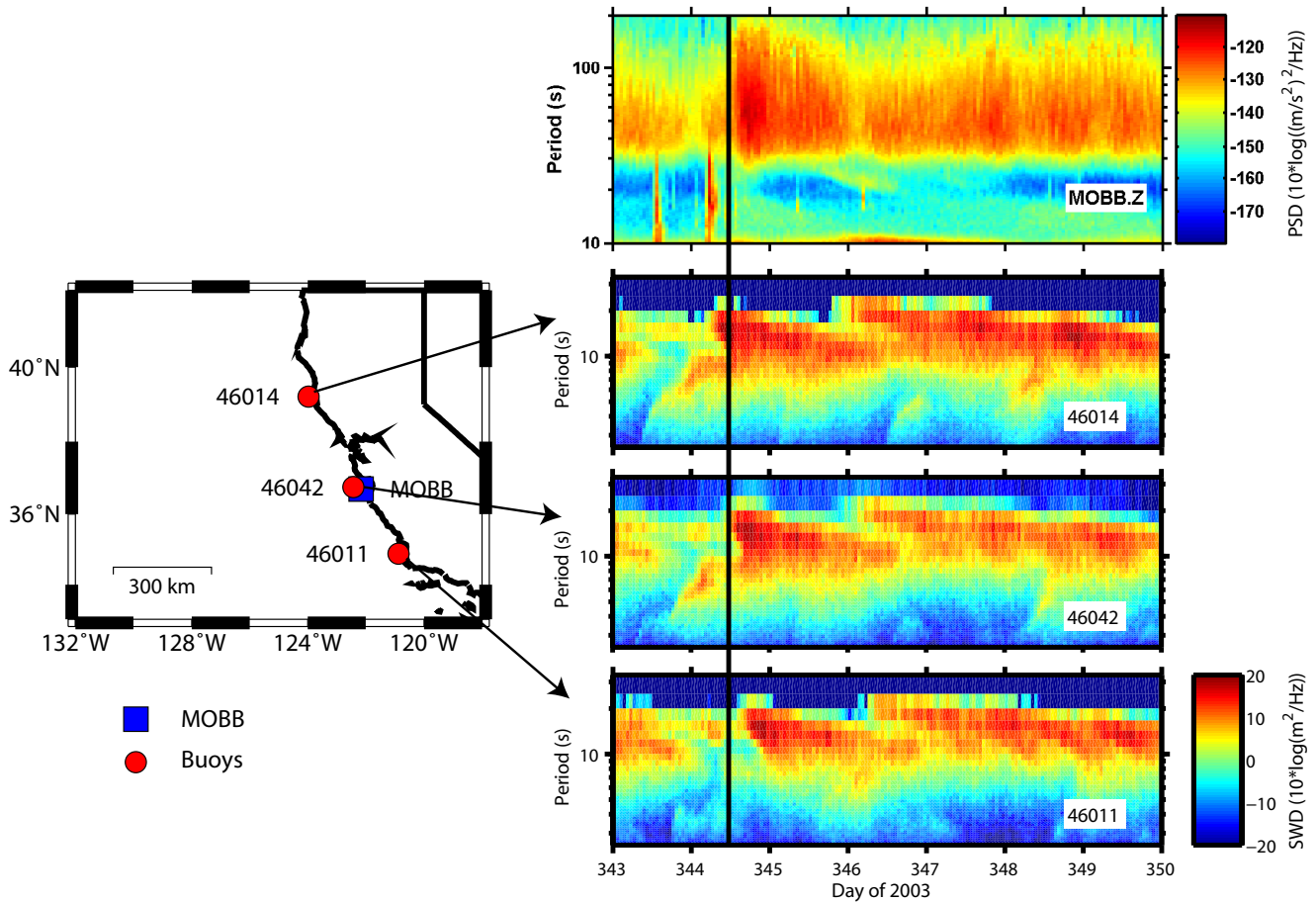


Figure 13.28: Left: The location of some of the NOAA buoys closest to the MOBB. Right: The power spectral density (PSD) for the vertical MOBB channel as a function of period and time (top). Bottom panels show the spectral wave density (SWD) calculated at 3 buoys. The vertical line indicates a sudden change of the infragravity peak width.

Figure 13.29i, and confirms that the infragravity peak long-period modulation correlates the strongest with the ocean wave energy at ~ 14 seconds.

A similar result can be obtained for other stormy periods at MOBB. This suggests that the short-period ocean waves are essential for the generation of the infragravity waves. It is interesting that the same period ocean waves are also the source of the microseisms noise, observed at the double frequency, at 6-7 s. This suggests that the generation mechanisms of infragravity waves and double frequency microseisms could be closely related.

14.4 Conclusions

Infragravity waves can be observed at the ocean bottom broadband seismic station MOBB. When compared to the energy of the short-period ocean waves recorded at the local buoys, infragravity waves in the longer than 20 s period band are found to be mainly locally generated from shorter period waves. Two types of modulation of the infragravity signal are observed. First, the entire in-

fragravity band is modulated in-phase with tides. It is possible that this is a result of the nonlinear exchange of energy between the short-period waves and tidal currents. Second, the low-frequency modulation of the observed infragravity peak is best correlated with the energy of the 14.3 s period ocean waves, suggesting a close relation of infragravity wave generation to that of double frequency microseisms.

14.5 Acknowledgements

The MOBB instrumentation, deployment, and maintenance were supported by the Lucile and David Packard Foundation funds to MBARI, the NSF Grant OCE9911392, and UC Berkeley funds to BSL.

14.6 References

Dolenc, D., B. Romanowicz, D. Stakes, P. McGill, and D. Neuhauser, Observations of infragravity waves at the Monterey ocean bottom broadband station

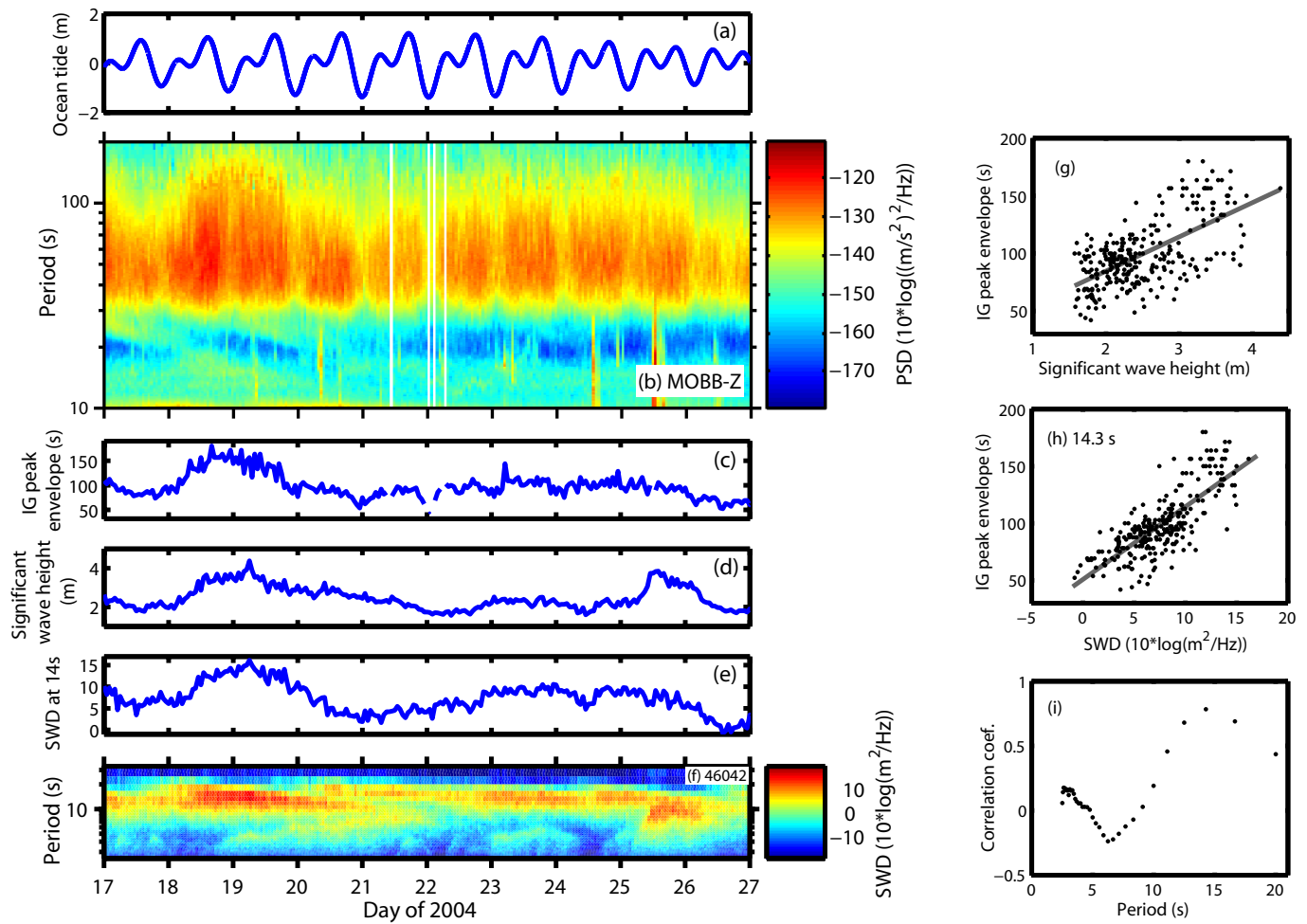


Figure 13.29: (a) Theoretical ocean tide at the MOBB location. (b) The power spectral density (PSD) for the vertical MOBB channel as a function of period and time. White lines indicate hours with some missing data. (c) The envelope of the infragravity peak presented in (b), taken at the long-period end, at the PSD value of -136 dB. (d) The significant wave height at the buoy 46042. (e) The spectral wave density (SWD) in the 14.3 s period bin at the buoy 46042. (f) The SWD at the buoy 46042 as a function of period and time. (g) The period of the infragravity peak envelope, taken at the long-period end, at the PSD value of -136 dB, as a function of the significant wave height as observed at the buoy 46042. Gray line shows best linear fit to the data. (h) The period of the infragravity peak envelope as a function of the SWD observed at the buoy 46042 in the 14.3 s period bin. Gray line shows best linear fit to the data. (i) The correlation coefficient between the period of the infragravity peak envelope and the SWD observed in the individual bins at buoy 46042, as a function of the SWD bin period.

(MOBB), *Geochem. Geophys. Geosyst.*, 6, Q09002, doi:10.1029/2005GC000988, 2005.

Louquet-Higgins, M. S. and R. W. Stewart, Changes in the form of short gravity waves on long waves and tidal currents, *J. Fluid Mech.*, 8, 565-583, 1960.

Louquet-Higgins, M. S. and R. W. Stewart, Radiation stresses in water waves; a physical discussion, with applications, *Deep-Sea Res.*, 11, 529-562, 1964.

Rhie, J. and B. Romanowicz, Excitation of Earth's continuous free oscillations by atmosphere-ocean-seafloor coupling, *Nature*, 431, 552-556, 2004.

Romanowicz, B., D. Stakes, R. Uhrhammer, P. McGill, D. Neuhauser, T. Ramirez, and D. Dolenc, The MOBB Experiment: A prototype permanent off-shore ocean bottom broadband station, *Eos Trans., AGU*, 84 (34), 325, 331-332, 2003.

Tanimoto, T., The oceanic excitation hypothesis for the continuous oscillation of the Earth, *Geophys. J. Int.*, 160, 276, 2005.

Webb, S. C., X. Zhang, and W. Crawford, Infragravity waves in the deep ocean, *J. Geophys. Res.*, 96, 2723-2736, 1991.

15. Seismic Imaging OF the Newberry Hotspot Track

Mei Xue and Richard M. Allen

15.1 Introduction

Located in the northwestern United States, the Newberry hotspot track, along the Oregon High Lava Plains (HLP), consists of a sequence of age-progressive silicic volcanic domes and lava flows, showing a monotonic age progression from east to west ending at the Newberry Caldera. While mantle plumes are often called upon to explain hotspot tracks, the Newberry hotspot track cannot be the product of plate motion over a stationary mantle source as its orientation is $\sim 120^\circ$ to plate motion, making it a good case study for alternative causal mechanisms of hotspot tracks. Four tectonic models have been proposed: (1) subduction counterflow (*Draper, 1991; Jordan et al., 2004*), (2) gravitational flow along lithospheric topography (*Humphreys et al., 2000; Jordan et al., 2004*), (3) lithospheric faulting (*Rocchi et al., 2003*), and (4) extension of Basin and Range (*Christiansen et al., 2002*). To study the Newberry track, the Oregon Array for Teleseismic Study (OATS) was installed in May 2003 and will operate until the spring of 2006 (Figure 13.30). Data is archived at DMC.

15.2 Shear-wave splits

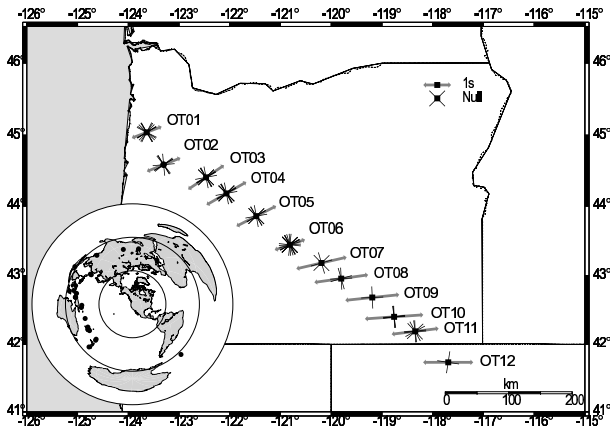


Figure 13.30: Splitting results across Oregon. The thick gray line indicates the result after stacking all useful events at each station. The line orientation gives the fast splitting direction, and its length is linearly proportional to splitting time. The thin black crosses indicate null results. Inset: Distribution of the 27 events used in the SKS splitting study.

To constrain the possible flow fields beneath the Newberry track, preliminary SKS splitting measurements were made for 27 events at 12 OATS stations. A grad-

ual rotation of fast direction is observed from ENE-WSW at the northwest end of the array to E-W to the southeast and the delay times average 1.65 sec (Figure 13.30). The SKS splits imply anisotropy primarily comes from asthenosphere and anisotropy orientation does not vary with depth beneath the track. Since the observed fast directions are not parallel to the Newberry track, and both the subduction counterflow model and the gravitational flow model require flow along the track, the lithospheric models are the most likely causal processes.

15.3 Teleseismic tomography results

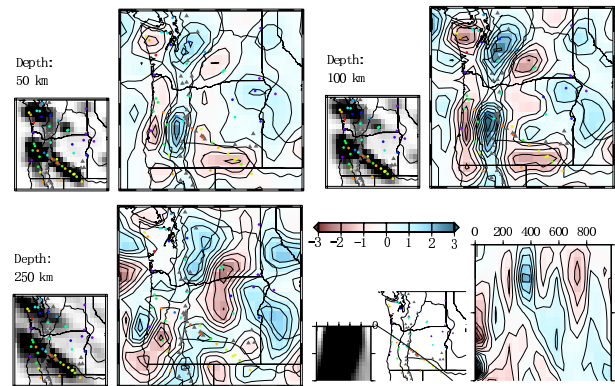


Figure 13.31: Ray density plots and horizontal slices through the Vs model at (a) 50 km depth, (b) 100 km depth and (c) 250 km depth. (d) shows vertical slice through the Vs model along the Newberry track with the ray density plot on the left, the map of cross-section in the middle, and the vertical slice on the right. The model grid spacing is 50 km in all three dimensions.

This study uses a total of 53 broad-band seismic stations, 12 from OATS, and others from nearby permanent networks (BK, CC, US, UO, UW, PN, IU, TA, LI) and temporary deployments (XJ, YC, YS). In this preliminary study, we inspect events with magnitude 6.0 and above from July 19th, 2003 to Nov. 11th, 2004. For the S wave velocity model, a total of 95 events with useable S and SKS phases were recorded at 45 stations, and a total number of 2148 rays were used in the Vs inversion. Our preliminary tomography results show large low velocity residuals all along the Newberry track to a depth ~ 150 km and no further continuation to the deep mantle (Figure 13.31). This suggests there is no migrating melt body in the asthenosphere beneath the region, and supports the conclusion from our SKS splitting analysis that

the Newberry track is more likely a result of lithospheric processes.

15.4 Conclusion

Preliminary results of SKS splitting and teleseismic tomography suggest a lithospheric origin for Newberry. First, there is no asthenospheric anomaly beneath the Newberry, instead low anomaly is beneath all of the HLP. Second, no flow observed in asthenosphere along the track.

15.5 Acknowledgements

This work was supported by the Graduate School of the University of Wisconsin-Madison. We thank Lee Powell, Neal Lord, Andrew Lockman, Robert Pyszalski, Bill Unger for helping installation of stations and collecting data.

15.6 References

Christensen, R.L., and R.S. Yeats, Post-Laramide geology of the U.S. Cordilleran region, in *The Cordilleran orogen: Conterminous U.S.*, edited by M.L. Zoback, pp. 261-406, Geological Society of America, Boulder, Colorado, 1992.

Christiansen, R.L., G.R. Foulger, and J.R. Evans, Upper-mantle origin of the Yellowstone Hotspot, *GSA Bulletin*, 114(10), 1245-1256, 2002.

Draper, D.S., Late Cenozoic Bimodal Magmatism in the Northern Basin and Range Province of Southeastern Oregon, *Journal of Volcanology and Geothermal Research*, 47(3-4), 299-328, 1991.

Humphreys, E.D., K.G. Dueker, D.L. Schutt, and R.B. Smith, Beneath Yellowstone: Evaluating plume and non-plume models using teleseismic images of the upper mantle, *GSA Today*, 10(12), 1-7, 2000.

Jordan, B.T., A.L. Grunder, R.A. Duncan, and A.L. Deino, Geochronology of age-progressive volcanism of the Oregon High Lava Plains: Implications for the plume interpretation of Yellowstone, *Journal of Geophysical Research*, 109 (B10202), doi:10.1029/2003JB002776, 2004.

Lawrence, R.D., Strike-Slip Faulting Terminates Basin and Range Province in Oregon, *Geological Society of America Bulletin*, 87(6), 846-850, 1976.

Macleod, N.S., G.W. Walker, and E.H. McKee, Geothermal significance of eastward increase in age of upper Cenozoic rhyolitic domes, in *Second United Nations Symposium on the Development and use of Geothermal Resources*, pp. 465-474, U.S. Government Printing Office, Washington D.C., 1976.

Pierce, K.L., and W.J. Morgan, The track of the Yellowstone hotspot: Volcanism, faulting, and uplift, in *Regional geology of eastern Idaho and western Wyoming*, edited by P. L.B., pp. 1-53, 1992.

Rocchi, S., F. Storti, V.G. Di, and F. Rossetti, *Intraplate strike-slip tectonics as an alternative to mantle plume activity, in Intraplate strike-slip deformation belts.*, edited by F. Salvini, Geological Society of London. London, United Kingdom, 2003.

16. Fluid-Influenced Faulting in the Long Valley Volcanic Region

Dennise C. Templeton and Douglas Dreger

16.1 Introduction

In volcanic areas, deviations from the usual double-couple (DC) model of shear faulting may be able to illuminate a link between the source process of an earthquake and fluids associated with the geothermal or magmatic system. These non-double-couple (non-DC) earthquakes have mechanisms vastly different from simple shear along a linear fault plane and are characterized by a compensated-linear-vector-dipole (CLVD) component, suggesting either fluid involvement or complex shear failure, and/or an isotropic component which describes volume changes in the source region.

In this study, we investigated the source kinematics of events greater than M3.5 occurring between 1993 - 2003 within a 100 km wide circular area centered at the Long Valley caldera, which includes the Mono-Inyo Craters to the north and the Sierra Nevada Block to the south, to identify events with significant coseismic volume changes. In this active geothermal and magmatic area, we treat coseismic volume changes as an indicator of fluid involvement at the source.

16.2 Data and Methodology

In this study we solved for four different source models: DC, deviatoric (DC+CLVD), DC+isotropic and the full moment tensor model (DC+CLVD+isotropic). The full moment tensor model can characterize source processes involving a combination of tensile and shear faulting (*Julian et al.*, 1998). The deviatoric moment tensor model describes volume conserving source processes which deviate from a simple DC mechanism. DC+isotropic source mechanisms have been used to describe combinations of near-simultaneous faulting near an underground explosion source (*Massé*, 1981). The pure DC model assumes that the earthquake source is best modeled as shear along a linear fault plane and a priori sets the CLVD and volumetric components to zero.

For the DC and DC+isotropic models, a grid search method iterating over strike, dip, rake, DC moment and isotropic moment, which is equal to zero in the pure DC case, was used to find the solution which best fit the observed three-component Berkeley Digital Seismic Network waveforms bandpass filtered between 0.02 and 0.05 Hz. For the deviatoric and full moment tensor models, the second rank symmetric seismic moment tensor is solved by linearly inverting complete three-component filtered broadband seismograms in the time domain using a weighted least squares approach. Green's functions for all four models were computed utilizing a frequency

wave-number integration method and the SoCal velocity model (*Dreger and Helmberger*, 1993) for source depths every 3 km between 2 - 17 km.

When testing more complex source models, the variance reduction usually increased with increasing complexity. F test statistics were performed to determine if the additional CLVD and/or volumetric components represented a true aspect of the source mechanism or if they were simply added non-physical parameters in the inversion.

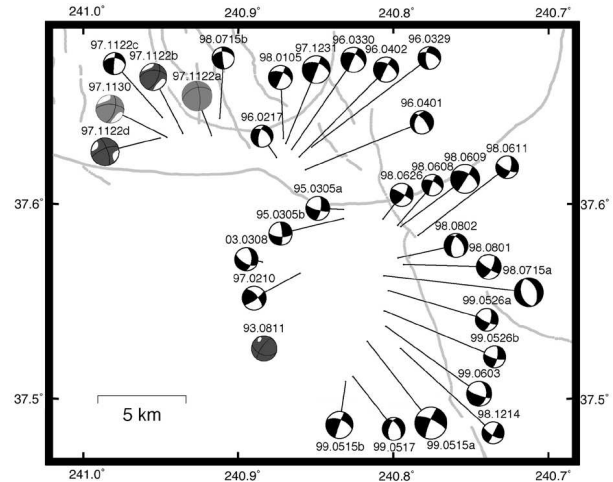


Figure 13.32: DC solutions shown in black. DC+isotropic solutions shown as dark gray. Full moment tensor solutions shown as light gray. Date of event shown as YY.MM.DD.

16.3 Results

Within the chosen space and time constraints, 33 high quality events are identified that have solutions with three or more stations in their inversion. Of these 33 events, 28 are best characterized using a simple DC model, four by a DC+isotropic source model, and one by a full moment tensor model. The isotropic components of the five non-DC events were between 27-48% of the total moment released for each event. All non-DC events are located either in the south moat of the caldera or in the Sierra Nevada block.

The first event with a significant volumetric component occurred on August 11, 1993 in the Sierra Nevada block during the Red Slate Mountain earthquake swarm. Previously, the only non-DC events to occur in this area

were a 1978 M5.8 event and two M6 1980 events (*Julian and Sipkin, 1985*). Event 93.08.11, however, did not occur along the same fault planes as these earlier events. Additionally, it is not known if the earlier non-DC components were due to fluid involvement or complex shear faulting.

The next four events with coseismic volume increases occurred in November 1997 in the south moat of the Long Valley caldera during a period of unrest at the peak of a large earthquake swarm. These south moat events had been previously identified as having significant volumetric components by *Dreger et al. (2000)* however, the current study investigates a wider range of possible source mechanisms. A previous study using a dense temporary seismic network operating during the summer of 1997 showed that most of 26 microearthquakes less than M3.1 were characterized by positive CLVD and isotropic components (*Foulger et al., 2004*). The difference in the total number of isotropic events between our two studies suggests that physical conditions which produce isotropic components are scale dependent, possibly in terms of the ability of individual high pressure reservoirs to sustain pressurization during the faulting process as the crack or fault grows larger.

We were not able to analyze the source process of earthquakes in or near the vicinity of the Mono-Inyo volcanic chain or Mammoth Mountain because events greater than M3.5 were not recorded during the time interval investigated by this study.

Pure DC events sometimes occurred close in space and time to events with significant non-DC components. For example, DC Event 97.11.22c occurred 10 minutes before non-DC Event 97.11.22d and was located just a few kilometers away from all four south moat non-DC events. In some cases, DC events determined by this study were located near previously identified fluid influenced microseismicity structures. For example, Events 97.12.31 and 98.01.05 occurred close in space to a microseismicity trend inferred to be a compensated tensile failure plane (*Foulger et al., 2004*). Thus, it appears that the factors necessary to produce isotropic components only coalesce and trigger non-DC events within a relatively small physical and temporal window in the Long Valley volcanic region.

16.4 Stability of Isotropic Component

We performed Jackknife tests on the four events with significant isotropic components that had four or more stations in their solution (Events 97.11.22a, 97.11.22b, 97.11.22d, and 97.11.30) to determine the likelihood of non-DC events incorrectly being identified as DC events. For all station combinations of three or more, we determined if the volumetric component was significant at or above the 95% significance level by using the F test statistic. All 52 combinations of four or more stations re-

covered the statistically significant isotropic component. For solutions with three stations, six iterations out of 60 failed to recover the isotropic component. It is reasonable to assume that significant isotropic components can be recovered with as few as three, but preferably with at least four, stations in the solution.

We also investigated the possibility of obtaining a spurious isotropic component due to poor data coverage. For this test, we took three high quality DC solutions (Events 97.12.31, 98.06.09, and 98.07.15) and performed Jackknife tests to see if any combination of three or more stations would result in a statistically significant isotropic component. Of 75 three station solutions, one returned a false positive. Of 65 four station solutions, three incorrectly determined that the event had a significant isotropic component. Five and six station solutions did not return false positives. Thus, we feel confident that the isotropic components of our non-DC events with at least five stations in their inversion are not due to poor data coverage. This test, however, casts a small amount of doubt as to the validity of non-DC Event 93.08.11 which has only three stations in its solution.

16.5 Acknowledgements

This research was supported by NSF through contract EAR-0087147.

16.6 References

- Dreger, D. S., H. Tkalic, and M. Johnston, Dilational processes accompanying earthquakes in the Long Valley Caldera, *Science*, 288, 122 - 125, 2000.
- Dreger, D. S., and D. V. Helmberger, Determination of source parameters at regional distances with three-component sparse network data, *J. Geophys. Res.*, 98, 8107 - 8125, 1993
- Foulger, G. R., B. R. Julian, D. P. Hill, A. M. Pitt, P. E. Malin, and E. Shalev, Non-double-couple microearthquakes at Long Valley caldera, California, provide evidence for hydraulic fracturing, *J. Volcanol. Geothermal Res.*, 132, 45 - 71, 2004.
- Julian, B. R., A. D. Miller, and G. R. Foulger, Non-double-couple earthquakes, 2, Theory, *Rev. Geophys.*, 36, 525 - 549, 1998.
- Julian, B. R., and S. A. Sipkin, Earthquake processes in the Long Valley Caldera area, California, *J. Geophys. Res.*, 90, 11,155 - 11,169, 1985.
- Massé, R. P., Review of seismic source models for underground nuclear explosions, *Bull. Seismol. Soc. Am.*, 71, 1249 - 1268, 1985.
- Templeton, D. C., and D. S. Dreger, Non-Double-Couple Earthquakes in the Long Valley Volcanic Region, *Bull. Seismol. Soc. Am.*, in press.

17. Measuring and Modeling Fluid Movements in Volcanoes: Insights from Continuous Broadband Seismic Monitoring at Galeras Volcano, Colombia

Margaret Hellweg, Douglas Dreger and Leigh House (Los Alamos National Laboratory)

17.1 Introduction

In July, 2004, after 11 years of relative quiescence, Galeras Volcano (Colombia) renewed its eruptive activity with a sequence of explosions and ash emissions. Initial evidence of the activity transition appeared in gas measurements from the instruments of the multiparameter station (Seidl et al, 2003, Faber et al, 2003) in early June, followed by a strong increase in the shallow seismic activity below the active cone on June 27 (Gómez et al, 2004). As is the case at many other volcanoes, the most clear evidence for the transition came in the form of seismic swarms, which included both volcano tectonic and long-period events, and tremor. Eruptive activity commenced with two brief episodes of ash emission, on July 16 and July 21. Since then, ash emissions and explosions have been intermittent. An episode lasting from August 11 - 19 began with a large explosion and released more ash than any individual episode from 1989 to 1993. Sudden deformation, as well as changes in the electric and magnetic fields at the crater electromagnetic (EM) station and the gas parameters, such as CO₂ concentration and fumarole temperature, accompanied the ash emissions on July 16 and July 21. While the EM and gas sensors were lost to ashfall by the end of July, monitoring continued via seismometers, tiltmeters and visual inspection.

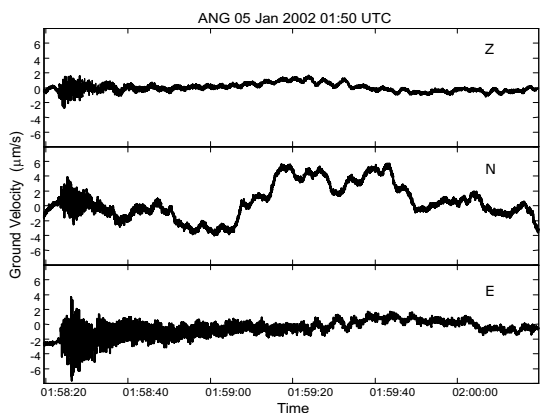


Figure 13.33: Raw velocity seismograms of a tornillo recorded with a broadband seismometer.

17.2 Tornillos and Explosions

We have been analysing tornillos, a particular type of seismic signal from Galeras, to learn about the movement of fluids in the volcanic system. In 1992 and 1993, tornillos occurred at Galeras prior to explosions (Narváez et al, 1997), so they have been considered a precursory signal. They are distinct seismic events with identifiable onsets and relatively long, gradually decaying event tails (codas) and their name comes from the resemblance of their shape on the seismic record to a screw (Figure 13.33). Ninety tornillos recorded at Galeras Volcano, Colombia, from December 1999, to December 2002, were not immediately associated with explosions. Then, no tornillos were observed from December 2002, until well after the beginning of eruptive activity, in September 2004 (Figure 13.34). As a class, the tornillos are complex, each having from one to 15 spectral peaks between 1 and 40 Hz. The peaks for frequencies which extend into the coda are extremely narrow, while those present only during the initial excitation are relatively broad. The frequency of the lowest spectral peak present in any of the tornillos recorded between December 1999, and December 2002, was higher than 1.6 Hz. In contrast, tornillos occurring after the eruption began included frequencies between 1.0 and 1.3 Hz.

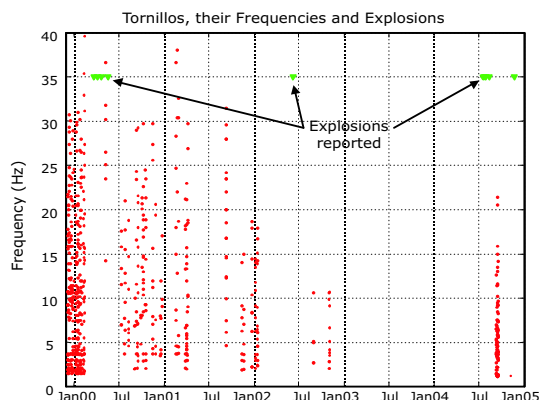


Figure 13.34: Occurrence of tornillos and their frequencies (dots). Triangles mark reported explosions.

Most analysis of tornillos has concentrated on the coda which gives them their name. However, each tornillo waveform is actually made up of three parts (Figure 13.35). In the high quality broadband recordings, the tornillos start with a very small, but clearly recognizable P-onset. This is followed about 0.25 s later by the arrival of wave energy on the horizontal traces, probably S-waves. This arrival becomes a complex wavepacket lasting between two and three seconds which then transitions into the coda. Preliminary comparisons of these wavepackets for many different tornillos suggest two things: that they can be classified into families, and that these families are only indirectly related to the exact frequency or family of frequencies present in the long-lasting coda into which they segue.

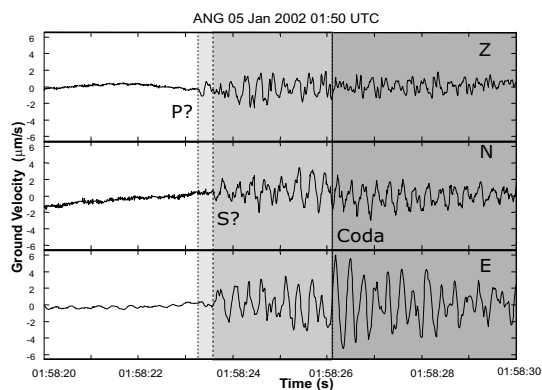


Figure 13.35: Displacement seismograms of the beginning of a tornillo. The first onset has polarization consistent with a P-wave, while the second onset is likely to be an S-wave. It is followed by a 2-3 s transition before the characteristic coda develops.

We are currently investigating and quantifying the characteristics of both the onsets and the intermediate wavepackets more thoroughly, as they bear important information about the mechanism which triggers a tornillo.

For the spectral peaks below 5 Hz, the polarization both remains constant during an individual tornillo, and varies little from one tornillo to the next. This suggests that tornillos are all generated within a limited volume of the volcanic edifice. The variation in the polarization at higher frequencies should allow us to constrain the size of this volume (Hellweg, 2003)..

17.3 Perspectives

Details in the tornillo onset and the intermediate wavepacket, and their relationships to the characteristics of the tornillo coda, are important factors which will enable us to derive a more thorough picture of what physical process in the volcano actually produces the tornillos. In particular, the tornillos associated with the recent activity give interesting clues: why are their frequencies lower and what governs the timing of their occurrence in the eruption sequence?

17.4 Acknowledgements

This project is funded by U.C. Berkeley - Los Alamos National Laboratory collaborative Institute for Geophysics and Planetary Physics Project number 04-1407. Tornillo data have been acquired as part of a cooperative project between the Bundesanstalt für Geowissenschaften und Rohstoffe (Germany) and the Instituto de Investigación e Información Geocientífica Minero-Ambiental y Nuclear (Colombia) on Multiparameter Monitoring of Volcanoes.

17.5 References

Faber, E., C. Morán, J. Poggenburg, G. Garzón, and M. Teschner, Continuous gas monitoring at Galeras Volcano, Colombia: First evidence, *J. Volc. Geotherm. Res.*, 25, 13-23, 2003.

Gómez, D., M. Hellweg, B. Buttkus, F. Böker, M.L. Calvache, G. Cortés, E. Faber, F. Gil Cruz, S. Greinwald, C. Laverde, L. Narváez, A. Ortega, H. Rademacher, G. Sandmann, D. Seidl, B. Silva and R. Torres, A volcano reawakens: Multiparameter observations of activity transition at Galeras Volcano (Colombia), *EOS Trans. AGU*, 85(47), *Fall Meet. Supp.*, Abstract V11B-1423, 2004.

Hellweg, M., The Polarization of Volcanic Seismic Signals: Medium or Source?, *J. Volc. Geotherm. Res.*, 128, 159-176, 2003.

Narváez, M.L., R.A. Torres, D.M. Gómez, G.P.J. Cortés, H.V. Cepeda, and J. Stix, Tornillo-type seismic signals at Galeras volcano, Colombia, 1992-1993. *J. Volcanol. Geotherm. Res.*, 77, 159-171, 1997.

Seidl, D., M. Hellweg, M. Calvache, D. Gómez, A. Ortega, R. Torres, F. Böker, B. Buttkus, E. Faber and S. Greinwald, The multiparameter-station at Galeras Volcano (Colombia): Concept and realization, *J. Volc. Geotherm. Res.*, 125, 1-12, 2003

Seidl, D. and M. Hellweg, Parametrization of multi-chromatic tornillo signals observed at Galeras Volcano (Colombia), *J. Volc. Geotherm. Res.*, 125, 171-189, 2003

18. Independent Okhotsk and Amurian Microplate Tectonics of Northeast Asia

Edwin (Trey) Apel, Roland Bürgmann, Misha Kogan (Columbia), and Robert King (MIT)

18.1 Introduction

The possible existence of independently rotating Okhotsk and Amurian microplates has been examined by many in an attempt to explain both seismological and geologic data in Northeast Asia (Cook *et al.*, 1986; Seno *et al.*, 1996). Geodetic measurements can be used to fully characterize the motion of tectonic plates; however, because most GPS sites in this region are in such close proximity to plate boundaries, previous attempts to firmly confirm or refute an independent Okhotsk plate have been inconclusive (Heki *et al.*, 1999; Steblou *et al.*, 2003). Independent Amurian plate motion is notably more difficult to constrain because of the uncertainty of the southwestern plate boundary and the sparsely spaced geodetic data.

Horizontal surface velocities of 122 GPS sites (82 from within the proposed Okhotsk and Amurian plate boundaries) constrain the plate kinematics of northeast Asia and allow for a rigorous test of the possibility of independent Okhotsk and Amurian plate motion. We use a block modeling approach to incorporate both rigid block rotation and near-boundary elastic strain accumulation effects in a formal inversion of the GPS velocities. Considered models include scenarios with and without independent microplates and a number of different plate boundary locations and locking depths.

18.2 GPS Velocities

The GPS velocities used in our inversion are from an updated velocity field of 151 global stations by (Steblov *et al.* 2003). We include data from additional campaign stations from central Sakhalin (Kogan *et al.*, 2003) and the Kamchatka peninsula (Bürgmann *et al.*, 2005), and from sites in northern Japan that are part of the continuous Japanese GSI network in our complete solution. These data were processed using GAMIT/GLOBK by Bob King at MIT and Misha Kogan at Columbia. Processing details can be found in (Steblov *et al.*, 2003).

In addition to our own analysis we integrate GPS-station velocities from published work in the region that help with defining the deformation patterns for the Baikal and central Amurian regions (Calais *et al.*, 2003). We also include selected stations from Zhang *et al.* (2004) that fell within or near the boundaries of the proposed Amurian microplate. These velocities were combined with our solutions by rotating them into a common reference frame. The sites selected for our inversion are shown in Figure 13.36 and Figure 13.37.

18.3 Blocks

We define our plates as rigid blocks on a spherical earth bounded by dislocations in an elastic halfspace and invert for poles and rates of rotation that minimize the misfit to the GPS velocities using an extension of the block modeling code by Meade and Hager (2005). The segments that bound the blocks represent uniformly slipping elastic dislocations locked to some specified depth. Because our inversion combines rigid block rotation with elastic strain accumulation effects, the parameterization of the block boundary geometry is critical. Geometry of the block boundaries is based heavily on seismicity and adopted from prior analyses (Bürgmann *et al.*, 2005) or adjusted as indicated by the geodetic data (Kogan *et al.*, 2003).

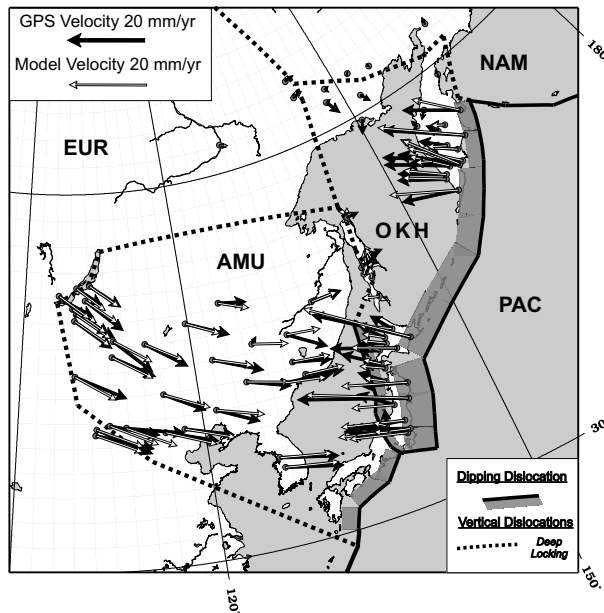


Figure 13.36: GPS velocities, in black, are shown in a fixed North American reference frame. Predicted model velocities from our 5-plate model are shown in white and show good fit to the data.

We invert the horizontal GPS velocities for poles of rotation constrained by the prescribed block geometry defined above. Systematic patterns in the residual velocities (observed minus predicted) are used as an indicator of where and how the model matches the observed surface velocities. Misfit statistics are used to formally evaluate

the statistical significance of the plate kinematic scenarios we test.

18.4 Results

Independent Okhotsk plate motion is tested using three main block configurations. In our 3-plate system we assume that the Okhotsk region is part of the North American plate and Amuria belongs to Eurasia. Our 4-plate model allows the Okhotsk block to rotate independently while the 5-plate model also includes an independently rotating Amurian block. Our inversions favor a scenario with independent Okhotsk plate motion but does not formally require it. The F-test statistic indicates that the improved fit is significant at 92% confidence. Independent Amurian plate motion is significant only at 69% confidence. The best fitting poles of rotation for our 5-plate model are shown in Figure 13.37.

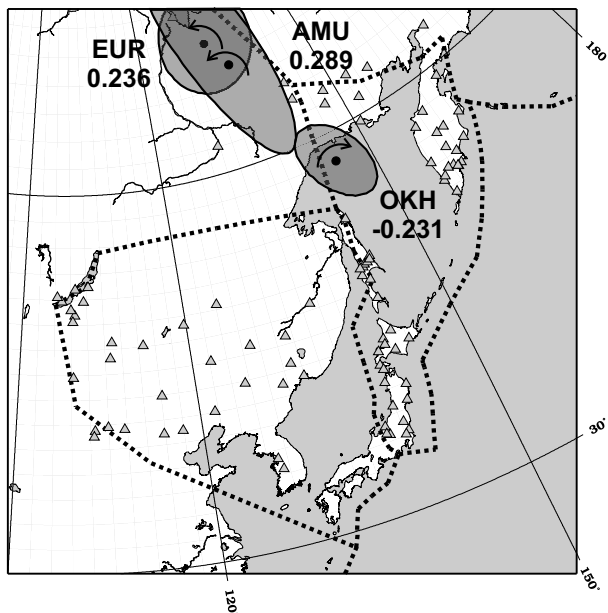


Figure 13.37: Poles of rotation for the Amurian, Okhotsk, and Eurasian plates. Error ellipses represent 95% confidence bounds. Triangles represent the locations of the GPS sites used in this study.

18.5 Discussion

The plate-motion parameters of independently rotating Okhotsk and Amurian plates are consistent with the style of active deformation inferred from focal mechanism solutions. For example, our inversions predict right-lateral motion in northern Sakhalin, oblique contraction in southern Sakhalin, and little to no active deformation in the sub-marine crust north of Sakhalin. Predicted opening in the Baikal region is also consistent with historical seismicity and active structures.

Subtle changes in block and segment geometry (e.g. dip) within or near subduction zones can cause significant changes in the estimated pole of rotation of the Okhotsk plate. This is due, in large part, to the close proximity of most GPS stations in northeast Asia to these plate boundaries, such as the Kamchatka-Kurile subduction zone. GPS velocities on the Kamchatka peninsula and in Japan capture a complex pattern associated with the heterogeneously locked subduction zone that may require more complex models. Additional blocks may also affect the determination of an independently rotating Okhotsk plate. Future work will examine the potential role of adjacent blocks such as the Philippine, Bering, northern Honshu, and Magadan blocks.

18.6 References

- Bürgmann, R., M. Kogan, G. Steblov, G. Hiley, V. Levin, and E. Apel, Interseismic coupling and asperity distribution along the Kamchatka subduction zone, *Journal of Geophysical Research*, 110, doi:10.1029/2005JB003648, 2005.
- Calais, E., M. Vergnolle, V. Sankov, A. Lukhnev, A. Miroshnitchenko, S. Amarjargal, and J. Deverchere, GPS measurements of crustal deformation in the Baikal-Mongolia area (1994-2002): Implications for current kinematics of Asia, *Journal of Geophysical Research*, 108(B10), 2003.
- Cook, D. B., K. Fujita, and C. A. McMullen (1986), Present-day plate interactions in northeast Asia - North-American, Eurasian, and Okhotsk plates, *Journal of Geodynamics*, 6(1-4), p. 33, 1986.
- Heki, K., S. Miyazaki, H. Takahashi, M. Kasahara, F. Kimata, S. Miura, N. F. Vasilenko, A. Ivashchenko, and K. D. An, The Amurian Plate motion and current plate kinematics in Eastern Asia, *Journal of Geophysical Research*, 104(B12), p. 29147, 1999.
- Meade, B. J., and B. H. Hager, Block models of crustal motion in southern California constrained by GPS measurements, *Journal of Geophysical Research*, 110, B03403, doi:10.1029/2004JB003209, 2005.
- Seno, T., T. Sakurai, and S. Stein, Can the Okhotsk plate be discriminated from the North American plate?, *Journal of Geophysical Research*, 101(B5), p. 11305, 1996.
- Steblov, G. M., M. G. Kogan, R. W. King, C. H. Scholz, R. Bürgmann, and D. I. Frolov, Imprint of the North American Plate in Siberia revealed by GPS, *Geophysical Research Letters*, 30(18), 2003.
- Zhang, P. Z., Z. Shen, M. Wang, W. J. Gan, R. Bürgmann, and P. Molnar, Continuous deformation of the Tibetan plateau from global positioning system data, *Geology*, 32(9), p. 809, 2004.

19. Crustal Deformation Along the Northern San Andreas Fault System

Mark H. Murray

19.1 Introduction

The San Andreas fault system in northern California includes three sub-parallel right-lateral faults: the San Andreas, Ma'acama, and Bartlett Springs. This northernmost segment is the youngest portion of the fault system, forming in the wake of the northwestwardly propagating Mendocino triple junction where the Pacific, North America, and Gorda (southern Juan de Fuca) plates meet. The Pacific plate moves about 35-40 mm/yr relative to central California across a broad ~100-km zone in northern California. Additional deformation in eastern California and the Basin and Range province contribute to the total relative Pacific-North America motion of ~50 mm/yr. The San Andreas fault itself has been essentially aseismic and accumulating strain since it last ruptured in the great 1906 San Francisco earthquake, and no major earthquakes have occurred during the historical record on the more seismically active Ma'acama, and Bartlett Springs faults, which are northern extensions of the Hayward-Rodgers Creek and Calaveras-Concord-Green Valley faults in the San Francisco Bay area. Our earlier geodetic studies showed that the inferred slip rate on the Ma'acama fault ($13.9^{+4.1}_{-2.8}$ mm/yr) implied an accumulated slip deficit large enough to generate a magnitude 7 earthquake, posing a significant seismic hazard (Frey Mueller *et al.*, 1999).

Since 2003, we have been resurveying sites measured in our previous studies plus about 40 additional sites, originally surveyed by Caltrans and NGS (Murray, 2004). The additional sites are located along the San Andreas fault system just north the San Francisco Bay and will improve monitoring along the Rodgers Creek and Green Valley faults. Most of the monuments were last observed in 1993–1995, so the new observations significantly improve the velocity estimates and models of average interseismic strain accumulation, including possible spatial variations along the fault system. Additional sites in the region between the southern and northern portions of the network are planned for resurveying in the future. The entire network spans the region from Pt. Reyes to Cape Mendocino. Together with planned PBO stations, it forms a primary monitoring network for future observations to detect temporal variations in deformation.

19.2 Deformation

Figure 13.38 shows site velocities estimated using the GAMIT/GLOBK software package for the 1994-2004 period relative to stable North America, as defined by a set of 20 fiducial stations. We are currently processing the

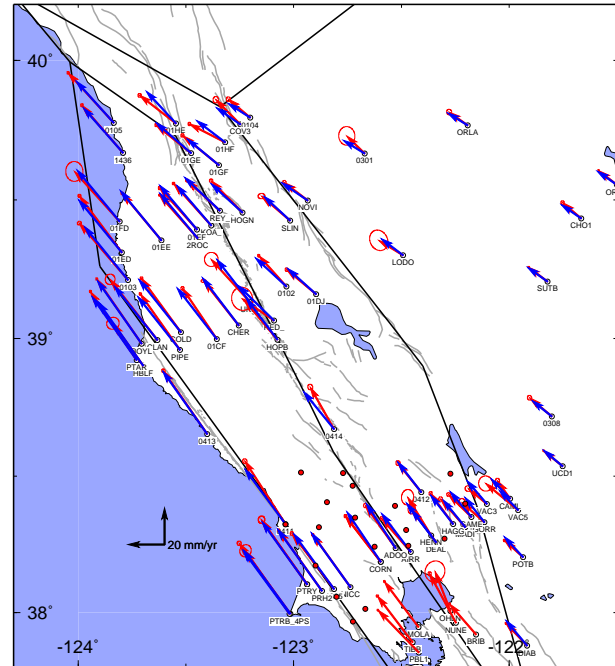


Figure 13.38: Velocities of sites in the Coast Ranges relative to North America, with 95% confidence regions assuming white-noise process only. Included are sites from this study plus sites from the BARD continuous network and the USGS North Bay profile. Arrows with ellipses, observed velocities. Arrows without ellipses, velocities predicted from angular velocity-backslip block model assuming block boundaries (heavy black lines). We assume Pacific, North America, and Sierran-Great Valley blocks, plus 2 small blocks between the San Andreas, Ma'acama, and Bartlett Springs faults. The most significant misfits, such as near Cape Mendocino, can be reduced by refining the fault geometry. Additional sites in the southern portion of the network (circles), have been recently re-measured.

data from the most recent surveys that will provide new estimates of velocities for sites between the southern and northern profiles shown. Most of the velocities are derived from data spanning 8-10 years, whereas those with the largest error ellipses include data from only a 4 year span. The easternmost stations exhibit motions typically associated with Sierran-Great Valley block (ORLA: 12.5 mm/yr NW). The westernmost sites are moving close to the Pacific plate rate (PTAR: 45.9 mm/yr NW). Fault-normal contraction is observed east of the Ma'acama

fault, in the region of the Coast Ranges near the Central Valley where similar contraction has been observed elsewhere (e.g., Murray and Segall, 2001).

Also shown in Figure 13.38 are velocities predicted by angular velocity-fault backslip modeling techniques (e.g., Murray and Segall, 2001) to account for both far-field plate motions and interseismic strain accumulation. We are developing a 3D fault model and applying the same modeling approach that we used in our BAVU study of the San Francisco Bay area (d'Allesio et al., 2005). Preliminary results show that the agreement between observed and predicted velocities is typically less than the 2 mm/yr level. Misfits are larger in a few areas close to faults, such as along the central Ma'acama and near the MTJ, that should be decreased with further refinement of the fault geometry. Total deformation across the San Andreas fault system is 38 mm/yr, in agreement with previous studies, but deep slip is concentrated on the Ma'acama fault (24 mm/yr) and on the Bartlett Springs fault (10 mm/yr), with only 4 mm/yr on the San Andreas. We are currently investigating this result, which is due in part to the high-degree of correlation between the slip rates on the 3 faults, and will test methods for adding geologic and other information using Bayesian techniques, which should reduce the correlations on slip rates and provide better resolution on other parameters such as locking depths.

We are also working with D. Agnew (UCSD), R. King (MIT), and Z-K. Shen (UCLA) to combine these results with the BAVU, SCEC Crustal Motion Model (CMM 3.0), and other studies to provide an integrated California-wide velocity field. The preliminary velocity field is shown in Figure 20. and includes over 2000 stations. Additional stations will be included from the Cape Mendocino triple junction region. Results from this study will be used to develop a state-wide deformation and fault slip model that will be incorporated into a hazard assessment project by the Working Group on California Earthquake Probabilities under the auspices of the USGS. Preliminary results of the WGCEP project are expected in mid-2006.

19.3 Acknowledgements

We appreciate support for this project by the USGS NEHRP through grant numbers 02HQGR0064, 03HQGR0074, and 04HQGR0103. We thank André Basset, Maurizio Battaglia, Dennise Templeton, and especially Todd Williams for assistance conducting the survey.

19.4 References

d'Alessio, M. A., I. A. Johanson, R. Bürgmann, D. A. Schmidt, and M. H. Murray, Slicing up the San Francisco Bay Area: Block kinematics from GPS-derived

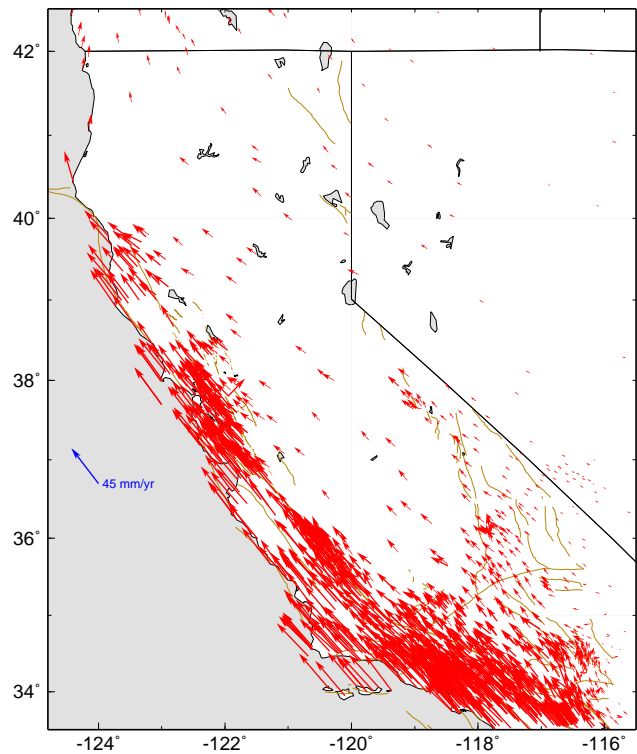


Figure 13.39: Velocities of sites in California relative to stable North America from a combination of velocities from this study, BAVU, the SCEC Crustal Motion Map, and other studies.

surface velocities, *J. Geophys. Res.*, 110, B06403, doi:10.1029/2004JB003496, 2005.

Frey Mueller, J. T., M. H. Murray, P. Segall, and D. Castillo, Kinematics of the Pacific-North America plate boundary zone, northern California, *J. Geophys. Res.*, 104, 7419–7442, 1999.

Murray, M. H., Crustal Deformation Along the Northern San Andreas Fault System From Geodetic and Geologic Data, EOS Trans. AGU, 85(47), Fall Meeting Suppl., Abstract G14A-04, 2004.

Murray, M. H., and P. Segall, Modeling broadscale deformation in northern California and Nevada from plate motions and elastic strain accumulation, *Geophys. Res. Lett.*, 28, 4315–4318, 2001.

20. Strong Ground Motions Derived from Geodetic Slip Models

Junkee Rhie, Douglas S. Dreger, Mark H. Murray

20.1 Introduction

Accurate estimation of near-fault strong ground motion from our basic understanding of faulting mechanisms and seismic wave propagation is an important goal in the field of earthquake engineering. In areas where there are no near-fault recordings of strong ground motions, such estimations can be crucial in producing a strong ground motion ShakeMap for emergency response purposes [e.g., Dreger and Kaverina, 2000; Dreger et al., 2005].

The main goal of this study is to develop a deterministic method to simulate temporal variations of slip from geodetic static displacements, and apply this method to derive reliable near-fault strong ground motion for earthquakes. Geodetic observations offer several advantages. Geodetic inversions can independently determine the orientation and fault finiteness quickly, whereas seismic inversions must first determine a moment tensor, and then test both possible nodal planes. Because geodetic slip-model inversions take less computer time than seismic inversions, this method can more quickly predict strong motion when real-time GPS observations are available. For emergency response, even a small improvement in time can be significant. Geodetic data sets also provide redundancy should seismic data sets be sparse or inaccessible in real-time, or difficulties arise in the multistage processing of the seismic data [e.g., Dreger and Kaverina, 2000].

20.2 Spatio-temporal slip model

Our method is based on the intuitive assumption that larger slip takes longer time to accumulate. This assumption follows from the well-known linear scaling relation between stress drop and slip velocity, which given that stress drop is basically independent of scalar seismic moment, implies that slip velocity is also essentially constant over the range of seismic moment and may be estimated by assuming regionally appropriate values of rigidity and shear wave velocity.

In practice, a spatially variable slip model is defined by a grid of point sources on a fault plane with rupture duration given by multiple time windows. We use empirical relations to define the average and minimum rise time and assume the scalar seismic moment M_0 from seismic or geodetic estimates. The regions with smallest slip take the minimum rise time to finish slipping, while the regions with larger slip require multiple time window based on the ratio of the spatially variable slip to the constant slip velocity. For a given level of slip, a larger assumed stress drop implies that more slip occurs in each

of the time windows resulting in a shorter overall duration (Figure 13.40). A circular rupture front initiates at the hypocenter given by seismic estimates and propagates with constant assumed rupture velocity. Slip is triggered when the rupture front reaches each point source and has a duration determined by the number of time windows appropriate for the level of slip at that point.

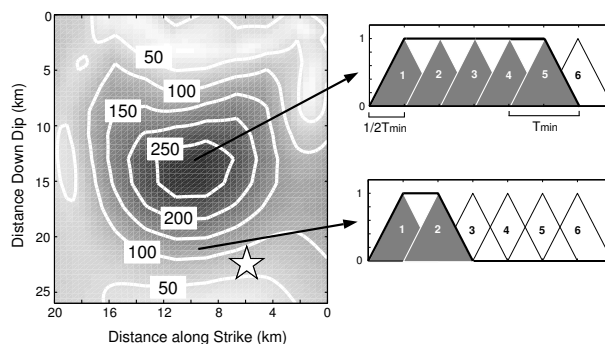


Figure 13.40: A schematic diagram showing how to determine the number of time windows for a variable-slip model. Left column shows the variable slip model on its rupture plane. White star indicates hypocenter of Northridge event. Two small panels on the right indicate necessary time windows (solid gray triangles) and final rise time curve (thick black) associated with slip patches indicated on slip distribution model.

20.3 The Northridge earthquake

We demonstrate the method by simulating strong ground motions from several slip models for the 17 January 1994 Mw 6.7 Northridge earthquake. A model derived from near-source strong ground motions, P and SH teleseismic body waves, and GPS and spirit leveling geodetic data provides reference time histories and peak ground motions for comparison with the motions obtained from the source models inferred from uniform and variable-slip models derived from geodetic data only.

To assess the methodology, we compare the observed and modeled velocity waveforms at near-source stations surrounding the event. To account for site effects, we applied site amplification factors to the waveforms based on the upper 30 m shear wave velocity. Amplification factors are calculated by considering differences in impedances for the rock and soil layers (upper 30 m) for a normal incidence seismic wave.

For most stations and components, predicted strong ground velocities for the reference and variable-slip models are similar to the observed velocities, whereas the uniform-slip model tended to underpredict the velocities. Simulated peak ground velocity (PGV) ShakeMaps for the three models showed similar behavior with the PGV values derived from the uniform-slip model significantly less than the other two models, possibly because the model is too smooth and spread in time. The simulated PGV for reference and variable-slip models showed the roughly the same extent of the 10-20 cm/s contours, the level at which structural damage can occur (Figure 13.41).

Since our objective is to develop a method that is practical in a rapid (on the order of 30 minutes) post-earthquake time frame, we made several simplifying assumptions such as constant slip and rupture velocity. As more information becomes available following an earthquake it may be possible to invert for models to resolve these parameters, but such analysis is not applicable in an automated fashion. Nevertheless, to first order, assuming rupture velocity is constant performs well in describing the overall directivity effect and in simulating peak ground velocity for ShakeMap purposes. Although studies of many events show that the slip velocity is not spatially constant, the assumption is generally applicable given that many spatio-temporal slip models have longer duration for larger slip.

Future work will test this methodology for other large, well-studied events, such as 2003 San Simeon, 1992 Landers, and 2004 Parkfield, to optimize the rules for time variation of slip. Combining the optimized rules and near real-time measurement and inversion of GPS displacement vectors can reduce the estimation time of the extent of near-fault strong ground shaking, and thus could facilitate better emergency response activities.

20.4 Acknowledgements

We appreciate support for this project by the USGS NEHRP through grant numbers 04HQGR0043 and 04HQGR0044.

20.5 References

- Dreger D., and A. Kaverina, Seismic remote sensing for the earthquake source process and near-source strong shaking: A case study of the October 16, 1999 Hector Mine earthquake, *Geophys. Res. Lett.*, 27, 1941-1944, 2000.
- Dreger, D. S., L. Gee, P. Lombard, M. H. Murray, and B. Romanowicz, Rapid finite-source analysis and near-fault strong ground motions - Application to the 2003 Mw 6.5 San Simeon and 2004 Mw 6.0 Parkfield earthquakes, *Seism. Res. Lett.*, 76, 40-48, 2005.

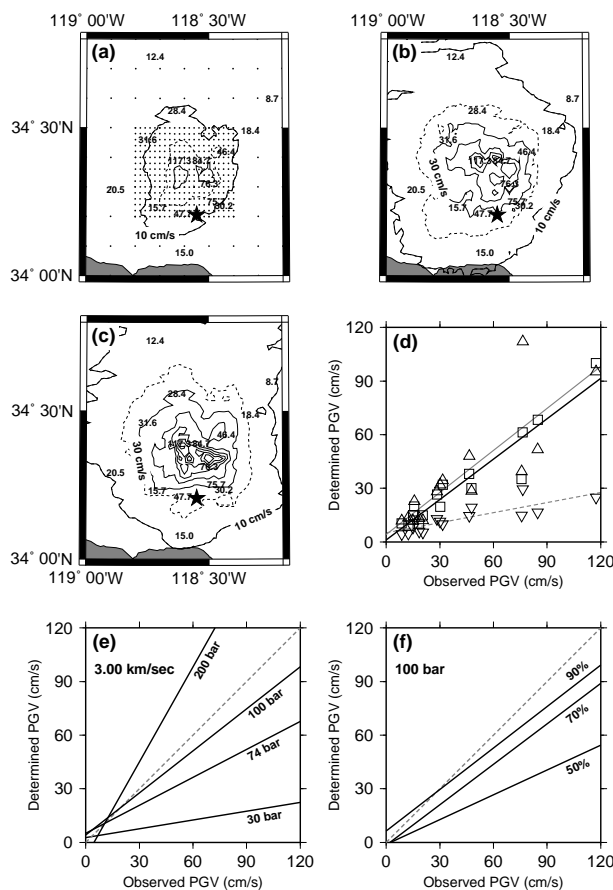


Figure 13.41: (a) PGV ShakeMaps simulated for the Northridge earthquake for model UNI. Black contours of PGV represent the geometric mean of two horizontal PGV components. The minimum level of contour is 10 cm/s and the interval is 20 cm/s. The dotted line is the 20 cm/s contour, indicating the extent of significant structural damage. The black star indicates main-shock epicenter. The black dots are the grid locations where strong motions are derived for ShakeMap. Black bold numbers on the map indicate 15 observed PGV. (b) Same as (a) for model REF. (c) Same as (a) for model VAR. (d) The simulated PGV values at 15 stations as a function of real observations for models VAR (triangles), REF (squares), and UNI (inverted triangles) and the best fitting lines for models VAR (thin grey), REF (thick black), and UNI (dotted grey). (e) The best fitting lines assuming different stress drops for constant rupture velocity of 3.00 km/s. For the reference, the perfect agreement line is indicated with the dotted gray line. (f) The best fitting lines assuming different rupture velocities for constant stress drop of 100 bars.

21. Joint Inversion for 3D Velocity Structure of the Middle East and North Africa to Improve Nuclear Explosion Monitoring

Suzan van der Lee (Northwestern University), Arthur Rodgers (LLNL), Megan Flanagan (LLNL), Michael Pasyanos (LLNL), Federica Marone and Barbara Romanowicz

21.1 Introduction

The need to monitor broader areas and an increasing number of nations with nascent nuclear weapons programs has lead to major challenges to nuclear explosion monitoring research. Agencies must, in fact, be prepared to detect, identify and locate nuclear explosions in wide regions, often aseismic and lacking previous seismic observations from specific test sites. Since the 1980's, the importance of monitoring at regional distances has been well established. However, such monitoring is complicated by the passage of seismic waves through the structurally complex crust and uppermost mantle. As a consequence, traveltimes and amplitudes of regional phases show great variability leading to large uncertainties in event locations and decreased performance of regional discriminants. A major requirement for the accurate modeling of regional seismic data and therefore improved event locations and regional discriminant performance are 3D regional velocity models characterized by high resolution from the crust down to the transition zone.

Our aim is a 3D velocity model of the crust and upper mantle for the geographic region extending from the western Mediterranean to Pakistan, including the aseismic region of North Africa. The joint inversion of different types of seismic data with diverse sensitivity to the crust and mantle is essential to achieve a high resolution image of the structure in this tectonically complex area, where six major tectonic plates and several microplates interact with each other. We expect predictions for seismogram characteristics (phase arrival times, amplitudes, dispersion) based on this new model to match most observations and be useful for event discrimination. Simultaneously, the new model will refine our understanding of the structure and tectonics in the study region.

21.2 Technical approach and dataset

Our 3D S -velocity model will be derived from the joint inversion of regional waveform fits, surface wave group velocity measurements, teleseismic arrival times of S and P waves, receiver functions and published results from active source experiments. The strength of jointly using various datasets lies in their redundancy (increase in the results accuracy) and complementarity (resolving power increase and trade-offs reduction).

The fitting of regional fundamental and higher mode Rayleigh waveforms is being accomplished using the Partitioned Waveform Inversion method (Nolet, 1990). Ex-

amples of recently obtained waveform fits are shown in Figure 13.42. The modeling of both fundamental and higher mode surface waveforms ensures resolution of the entire upper mantle structure down to the transition zone. The inclusion in the inversion of teleseismic arrival times will further boost the resolving power at mid and deep upper mantle levels, while group velocity measurements and constraints on crustal thickness from active-source literature and receiver function analysis will ensure high resolution in the shallow upper mantle.

The seismograms used in this work have been recently recorded by a variety of different stations and networks, both permanent and temporary, operating in the study region: MIDSEA deployment, Kuwait National Seismic Network (KNSN), the United Arab Emirates (UAE) Broadband deployment, the Jordan deployment, the Eastern Turkey Seismic Experiment (ETSE), the Caspian Broadband deployment, the Global Seismic Network (GSN), the International Monitoring System (IMS), MedNet and Geofon. While each of these waveform datasets is valuable on its own, their combination is unique and key to this study.

21.3 Preliminary results

The broad consistency between seismic velocity anomalies inferred from existing and performed measurements of teleseismic arrival times and Rayleigh wave group velocities as well as from regional waveform fits implies that these different types of dataset are at least in part redundant. The consistency further shows that the datasets record the same structural phenomena, despite differences in size and character between typical sensitivity kernels for each dataset.

Preliminary results from data analysis for the Middle East show that the uppermost mantle in this part of the study area is slower on average than typical 1D global velocity models as also previously observed in neighboring regions (e.g. in the Mediterranean (Marone *et al.*, 2004) and beneath the Iranian Plateau (Maggi and Priestley, 2005)).

21.4 Future of the project

The derived 3D S -velocity model will be converted to a 3D P -velocity model, using both published data on elastic properties (and their partial derivatives with temperature and pressure) of mantle rocks and empirical information provided by measured arrival times of teleseismic

P and Pms waves. The corresponding P -wave model will provide an improved ability to locate seismic events.

The prediction and calibration of regional traveltimes and waveforms depend strongly on the methodology used to compute synthetic traveltimes and waveforms from a 3D velocity model. Our goal is to test the obtained S - and P -wave models' ability to predict regional P and S traveltimes, deflect wave paths and deform waveforms using different approximations (e.g. path average vs. exact numerical approaches). We will assess the effects of 3D heterogeneities first on the studied seismograms (traveltimes and waveforms) and subsequently on the 3D models derived from these data.

21.5 Acknowledgements

This work has been financially supported by the National Nuclear Security Administration, Office of Nonproliferation Research and Engineering and Office of Defense Nuclear Nonproliferation (DE-FC52-04NA25542).

21.6 References

Maggi, A. and K. Priestly, Surface waveform tomography of the Turkish-Iranian Plateau, *Geophys. J. Int.*, *160*, 1068-1080, 2005.

Marone, F., S. van der Lee and D. Giardini, 3-D upper mantle S -velocity model for the Eurasia-Africa plate boundary region, *Geophys. J. Int.*, *158*, 109-130, 2004.

Nolet, G., Partitioned waveform inversion and two-dimensional structure under the network of autonomously recording seismographs, *J. Geophys. Res.*, *95*, 8499-8512, 1997.

Pasyanos, M.E., W.R. Walter and S.E. Hazler, A surface wave dispersion study of the Middle East and North Africa for monitoring the Comprehensive Nuclear Test Ban Treaty, *Pure Appl. Geophys.*, *158*, 1445-1474, 2001.

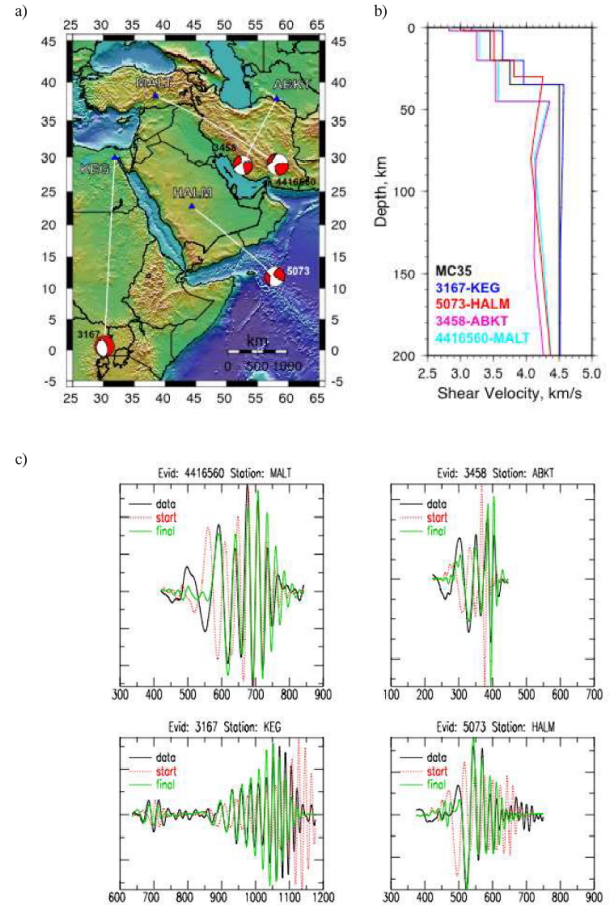


Figure 13.42: a) Map of the Middle East showing four earthquakes and paths for which waveform fits are shown. The events are indicated by their moment tensors. Stations are shown as blue triangles - b) 1D S -velocity models for the four paths shown in a). The used starting model, MC35, is shown in black - c) Fits for vertical component S - and Rayleigh waveforms for the four paths shown in a). In each panel, we show the observed waveform (black), the synthetic waveform computed using the starting (red dashed) and with the final model (green).

22. Constraints on Shear Wave Attenuation in the Earth’s Inner Core from an observation of PKJKP

Aimin Cao and Barbara Romanowicz

22.1 Introduction

Soon after *Lehmann* discovered the earth’s inner core in 1936 through the analysis of travel times of teleseismic body waves, *Birch* (1940) suggested that the inner core should be solid as a result of freezing of liquid iron in the outer core. Thirty years later, the first indirect evidence of the solidity of the inner core was documented by means of seismic normal mode eigenfrequency measurements (*Dziewonski and Gilbert*, 1971). However, the observation of the phase PKJKP, which traverses the inner core as a shear wave, is still a controversial issue, until now attempted by only few investigators. *Julian et al.* (1972) and *Okal and Cansi* (1998) each suggested the detection of PKJKP based on data from short-period seismic arrays in the ~ 1.0 Hz and 0.1-0.5 Hz frequency ranges, respectively. *Deuss et al.* (2000) argued that these two claims were misidentifications, and instead, proposed an observation of pPKJKP+SKJKP, based on stacking data from the global broadband network, in the frequency range 0.01-0.1 Hz. On the other hand, the existing Q_β estimates in the inner core are based solely on normal mode observations (*Dziewonski and Anderson*, 1981; *Widmer et al.*, 1991). There has been no attempt at estimating the shear wave attenuation in the inner core using body wave data.

PKIKP, which traverses the inner core as a compressional wave, is now a routinely observed phase. It should be observed simultaneously with PKJKP in the epicentral distance range 116° to 180° , according to the seismic reference model PREM. The relative amplitude of PKJKP varies strongly with frequency. Although we cannot rule out the possibility of observing PKJKP in the frequency range 0.1 to 0.5 Hz, it is more likely to be found at lower frequencies.

22.2 Data, Method, and Results

We use the high quality data from the broadband Gräfenberg Seismic Array (GRF) in Germany. With an aperture of $\sim 100\text{km} \times 50\text{km}$, GRF provides continuous high quality records at all of its 13 stations since 1980. Its geographical location with respect to frequent large events ($M_w > 7.0$), which occur in the south Pacific Ocean at distances around 140° , make it an ideal broadband seismic array to study PKJKP. We systematically examined large events from 1980 to 1999 and found ~ 20 large events in the vicinity of Tonga and Santa Cruz islands in this time interval. One of them ($M_w=7.3$, depth=76 km, 02/06/1999) is unique for PKJKP obser-

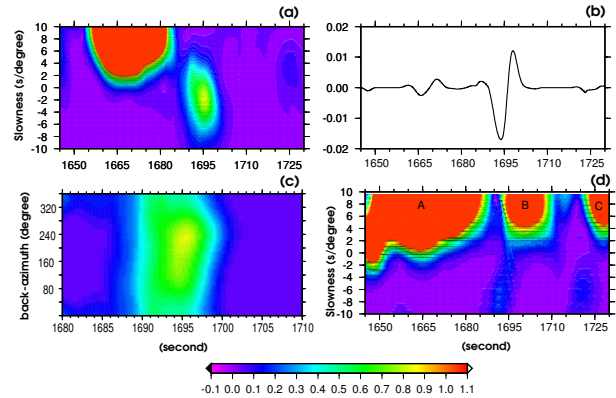


Figure 13.43: Evidence for the observation of PKJKP. (a) Observed vespagram for PKJKP in the slowness and travel time domain. (b) Stacked waveform corresponding to the energy maximum in (a). (c) Observed vespagram in the back-azimuth and travel time domain. The estimated back-azimuth is $\sim 223^\circ$ and the expected back-azimuth of PKJKP is 218° . (d) Synthetic vespagram for the pseudo-liquid inner core model.

vation. We choose the 0.06 to 0.1 Hz band for our analysis.

After aligning the seismograms with respect to the origin time of the event and making an array-sided travel time correction band-pass filtering, normalizing with respect to the first arrival (PKIKP+PKiKP), and stacking using the Phase Weighted Stack (PWS) technique (*Schimmel and Paulssen*, 1997), we computed a vespagram (Figure 13.43a), which corresponds to the predicted window for PKJKP based on the PREM mode. In the negative slowness range, the slowness of the energy maximum is $\sim -1.6\text{s/deg}$, close to the PREM prediction of -1.43s/deg . The arrival time is also compatible with PREM (1695 sec for the maximum energy, compared to a prediction of 1690 sec for the high frequency onset of the pulse). We also observe a clean stacked waveform corresponding to the energy maximum in the PKJKP window (Figure 13.43b). We verified that this phase arrives within 5° of the great circle path from the source, ruling out a scattered near source phase (Figure 13.43c). We further verified that this phase is not a mantle, outer core, or even crust phase (Figure 13.43d). In the negative slowness region there is no energy maximum corresponding to the observation in Figure 13.43a. For this, the in-

roduction of the concept of liquid inner core, as was done by *Duess et al.* (2000), is helpful. If the inner core were liquid, there would not be a PKJKP phase. Therefore, we constructed a synthetic vespagram for an assumed liquid inner core in the relevant time window, using the Direct Solution Method (DSM) to generate complete synthetic seismograms (*Takeuchi et al.* 1996).

The clear PKJKP waveform (Figure 13.43b) allows us to estimate the shear wave attenuation in the inner core. We use the envelope function of PKJKP in the synthetic differential seismogram between the solid inner core and the 'pseudo-liquid' inner core, to constrain the Q_β in the inner core. We process the synthetic differential seismograms in the same way as the observed seismogram and compare the envelope amplitude to the observed one for different values of Q_β in the inner core (Figure 13.44), obtaining a value of $Q_\beta \sim 320$, with an error of ± 150 , accounting for various uncertainties in the measurement. This is significantly higher than obtained from normal mode measurements. Normal modes mainly sample the shallow portion of the inner core, whereas PKJKP samples the central part. Thus, we find that Q_β increases with depth in the inner core, just as Q_α does (*Souriau and Roudil*, 1995). The envelope function modeling also suggests that the observed PKJKP is about 9.0 seconds faster than the synthetic PKJKP. It means that the constrained shear wave velocity in the inner core is $\sim 1.5\%$ faster than that for the PREM model, also in agreement with previous results if one allows for a slight increase in shear velocity with depth in the inner core.

22.3 Acknowledgments

We are grateful to the Gräfenberg Array operators for the long-term high quality maintenance of their array. This work was partially funded by NSF grant EAR-0308750.

22.4 References

Birch, F., The alpha-gamma transformation of iron at high compressions and the problem of the Earth's magnetism, *Am. J. Sci.* 238, 192, 1940.

Deuss, A., Woodhouse, J.H., Paulssen, H., and Trampert, J., The observation of inner core shear waves, *Geophys. J. Int.* 142, 67-73, 2000.

Dziewonski, A.M., and Gilbert, F., Solidity of the inner core of the Earth inferred from normal mode observations, *Nature* 234, 465-466, 1971.

Dziewonski, A.M., and Anderson, D.L., Preliminary reference earth model, *Phys. Earth Planet. Inter.* 25, 297-356, 1981.

Julian, B.R., Davies, D., and Sheppard, R.M., PKJKP, *Nature* 235, 317-318, 1972.

Lehmann, I., *P'*, Bur. Centr. Seismol. Int. A., *Travaux Scientifiques* 14, 87-115, 1936.

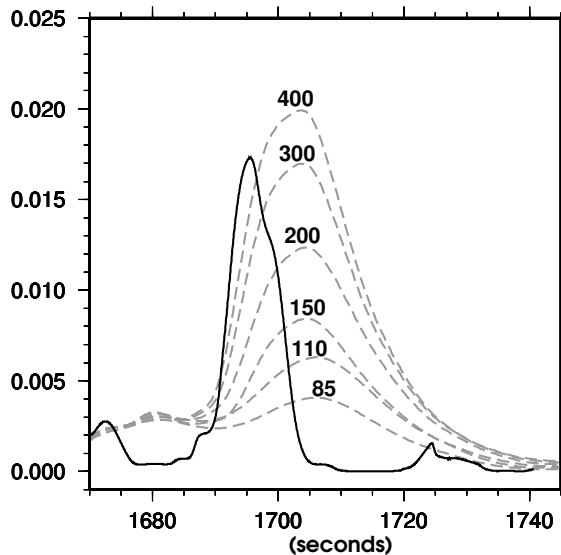


Figure 13.44: Envelope function modeling. The solid black line corresponds to the observed PKJKP, and dashed lines denote synthetic PKJKP with respect to different shear wave quality factors assumed in the inner core.

Okal, E.A., and Cansi, Y., Detection of PKJKP at intermediate periods by progressive multi-channel correlation, *Earth planet. Sci. Lett.* 164, 23-30, 1998.

Schimmel, M., and Paulssen, H., Noise reduction and the detection of weak, coherent signals through phase-weighted stacks, *Geophys. J. Int.* 130, 497-505, 1997.

Souriau, A., Roudil, P., Attenuation in the uppermost inner core from broad-band GEOSCOPE PKP data, *Geophys. J. Int.*, 123, 572-587, 1995.

Takeuchi, N., Geller, R.J., and Cummins, P.R., Highly accurate P-SV complete synthetic seismograms using modified DSM operators, *Geophys. Res. Lett.* 23, 1175-1178, 1996.

Widmer, R., Master, G., and Gilbert, F., Spherically symmetric attenuation within the earth from normal mode data, *Geophys. J. Int.* 104, 541-553, 1991.

23. High Resolution Anisotropic Structure of the North American Upper Mantle from Inversion of Body and Surface Waveform Data

Federica Marone and Barbara Romanowicz

23.1 Introduction

Seismic anisotropy is required for a correct interpretation of the retrieved S -velocity structure in tomographic studies at least in the first 400 km of the upper mantle (Gung *et al.*, 2003). A detailed knowledge of the seismic anisotropic structure of the earth's mantle also provides insight into debated geophysical issues, such as the nature and strength of the lithosphere/asthenosphere coupling, the depth extent of continental sub-regions and the relation of imaged seismic anisotropy to present-day asthenospheric flow and/or past tectonic events recorded in the lithosphere.

To date, our knowledge of the North American anisotropic structure arises mainly from global tomographic models (e.g. Ritsema *et al.*, 1999; Gung *et al.*, 2003) or SKS splitting studies (e.g. Fouch *et al.*, 2000; Savage and Sheehan, 2000), which lack horizontal and vertical resolution respectively, and are limited to either radial or azimuthal anisotropy.

Our goal is a new high resolution model for the North American upper mantle incorporating both radial and azimuthal anisotropy. We aim at unprecedented lateral and depth resolution by improving both data coverage and methodology.

23.2 Dataset

In this study, we consider fundamental and overtone surface waveforms selected from 3 component long period seismograms. Surface wave data for paths relevant to the study region has been extracted from the existing compilation used for global tomography in Panning and Romanowicz (2005). This dataset has been further complemented with waveforms from events at teleseismic and far regional distances ($15^\circ < \Delta < 65^\circ$) recorded at broad band seismic stations in North America. The collected dataset includes data for 540 events from 1993 to 1999, with M_w between 6.0 and 7.0. The main criteria guiding the event selection has been the achievement of the best possible path (Figure 13.45) and azimuthal coverage for the North American continent.

From each deconvolved and filtered seismogram, individual fundamental and higher mode surface wave packets have been extracted using an automated selection algorithm (Panning and Romanowicz, 2005) and subsequently checked by hand, to ensure a high quality dataset.

Our final dataset consists of more than 18,000 fundamental and 20,000 higher mode high quality surface wave

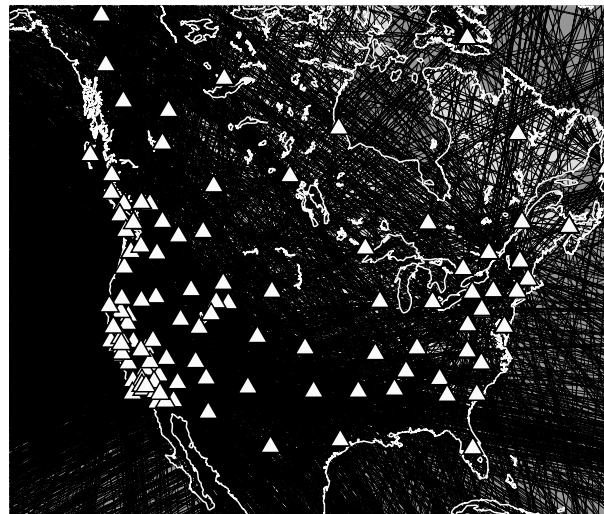


Figure 13.45: Data coverage - Paths of teleseismic events with $M_w \geq 6$ recorded at North American stations (indicated by white triangles), for which high quality fundamental mode Rayleigh wave packets have been selected.

packets. We expect that the achieved fairly homogeneous path and azimuthal coverage for North America will be further improved by taking advantage of the broad band dataset that is being collected under the USArray effort within EarthScope.

23.3 Methodology improvements

We invert seismic long period waveform data simultaneously for perturbations in the isotropic S -velocity structure and anisotropic parameter $\xi = \frac{v_S^2 H}{v_{SV}^2}$, in the framework of normal mode asymptotic coupling theory (NACT - Li and Romanowicz, 1996). The resulting broad band sensitivity kernels allow us to exploit the information contained in long period seismograms for body, fundamental and higher mode surface waves at the same time.

This approach was being applied at the global scale with lateral parametrization in terms of spherical harmonics (e.g. Li and Romanowicz, 1996). Here, we have adapted the procedure to the regional case by implementing a lateral parametrization in terms of spherical splines on an inhomogeneous triangular grid of knots (e.g. Wang and Dahlen, 1995), with the finest mesh for the region of interest, where the data coverage is densest, and a coarser

grid outside the study region. This flexible parametrization approach permits the perturbation of only a subset of the model parameters, for instance the ones falling within the target area, while using the entire set to correct the data for the global 3D heterogeneous structure, in this case using the radial anisotropic global model SAW24AN16 (Panning and Romanowicz, 2005).

Body and surface wave datasets used in mantle seismic tomography are sensitive to crustal structure, but cannot resolve details within the crust. Accurate crustal corrections are therefore essential for the quality of high resolution regional tomographic studies. The effect of shallow-layer features is often removed from the data by assuming an a priori crustal model (e.g. CRUST5.1) and applying linear perturbation corrections. However, lateral variations in Moho depth can be fairly large even over short distances, as for instance at ocean/continent transitions and the adequacy of linear corrections is questionable. In fact, Montagner and Jobert (1988) showed that the non-linearity of shallow-layer corrections is often non negligible even at long periods. In high resolution upper mantle regional tomographic studies, it is therefore important to take the crustal structure into account in a more accurate way. Going beyond the linear perturbation approximation, we follow the approach proposed by Montagner and Jobert (1988) and split the correction into a linear and non-linear part. At each point along a path, we assign a 1D reference model according to the local crustal structure (e.g. extended crust, orogen, ocean, ...). We then correct for the difference between the discontinuities in the chosen a priori crustal model (e.g. CRUST5.1) and the selected 1D local reference model assuming a linear perturbation, and exactly for the difference, if any, between the local reference model and PREM (our global reference model).

23.4 Results

Our 3D radial anisotropic model (Figure 13.46) shares the large scale features of previous regional tomographic studies for North America (e.g. Van der Lee and Nolet, 1997; Grand, 2001). We confirm the pronounced difference in the isotropic velocity structure between the western active tectonic region and the central/eastern stable shield, with the boundary being sharp and almost perfectly coincident with the Rocky Mountain Front. At transition zone depths, we document the presence of subducted material (Juan de Fuca and Farallon plate). Concerning the anisotropic signature, we observe a positive ξ anomaly in correspondence of the cratonic areas between 200 and 300 km depth.

Comparison of models obtained with different crustal correction approaches (linear vs. linear/non-linear perturbation approximation) shows that shallow-layer features can significantly bias the mantle structure down to 400 km depth and therefore confirms that accurate

crustal corrections are an essential step in high resolution regional tomographic studies. Both shape and amplitude of the imaged anomalies can be affected by inaccurate removal of the crustal signature.

23.5 Future of the project

Our final goal is a 3D high resolution tomographic model incorporating both radial and azimuthal anisotropy. Starting from our 3D radial anisotropic structure, we have begun addressing the distribution of azimuthal anisotropy, for which we have extended our NACT formalism. Resolving azimuthal anisotropy's four different components will only be possible with the improved coverage we expect from the USArray data. Meanwhile, using appropriate scaling relationships for the upper mantle, we are developing a preliminary 3D model, which, in addition to the isotropic S -velocity structure and the anisotropic parameter ξ , also incorporates the dominant $2\text{-}\Psi$ variations of anisotropy. Such a model can be interpreted in terms of an orthotropic medium, characterized by radial anisotropy with a symmetry axis of arbitrary orientation and described by the 5 Love parameters plus two angles defining the axis orientation. We hope to obtain constraints on the depth distribution of azimuthal anisotropy and in particular to discriminate between a lithospheric and an asthenospheric origin of the observed SKS splitting.

23.6 Acknowledgements

This work has been financially supported by the National Science Foundation as part of EarthScope (Grant EAR-0345481).

We are grateful to the IRIS Data Management Center (DMC) as well as to the Geological Survey of Canada for providing waveform data used in this study.

23.7 References

- Fouch, M.J., K.M. Fischer, E.M. Parmentier, M.E. Wysession and T.J. Clarke, Shear-wave splitting, continental keels, and patterns of mantle flow, *J. Geophys. Res.*, 105, 6255-6275, 2000.
- Grand, S.P., Mantle shear structure beneath the Americas and surrounding oceans, *J. Geophys. Res.*, 99, 591-621, 1994.
- Gung, Y., M. Panning and B. Romanowicz, Global anisotropy and the thickness of continents, *Nature*, 422, 707-711, 2003.
- Li, X.D. and B. Romanowicz, Global mantle shear-velocity model developed using nonlinear asymptotic coupling theory, *Geophys. J. R. Astr. Soc.*, 101, 22,245-22,272, 1996.
- Montagner, J.-P. and N. Jobert, Vectorial tomography; II. Application to the Indian Ocean, *Geophys. J.*, 94, 309-344, 1988.

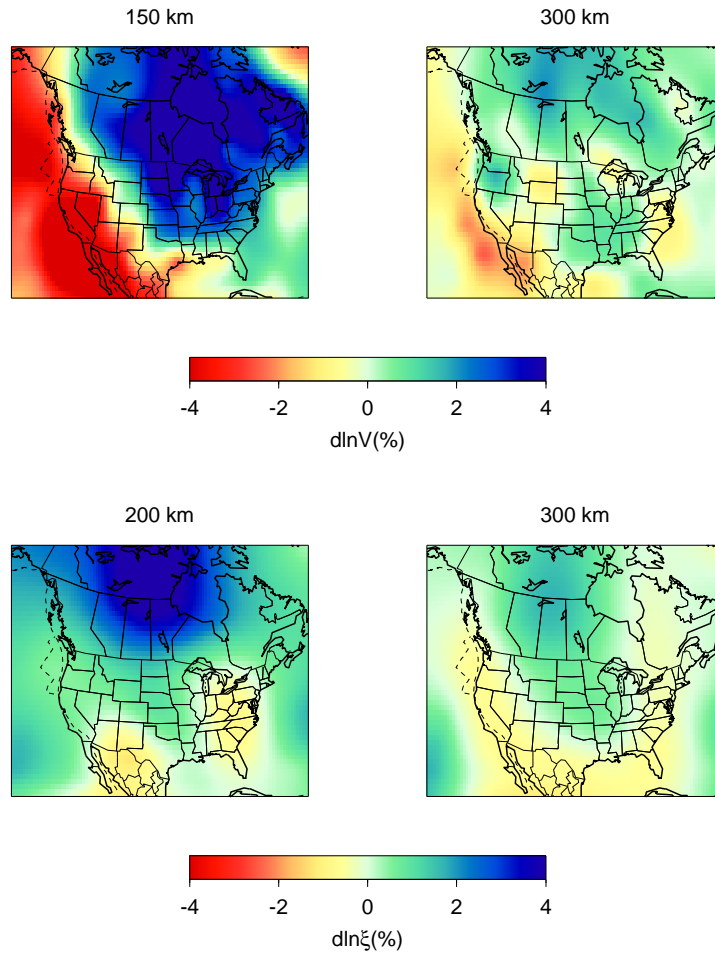


Figure 13.46: Horizontal slices at different depths through our 3D radially anisotropic model - Top: Perturbations in the isotropic S -velocity structure. Anomalies are relative to average - Bottom: Perturbations in the anisotropic parameter ξ . Anomalies are relative to isotropy.

Panning, M. and B. Romanowicz, A three dimensional radially anisotropic model of shear velocity in the whole mantle, *Geophys. J. Int.*, in revision, 2005.

Ritsema, J., H. van Heijst and J. Woodhouse, Complex shear wave velocity structure imaged beneath Africa and Iceland, *Science*, *286*, 1925-1928, 1999.

Savage, M.K. and A.F. Sheehan, Seismic anisotropy and mantle flow from the Great Basin to the Great Plains, western United States, *J. Geophys. Res.*, *105*, 13715-13734, 2000.

Van der Lee, S. and G. Nolet, Upper mantle S -velocity structure of North America, *J. Geophys. Res.*, *102*, 22815-22838, 1997.

Wang, Z. and F. Dahlen, Spherical-spline parametrization of three-dimensional Earth models, *Geophys. Res. Lett.*, *22*, 3099-3102, 1995.

24. Development of a Regional Velocity Model Using 3D Broadband Waveform Sensitivity

Mark Panning, Barbara Romanowicz, and Ahyi Kim

24.1 Introduction

We present a new approach to develop and evaluate earth models at the regional scale that utilizes full waveform seismograms. Adequate path calibrations are crucial for improving the accuracy of seismic event location and origin time, size, and mechanism. There is considerable information on structure in broadband seismograms that is currently not utilized. The limitations have been largely theoretical. The development and application to solid earth problems of powerful numerical techniques, such as the Spectral Element Method (SEM), has opened a new era, and it should be possible to compute the complete predicted wavefield accurately without any restrictions on the strength or spatial extent of heterogeneity. This approach requires considerable computational power, which is currently not fully reachable in practice.

We have begun work on an approach which relies on a cascade of increasingly accurate theoretical approximations for the computation of the seismic wavefield to develop a model of structure for the area of Eurasia located between longitudes of 30 and 150 degrees E, and latitudes of -10 to 60 degrees North. The selected area is particularly suitable for the purpose of this experiment, as it is highly heterogeneous, presenting a challenge for modeling, but it is well surrounded by earthquake sources and a significant number of high quality broadband digital stations exist, for which data are readily accessible through IRIS (Incorporated Research Institutions for Seismology) and the FDSN (Federation of Digital Seismic Networks).

24.2 Modeling Approach

The modeling approach utilizes increasingly advanced theoretical frameworks and numerical methods in order to obtain improved models of regional seismic structure. Specifically, a large-scale regional Eurasian model will be developed from a large dataset of seismic waveforms using the path-average approximation (PAVA) and NACT (Non-linear Asymptotic Coupling Theory; *Li and Romanowicz, 1995*), which are well-developed normal-mode based approaches which consider 1D (PAVA) and 2D (NACT) waveform sensitivity in the vertical plane along the great-circle path between source and receiver. This model will then be refined in a smaller region using an implementation of Born single-scattering theory (*Capdeville, 2005*), which more accurately represents the 3D sensitivity of the seismic wavefield. Finally, we will utilize the Spectral Element Method (SEM), a numerical approach that accurately models both 3D and non-linear

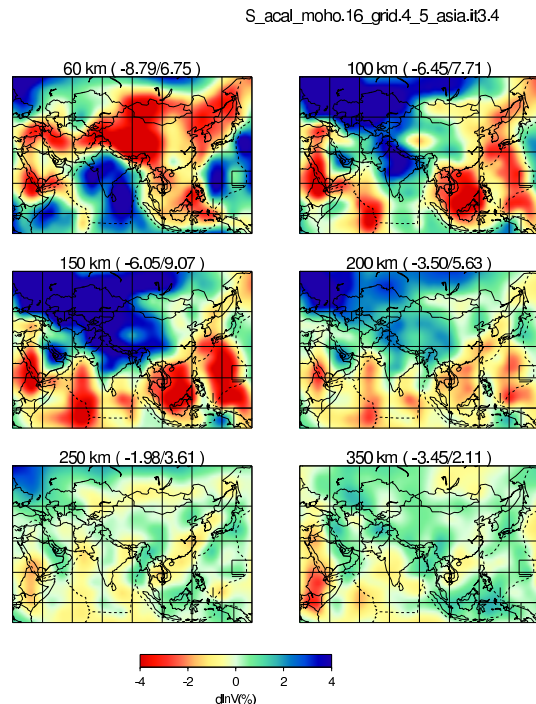


Figure 13.47: Preliminary smooth S velocity model for the upper mantle for the Eurasia developed using PAVA and NACT approaches. Values are the percent perturbations in isotropic velocity from PREM. Model is parameterized in radial splines spaced approximately 100 km, and in level 5 spherical splines (spacing ≈ 400 km).

effects (e.g. *Faccioli et al., 1996; Komatitsch and Vilotte, 1998*). To conserve computational resources we will restrict the use of SEM to the upper mantle by coupling to a normal mode solution (CSEM; *Capdeville et al., 2003*) and applying appropriate boundary conditions.

24.3 Preliminary Results

An initial model for Eurasia has been developed using PAVA and NACT and a global dataset of surface waveforms (Figure 13.47). This dataset includes waveforms both from our existing database (*Li and Romanowicz, 1996; Mégnin and Romanowicz, 2000; Gung et al., 2003; Panning and Romanowicz, 2004*), as well as new data, and includes 38826 3-component waveforms from 476 events recorded at 169 stations. While this model is smooth, it will serve as a starting point for the mod-

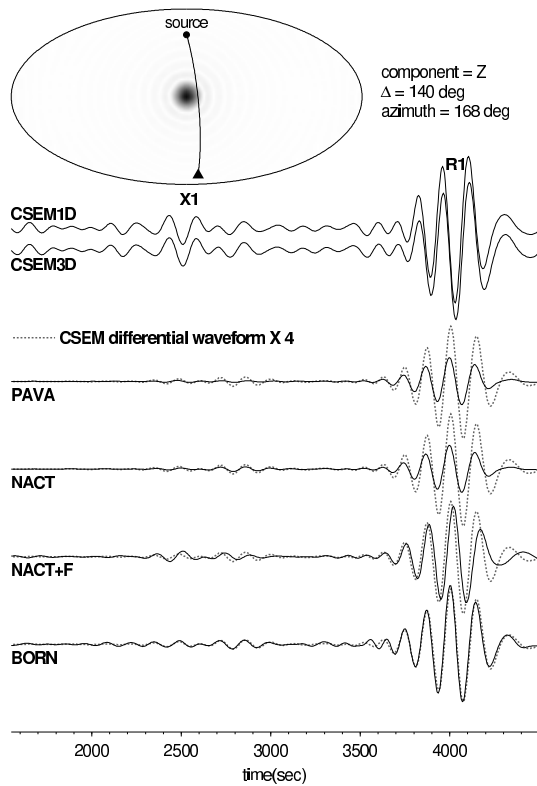


Figure 13.48: Comparison of performance of several mode-based approximations used in tomographic modeling. The map shows the source-receiver geometry and the velocity model, an ellipsoidal anomaly 5% slower than the background centered at 220 km depth. The top two traces are the SEM synthetics calculated from the 1D background model and the 3D model. The remaining traces show the differential waveforms obtained by subtracting the waveform produced by the 1D model. For each approximation, the differential SEM waveform is shown as a dotted line, and the waveform from the approximation is solid. Results are shown for the Path Average approximation (PAVA), Non-linear Asymptotic Coupling Theory (NACT), NACT plus a higher-order focusing approximation (NACT+F), as well as the 3D Born approximation.

els developed using increasingly accurate theoretical approaches.

The next step is to invert the surface wave dataset using the 3D implementation of Born scattering. Using this approach, we can calculate 3D sensitivity kernels with show significant sensitivity to off-path structure. We have performed verification tests that show that this approach can produce much more accurate seismograms for particular source-receiver paths (Figure 13.48).

Future work will include CSEM calculation of synthetics used in the inversion, which will include both 3D ef-

fects as well as the non-linear dependence of the waveforms to velocity structure.

24.4 Acknowledgements

We would like to acknowledge Yann Capdeville for the use of his Born code, and advice in the adaptation of this code to our project. This project has been funded through the Dept. of Energy, National Nuclear Security Administration, contract no. DE-FC52-04NA25543

24.5 References

- Capdeville, Y., E. Chaljub, J.P. Vilotte, and J. P. Montagner, Coupling the spectral element method with a modal solution for elastic wave propagation in global earth models, *Geophys. J. Int.*, *152*, 34-66, 2002.
- Capdeville, Y., B. Romanowicz, and Y. Gung, Global seismic waveform tomography based on the spectral element method, abstract, joint AGU/EGS/EUG Meeting, Nice, April 2003.
- Capdeville, Y., An efficient Born normal mode method to compute sensitivity kernels and synthetic seismograms in the Earth, submitted to *Geophys. J. Int.*, 2005.
- Faccioli, E., F. Maggio, A. Quarteroni, and A. Tagliani, Spectral-domain decomposition methods for the solution of acoustic and elastic wave equations, *Geophysics*, *61*, 1160-1174, 1996.
- Gung, Y., B. Romanowicz, and M. Panning, Anisotropy and lithospheric thickness, *Nature*, *422*, 707-711, 2003.
- Komatitsch, D. and J. P. Vilotte, The spectral element method: an effective tool to simulate the seismic response of 2D and 3D geological structures, *Bull. Seism. Soc. Am.*, *88*, 368-392, 1998
- Li, X.D. and B. Romanowicz, Comparison of global waveform inversions with and without considering cross-branch modal coupling, *Geophys. J. Int.*, *121*, 695-709, 1995.
- Li, X. D. and B. Romanowicz, Global mantle shear velocity model developed using nonlinear asymptotic coupling theory, *J. Geophys. Res.*, *101*, 22,245-22,273, 1996.
- Megnin, C. and B. Romanowicz. The 3D shear velocity structure of the mantle from the inversion of body, surface and higher mode waveforms, *Geophys. J. Int.*, *143*, 709-728, 2000.
- Panning, M. and B. Romanowicz, Inferences on flow at the base of Earth's mantle based on seismic anisotropy, *Science*, *303*, 351-353, 2004.

25. Toward the Constraints on Lateral S Wave Velocity Gradients and the Shape of the Pacific Superplume

Akiko To, Barbara Romanowicz

25.1 Introduction

We have recently documented that a sharp lateral boundary exists at the southern edge of the Pacific superplume (*To et al.*, 2005). The set of SHdiff wave forms, which graze the South Pacific superplume, have similar features to those observed previously at the southeastern edge of the African superplume. They both show a rapid shift of the arrival time with respect to azimuth and are followed by postcursors. First, we report the postcursors are explained as refractions from the lateral boundary on the D'' region. Second, we report that sharp lateral boundaries also exist not only in the southern edge of the super plume, but also in other regions surrounding the super plume.

25.2 Cause of the secondary arrival in Sdiff waveforms

The Sdiff waveforms which sample South Pacific superplume or the southeastern edge of the African superplume both show a rapid shift of the arrival time with respect to azimuth and they are followed by postcursors. In order to explain these features, we modified a tomographic SH model by increasing the gradient between the fast and slow anomalies, but keeping the shape of the boundary fixed (Figure 13.50 (Right)). We used the coupled mode/spectral element method (CSEM, *Capdeville et al.*, 2003), which can handle strong lateral variations of velocity in the D'', to construct synthetic waveforms. The synthetics from the original tomographic model (Figure 13.49 (Left)) do not generate the secondary arrival or the rapid shift of the first arrival. On the other hand, the synthetics from the modified model with the sharp boundaries (Figure 13.49 (Middle)) capture the features of the observed waveforms. The move out of the secondary arrival, which actually appears in multiple branches, shows a slope which is consistent with observations, although it appears at a slightly different azimuth. Moreover, the jump of the first arrival occurs around the azimuth of 215 degrees, which is also consistent with the observations. Particle motion analysis of observed and synthetic waveforms shows that the first pulse arrives from the southern side and the second pulse arrives from the northern side. Both the first and second arrivals are estimated to be refracted waves and their paths are described schematically in Figure 13.50 by yellow and green lines, respectively. The result suggests that it is important to take into account the heterogeneity outside of the great circle path.

25.3 Sharp lateral boundaries around the Pacific super plume

We have assembled a large dataset of Sdiff waveforms and travel time throughout the Pacific region. Also in other regions bordering the South Pacific superplume, observed Sdiff travel times vary rapidly over small ranges of azimuth and/or distance (Figure 13.51). The observed travel times can be better fit by increasing the amplitude and lateral gradients of the large scale velocity anomalies in a tomographic S velocity model. Modeling the pulses and the travel time jump due to lateral heterogeneity can help constrain the shape and velocity contrast at the superplume boundaries, at the base of the mantle.

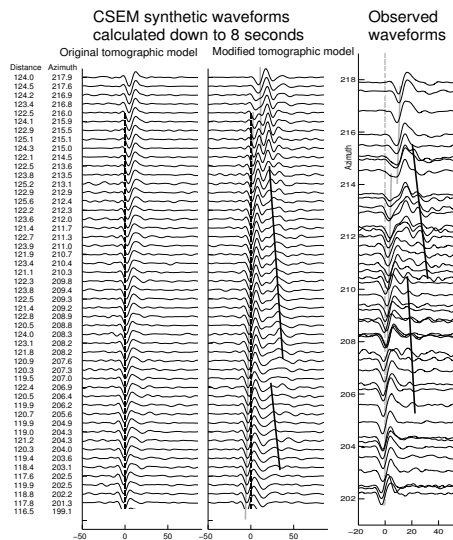


Figure 13.49: Synthetic waveforms calculated by CSEM down to 8 seconds. [Left] The waveforms from the original tomographic model (Figure 13.50 left panel); [Middle] the waveforms from the modified model (Figure 13.50 right panel). Gray lines follow the first trough, black lines follow the secondary arrivals. [Right] Observed velocity waveforms for event 19970904 in Fiji-Tonga (M_w 6.8) recorded in South Africa. Bandpass filtered with corner frequencies at 0.01 and 0.125 Hz. Y-axis shows the back azimuth. The broken line is the expected Sdiff arrival for the PREM model. Gray lines follow the trough of the first pulse. Black solid lines follow the secondary pulse, which is only observed in the vicinity of the structural boundary.

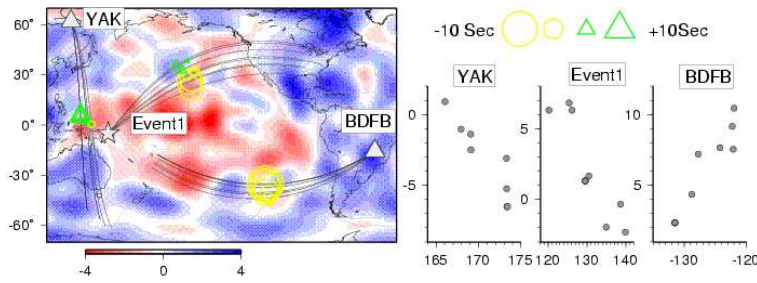


Figure 13.51: [Left] Sdiff ray path distributions where the rapid travel time shifts with respect to azimuth or back azimuth are observed. The background color map shows SAW24B16 model at CMB. Yellow circles and green triangles show the observed Sdiff travel time residuals with respect to PREM. Symbols are plotted at the middle point of the diffracting portion at CMB. White star and white triangles show the epicenter (Event1) and the stations (YAK and BDFB) which are discussed in the right figure. [Right] The Sdiff travel time residuals as a function of azimuth (for Event1) and back azimuth (for YAK and BDFB).

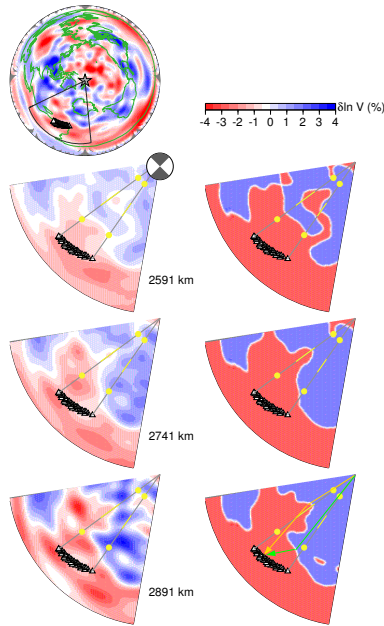


Figure 13.50: Left panel: the original SAW24B16 (Mégnin and Romanowicz, 2000) model at three depths in the bottom 300km of the mantle. The source in Fiji Tonga region is located at the apex. The stations in Africa are shown by triangles. Right panel: a model which is modified from SAW24B16. The boundary of the fast and slow anomalies is the contour line of 0% anomaly of SAW24B16. The anomaly jump is from -2.75 to 1.75%. Both models have 1D PREM structure from surface down to 370 km above the CMB. The 3D velocity anomalies linearly increase from 370 to 300 km above the CMB.

25.4 Acknowledgements

The data are downloaded from IRIS DMC and CNSN.

25.5 References

- Capdeville, Y., A. To and B. Romanowicz, Coupling spectral elements and modes in a spherical earth: an extension to the "sandwich" case, *Geophys. J. Int.*, 154, 44-57, 2003
- Mégnin C. and B. Romanowicz, The three-dimensional shear velocity structure of the mantle from the inversion of body, surface and higher-mode waveforms. *Geophys. J. Int.*, 143, pp. 709-728, 2000
- To, A., B. Romanowicz, Y. Capdeville and N. Takeuchi, 3D effects of sharp boundaries at the borders of the African and Pacific Superplumes: observation and modeling, *Earth and Planet. Sci. Lett.*, 233, 137-153, 2005

26. Towards Inverting Seismic Waveform Data for Temperature and Composition of the Earth’s Upper Mantle

Fabio Cammarano, Barbara Romanowicz, Lars Stixrude ^(a) and Carolina Lithgow-Bertelloni ^(a)
(a)Department of Geological Sciences, University of Michigan

26.1 Introduction

Unraveling the physical state of the upper mantle, including the transition zone (TZ), is one of the key factors for understanding the Earth’s mantle dynamics. Knowledge of mantle temperature and composition is mainly based on the interpretation of seismological observations based on insights from mineral physics. Despite the progress made to image the 3-D seismic structure of the upper mantle, its interpretation in terms of physical parameters is still challenging and it requires a truly interdisciplinary approach. Due to the better knowledge of the elastic and anelastic properties of mantle minerals at high temperatures and pressures, such an approach is now becoming feasible.

We propose a new waveform inversion procedure, based on a formalism previously developed at Berkeley for global elastic and anelastic tomography, and using our existing collection of long-period fundamental and higher mode surface waveforms. Here, we incorporate mineral physics data at an early stage of the process to directly map lateral variations in temperature and composition, using recent estimates of the temperature and composition derivatives of seismic velocities ($\partial \ln V / \partial \ln T, C$). We show preliminary tests of the inversion. We discuss ways to address the non-linearities, as well as uncertainties in the partial derivatives.

In addition to constraining the lateral variations in temperature or composition, the models can have implications on the average structure of the upper mantle. The most-common accepted physical 1-D structure had problems to satisfactorily fit seismic travel time data, requiring a slower TZ to improve the fit. However, these data do not have sufficient coverage (and resolution) in the TZ. A complementary outcome of our models will be to shed light on whether the seismic data require a modification of the physical structure in the transition zone and if the three-dimensional heterogeneity introduces a significant shift of the average physical structure away from adiabatic pyrolite.

26.2 Mineral physics data

The input parameters from mineral physics are the temperature and compositional partial derivatives of seismic velocities. These values are based on knowledge of elastic and anelastic properties of upper mantle minerals at appropriate pressure and temperature conditions. Compilation of recent data is being used to as-

sess the uncertainties of the temperature partial derivatives throughout the upper mantle (Cammarano *et al.*, 2003). A thermodynamic equation of state that determines jointly the phase equilibria and the elastic properties of the upper mantle has been recently proposed (Stixrude and Lithgow-Bertelloni, 2005). This provides a tool to compute consistently the compositional derivatives.

Anelasticity significantly increase temperature sensitivity in the mantle, but also enlarge notably the uncertainties of the partial derivatives. Moreover, anelasticity introduces a non-linear dependence of the seismic velocities with temperature throughout the upper mantle, and phase-transitions confer a non-linear character to the compositional derivatives as well. However, mineral physics experiments have shown that attenuation is not affected significantly by composition, while it is affected not only by temperature, but also by grain size (e.g. Faul and Jackson, 2005). Uncertainties in composition derivatives are then expected to be smaller, but their assessment will require further work.

26.3 Tests of inversion for temperature

The inversion is based on a normal mode asymptotic coupling mechanism (NACT, Li and Romanowicz, 1996). The seismic data used for the inversion are long period fundamental and overtone spheroidal modes selected on the vertical component of the seismograms included in the existing collection. Including higher modes provide resolution in the transition zone. No crustal correction has been used at this point. The direct inversion of the seismic waveforms for temperature requires $\partial \ln V / \partial \ln T$ (anelastic effects included) as a function of pressure (depth) and temperature and a starting thermal model as well. We choose an adiabat with a potential temperature of 1300° C overlaid by the geotherm for 60 m.y. old oceanic lithosphere.

To test the results of the inversion and assess the best way to address the non-linearities, we test our temperature inversion by performing in parallel an inversion for a physical reference model. The chosen model is one of the best-fit adiabatic pyrolitic models (PREF) for travel-time and fundamental mode data from Cammarano *et al.*, 2005. The models tested span the range of elastic properties for each mineral as inferred from mineral physics and applying different anelasticity models that cover the range of 1-D seismic attenuation models. Note that the thermal structure is exactly the same. An ex-

ample of how a temperature slice may be obtained by inverting with respect to a reference model is given in Figure 13.52

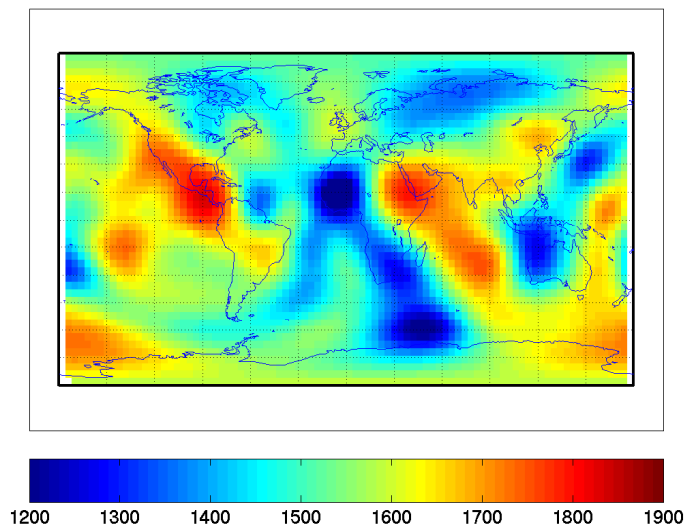


Figure 13.52: Example of horizontal tomographic slice for temperature at 300 km depth. Composition is pyrolitic. Note that the extremely low temperature beneath the African Craton is consistent with a contribution from compositional heterogeneity.

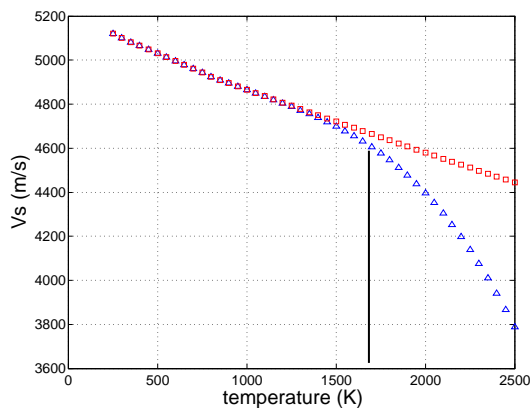


Figure 13.53: Examples of non linearity effects at 300km. Triangles represent variation of V_S with T by including anelasticity effects, squares are without it. Black line indicates the reference T at this depth.

The sensitivity kernels of the seismogram with respect to velocity are translated into temperature by using the partial derivatives. The kernels should be recomputed after each iteration of the inversion because of the non linearity introduced by attenuation. However, knowing how the effect changes as a function of temperature and depth, we will try to correct the model after each iteration. In figure 13.53, we show at a given depth (300

km) how the kernels change around the thermal reference temperature. Note that the kernels (the derivatives of Figure 13.53) change both towards high and low temperature.

26.4 References

Cammarano F., Goes S., Deuss A., Giardini D., Is a pyrolitic adiabatic mantle compatible with seismic data? *Earth and Planetary Science Letters*, 232, 227-243, 2005

Cammarano F., Goes S., Giardini D., Vacher P., Inferring upper mantle temperatures from seismic velocities. *Physics of the Earth and Planetary Interiors*, 138, 197-222, 2003

Li X.D., Romanowicz B., Global mantle shear velocity model developed using nonlinear asymptotic coupling theory. *Journal of Geophysical Res.*, 101, 22245-22272, 1996

Stixrude L., Lithgow-Bertelloni C., Thermodynamics of mantle minerals I, Physical properties. *Geophysical Journal International*, 162, 610-632, 2005

27. Europa Scenarios: Preliminary Physically Consistent Models of Europa

Fabio Cammarano, Vedran Lekic, Mark Panning, Michael Manga, Barbara Romanowicz

27.1 Introduction

Europa, one of the four major moons of Jupiter, presents planetary scientists with a set of fascinating questions, not the least of which concerns the presence of a water ocean beneath its icy surface. Recent magnetometer data acquired by the Galileo flybys seem to have confirmed the presence of Europa's ocean (Kivelson *et al.*, 2000). Additionally, detailed images of the planet allowed the observation of cracks in the ice consistent with flow of warm ice or water below the surface (Greeley *et al.*, 2000) and the near-infrared mapping spectrometer experiment probably detected hydrated salts on the surface (Mc Cord *et al.*, 2001). Nevertheless, any quantitative constraints on the ocean depth and the depth of the ice shell above it require further explorations.

Measurements of the seismic response of Europa remotely from an orbiter or using a lander can greatly expand our knowledge of its internal structure. Despite this potential, the feasibility of a seismic experiment that would exploit natural sound sources (e.g., the opening of the cracks in the ice) to investigate the thickness of the ice shell and the ocean depth, has only recently been considered. In order to determine the potential of seismic signals to discriminate between different possible scenarios for the structure of Europa, it is essential to provide a family of reasonable physical models.

We generate a set of physical models by assuming a three-layer composition: water-ice, silicate mantle (either pyrolytic or chondritic), metallic core (either solid iron or iron+sulfur) and different thermal structures. The thermal structures are based on estimations of the internal heating. Two extreme (cold and hot scenarios) have been considered. Thermodynamic properties as a function of pressure and temperature are computed for each layer by using equation of states based on the most recent mineral physics data (e.g. Wagner and Pruss 2002 for water, Stixrude and Lithgow-Bertelloni 2005 for the silicatic mantle). The depth of the ocean and of the core-mantle boundary are constrained by the mass and moment of inertia for each physical model.

Inversion for ocean depth and core-mantle boundary depth

For any possible combination of thermal structure and composition, we find the depth of the ocean and of the core-mantle boundary which best fits the mass and moment of inertia of Europa. For any physical structure, the uncertainties on those two depths are quite small and are

mainly due to the uncertainty of the gravitational constant (fig. 1).

We choose to not invert for the gravity acceleration (g) profile, which requires tedious iterations because of the feedback with the density profile. Instead, we approximate the gravity profile by pre-computing the values at the core-mantle boundary (assuming an average density of the core, based on the composition used), at the ocean bottom (assuming an average density of the water-ice layer combined with information about Europa's total mass) and by taking the known values at the surface (circa 1.31 m/s^2) and at the center (0) and by interpolating linearly between these points. The resulting gravity profile is sufficiently accurate, and does not noticeably affect our results.

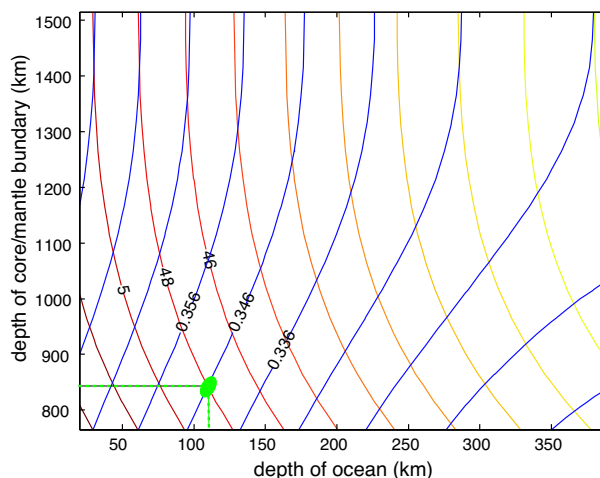


Figure 13.54: Example of determination of the ocean depths and core-mantle boundary for one physical structure. Yello-reddish contours are for mass value, blue for moment on inertia values. The green ellipse is the field of possible combination of the two depths to fit mass and moment of inertia

Anelasticity

Including anelasticity effects is essential to accurately characterize the seismic response of the different physical models. Anelasticity is strongly temperature dependent and it can be used to discriminate between the “cold” and the “hot” scenarios. In fact viscoelastic relaxation at high temperature leads to dispersion (frequency de-

pendence of seismic wave speeds) and dissipation (attenuation). The development of experimental techniques to measure the viscoelastic behavior at high temperature and seismic frequencies is beginning to provide direct constraints on the shear attenuation phenomena (e.g., *Faul and Jackson, 2005*). Extrapolation with pressure, which is still an important issue for the Earth, is less relevant for small planetary bodies where the pressure does not increase dramatically with depth. In this sense, we expect a (strong) constant attenuation throughout the “hot” adiabatic mantle. In the case of a cold mantle, we expect enhanced attenuation at the top of the mantle, and possibly at the core-mantle boundary. For the time being, we test the anelasticity effects using a model derived by *Cammarano et al., 2003*.

Conclusions

We calculate a range of thermodynamically consistent models for the physical structure of Europa, as constrained by the satellite’s mass and moment of inertia. We start with either a pyrolytic or a chondritic mantle composition and with either pure iron or iron plus 20% of sulfur core composition.

Due to the feedback between radiogenic and tidal heating, two extreme thermal profiles are possible in the mantle. Strong dispersion and dissipation is expected in the hot convective mantle, while anelasticity effects will be much weaker in the case of the cold mantle.

There is a strong relationship between different thermal structures and compositions. The “hot” mantle may well keep temperatures high enough to be consistent with a liquid core made of iron plus light elements. In the case of the “cold scenarios”, the possibility of a solid iron core cannot be excluded and it may even be favored.

The depth of the ocean and of the core-mantle boundary are determined with high precision once we assume the composition and thermal structure. In fact, the depth of the ocean is not very sensitive to the core composition used.

27.2 References

- Cammarano F., Goes S., Giardini D., Vacher P., Inferring upper mantle temperatures from seismic velocities. *Physics of the Earth and Planetary Interiors, 138*, 197-222, 2003
- Faul U.H., Jackson I., The seismological signature of temperature and grain size variations in the upper mantle. *Earth and Planetary Science Letters, 234*, 119-134, 2005
- Greeley R., Figueredo P.H., Williams D.A. et al., Geologic mapping of Europa. *J. Geophys. Res.-Planets, 105*, 22559-22578, 2000
- Kivelson MG, Khurana KK, Russell CT, et al., Galileo magnetometer measurements: A stronger case for a subsurface ocean at Europa. *Science, 289*, 1340-1343, 2000

Mc Cord T.B., Orlando T.M., Teeter G., Hansen G.B., Sieger M.T., Petrik N.G., van Keulen L., Thermal and radiation stability of the hydrated salt minerals epsomite, mirabilite, and natron under Europa environmental conditions. *J. Geophys. Res., 106*, 3311-3319, 2001

Stixrude L., Lithgow-Bertelloni C., Mineralogy and elasticity of the oceanic upper mantle: Origin of the low-velocity zone. *J. Geophys. Res., 110*, B03204, doi:10.1029/2004JB002965, 2005

Wagner W., Pruss A., The IAPWS formulation 1995 for the thermodynamic properties of ordinary water substance for general and scientific purpose. *Journal of Physical and Chemical Reference Data, 31*, 387-535, 2002